



NAVAL POSTGRADUATE SCHOOL

MONTEREY, CALIFORNIA

THESIS

**HYDRODYNAMIC RESPONSE OF A COMPOSITE
STRUCTURE IN AN ARCTIC ENVIRONMENT**

by

Scott H. Bolstad

June 2015

Thesis Advisor:
Second Reader:

Young W. Kwon
Jarema M. Didoszak

Approved for public release; distribution is unlimited

THIS PAGE INTENTIONALLY LEFT BLANK

REPORT DOCUMENTATION PAGE			<i>Form Approved OMB No. 0704-0188</i>	
Public reporting burden for this collection of information is estimated to average 1 hour per response, including the time for reviewing instruction, searching existing data sources, gathering and maintaining the data needed, and completing and reviewing the collection of information. Send comments regarding this burden estimate or any other aspect of this collection of information, including suggestions for reducing this burden, to Washington headquarters Services, Directorate for Information Operations and Reports, 1215 Jefferson Davis Highway, Suite 1204, Arlington, VA 22202-4302, and to the Office of Management and Budget, Paperwork Reduction Project (0704-0188) Washington DC 20503.				
1. AGENCY USE ONLY (Leave blank)		2. REPORT DATE June 2015	3. REPORT TYPE AND DATES COVERED Master's Thesis	
4. TITLE AND SUBTITLE HYDRODYNAMIC RESPONSE OF A COMPOSITE STRUCTURE IN AN ARCTIC ENVIRONMENT			5. FUNDING NUMBERS	
6. AUTHOR(S) Scott H. Bolstad			8. PERFORMING ORGANIZATION REPORT NUMBER	
7. PERFORMING ORGANIZATION NAME(S) AND ADDRESS(ES) Naval Postgraduate School Monterey, CA 93943-5000			10. SPONSORING/MONITORING AGENCY REPORT NUMBER	
9. SPONSORING /MONITORING AGENCY NAME(S) AND ADDRESS(ES) N/A			10. SPONSORING/MONITORING AGENCY REPORT NUMBER	
11. SUPPLEMENTARY NOTES The views expressed in this thesis are those of the author and do not reflect the official policy or position of the Department of Defense or the U.S. Government. IRB Protocol number ____N/A____.				
12a. DISTRIBUTION / AVAILABILITY STATEMENT Approved for public release; distribution is unlimited			12b. DISTRIBUTION CODE A	
13. ABSTRACT (maximum 200 words) Climate change has resulted in an increase in naval activity in the Arctic Ocean. While extensive research has been done on the interaction between different forms of ice and conventional steel hulls, little work has been done to assess the potential for composite-hulled vessels to operate safely in Arctic sea lanes. The goal of this experiment was to determine how well a composite hull can withstand ice loading and impacts with free-floating ice and whether a tumblehome, conventional, or a vertical hull performs best in the presence of ice. In order to do this, the tow tank at the Naval Postgraduate School was used. An ice equivalent was found which allowed for repeatable experimentation. Strain gauges were attached to critical locations of the composite plate towed through the tank. Both plate deformation and the resulting hydrodynamic force were measured for various ice conditions. A high-speed camera was used to qualitatively understand the flow characteristics of the ice around the composite plate. Finally, Ansys was used to determine if it was possible to replicate the experimental results. This work lays a basis for future tow tank experimentation involving ice interaction at the Naval Postgraduate School.				
14. SUBJECT TERMS Tow Tank, Fluid Structure Interaction, FSI, Composite Material, E-Glass, ANSYS, Hull Shape, CFX, Arctic.			15. NUMBER OF PAGES 131	
			16. PRICE CODE	
17. SECURITY CLASSIFICATION OF REPORT Unclassified	18. SECURITY CLASSIFICATION OF THIS PAGE Unclassified	19. SECURITY CLASSIFICATION OF ABSTRACT Unclassified	20. LIMITATION OF ABSTRACT UU	

THIS PAGE INTENTIONALLY LEFT BLANK

Approved for public release; distribution is unlimited

**HYDRODYNAMIC RESPONSE OF A COMPOSITE STRUCTURE IN AN
ARCTIC ENVIRONMENT**

Scott H. Bolstad
Ensign, United States Navy
B.S., United States Naval Academy, 2014

Submitted in partial fulfillment of the
requirements for the degree of

MASTER OF SCIENCE IN MECHANICAL ENGINEERING

from the

**NAVAL POSTGRADUATE SCHOOL
June 2015**

Author: Scott H. Bolstad

Approved by: Young W. Kwon
Thesis Advisor

Jarema M. Didoszak
Second Reader

Garth V. Hobson
Chair, Department of Mechanical and Aerospace Engineering

THIS PAGE INTENTIONALLY LEFT BLANK

ABSTRACT

Climate change has resulted in an increase in naval activity in the Arctic Ocean. While extensive research has been done on the interaction between different forms of ice and conventional steel hulls, little work has been done to assess the potential for composite-hulled vessels to operate safely in Arctic sea lanes. The goal of this experiment was to determine how well a composite hull can withstand ice loading and impacts with free-floating ice and whether a tumblehome, conventional, or a vertical hull performs best in the presence of ice. In order to do this, the tow tank at the Naval Postgraduate School was used. An ice equivalent was found which allowed for repeatable experimentation. Strain gauges were attached to critical locations of the composite plate towed through the tank. Both plate deformation and the resulting hydrodynamic force were measured for various ice conditions. A high-speed camera was used to qualitatively understand the flow characteristics of the ice around the composite plate. Finally, Ansys was used to determine if it was possible to replicate the experimental results. This work lays a basis for future tow tank experimentation involving ice interaction at the Naval Postgraduate School.

THIS PAGE INTENTIONALLY LEFT BLANK

TABLE OF CONTENTS

I.	INTRODUCTION.....	1
A.	ARCTIC OPERATING ENVIRONMENT.....	1
B.	COMPOSITE STRUCTURES	4
C.	PRIOR RESEARCH	7
D.	OBJECTIVES	8
II.	EXPERIMENT	11
A.	TOW TANK	11
B.	ICE EQUIVALENT.....	16
1.	Research.....	17
2.	Fabrication.....	20
C.	SIMULATION OF OPERATIONAL ENVIRONMENT	25
1.	Small-Scale Ice Interaction	25
2.	Large-Scale Ice Interaction.....	27
D.	COMPOSITE PLATE FABRICATION	29
E.	APPLICATION OF STRAIN GAUGES.....	32
1.	Determining Strain Gauge Location	32
2.	Strain Gauge Application.....	34
F.	TEST PLAN	37
G.	PROCEDURE	40
III.	RESULTS	47
A.	EXPERIMENTAL DATA REDUCTION	47
B.	BASE WATER TRIALS	49
C.	SMALL ICE DENSITY TRIALS.....	55
1.	Peak Force Analysis.....	57
2.	Peak Strain Analysis	63
3.	Ice Capacity Effect.....	66
D.	LARGE ICE TRIALS	68
E.	FRAMED COMPOSITE PLATE	73
F.	SUMMARY OF EXPERIMENTAL RESULTS.....	75
1.	Recommendations for Future Work	78
IV.	CFX MODEL	81
A.	CONTROL VOLUME	81
1.	Fluid Parameters and Boundary Conditions	83
2.	Solver Control and Mesh Adaptation	86
B.	CFX RESULTS AND DISCUSSION	86
C.	SUMMARY OF CFX ANALYSIS	92
1.	Recommendations for Future Work	93
APPENDIX A.	TOW TANK SOP.....	95
A.	FILLING AND DRAINING	95
B.	CARRIAGE OPERATION	96

APPENDIX B. STRAIN GAUGE CONNECTION: QUARTER-INCH BRIDGE ADAPTER	101
APPENDIX C. SUPPLEMENTAL CFX IMAGES.....	103
LIST OF REFERENCES	107
INITIAL DISTRIBUTION LIST	111

LIST OF FIGURES

Figure 1.	South China Sea Geography Resulting in Territorial Disputes, from [2].	2
Figure 2.	Arctic Region Geography Showing Potential for Disputes over Natural Resources, from [4].	3
Figure 3.	Vessels like the Fully Composite Constructed M80 Stiletto have Potential to Operate in the Arctic Region, from [7].	4
Figure 4.	Tumblehome Hull Exhibited by the DDG-1000 Zumwalt Destroyer, from [8].	5
Figure 5.	Conventional Hull Exhibited by the DDG-51 Arleigh Burke Destroyer, from [9].	6
Figure 6.	Vertical Hull Exhibited by a Medium Sized Norwegian Cargo Vessel, from [10].	6
Figure 7.	Halligan Hall Tow Tank with Dimensions.	11
Figure 8.	Tow Carriage Controller.	12
Figure 9.	Angle Selector for Precise Plate Orientation.	12
Figure 10.	WSN (A), Quarter-Inch Bridge Adapters (B), and External Battery Pack (C) Used to Transmit Strain and Force Values for Data Storage.	14
Figure 11.	Labview Computer Program Used for Data Acquisition.	14
Figure 12.	Data Obtained from Experimental Trials Divided into Acceleration Stage (A), Steady State Stage (B), and Deceleration Stage (C).	15
Figure 13.	Vessel Transiting through Brash Ice, from [17].	17
Figure 14.	Expected Surface Layer Practical Salinity Unit (PSU) in the Arctic Region Published by NOAA, after [21].	19
Figure 15.	Expected Surface Layer Temperature (°C) in the Arctic Region Published by NOAA, after [21].	19
Figure 16.	LDPE Rods Used to Simulate Arctic Ice.	21
Figure 17.	Electric Balance Used in Density Measurements.	21
Figure 18.	Graduated Cylinder and Scale Used for Water Density Measurements.	23
Figure 19.	Floating Characteristics of Rods with Lengths 25.4 cm, 38.1 mm, 50.8 mm, and 63.5 mm (1.0 in, 1.5 in, 2.0 in, 2.5 in).	24
Figure 20.	Small Diameter LDPE Rod Cutting Setup to Maximize Efficiency.	25
Figure 21.	Small-Scale Ice Present in Arctic Waters, from [23].	26
Figure 22.	Experimental Schematic to Simulate Conditions in Figure 21.	27
Figure 23.	Scattered Large-Scale Ice Present in Arctic Waters, from [24].	28
Figure 24.	Experimental Schematic to Simulate Conditions in Figure 23.	29
Figure 25.	Cutting Wheel Used to Cut Woven E-Glass Sheet.	30
Figure 26.	Resin and Hardener Mixed by Weight Ratio in Mixing Container.	31
Figure 27.	Workbench Used for Composite Plate Layup.	31
Figure 28.	Ansys Boundary Condition Relationship to Composite Plate.	33
Figure 29.	Hydrodynamic Pressure Resulting from Towing Plate.	33
Figure 30.	Location of Strain Gauges Noted by Red X's on Stress Profile.	34
Figure 31.	Taped Back Strain Gauges Prior to Application of Bonding Agent.	35

Figure 32.	Application of Weights to Ensure Proper Bonding between Strain Gauges and Composite Plate.	36
Figure 33.	Waterproofed Strain Gauges.	37
Figure 34.	Framed Composite Plate Used in Testing.	37
Figure 35.	Conventional Hull (Left) and Tumblehome Hull (Right) with $\theta=30^\circ$	40
Figure 36.	Beginning and End Locations Used for Measuring Average Speed. Only the Attachment Bar Bolts are Visible as Indicated by the Arrow.	41
Figure 37.	Correlation between Input Speed Setting (Hz) and both Velocity (m/s) and Motor RPM.	42
Figure 38.	Setup for 50% Capacity Small Ice Trials.	43
Figure 39.	Soldering Wire Attachments to Aid in Stabilizing Large Ice Equivalent.	44
Figure 40.	Large-Diameter Impact Test Setup.	45
Figure 41.	Go-Pro Used to Record Underwater Footage.	45
Figure 42.	Raw Experimental Force Data.	47
Figure 43.	Corrected Experimental Force Data Used in Analysis with Steady State Region Isolated.	48
Figure 44.	Corrected Experimental Strain Data Used in Analysis.	48
Figure 45.	Strain Gauge Location and Terminology.	49
Figure 46.	Average Force Required to Tow Different Plate Orientations for Base Water Trials.	50
Figure 47.	Flow Around Vertical Plate at 9 Hz Exhibiting Partial Freeboard.	51
Figure 48.	Flow Around Tumblehome Plate at 9 Hz Exhibiting Overflow.	51
Figure 49.	Flow Around Conventional Plate at 9 Hz Exhibiting Full Freeboard.	52
Figure 50.	Average Strain Experienced by Vertical Strain Gauges during Base Water Trials.	53
Figure 51.	Average Strain Experienced by the Horizontal Strain Gauge for Base Water Trials.	54
Figure 52.	Competing Deformation Modes at High Velocities.	55
Figure 53.	Use of Carriage Velocity and Distance to Ice Equivalent Section to Verify Impact Time.	56
Figure 54.	Isolated Impact Strain Data.	57
Figure 55.	Peak Force Percent Increase for High Capacity Ice Trials.	58
Figure 56.	Profile View of the Small Ice Section as the Three Plate Orientations Approach the Ice Equivalent.	59
Figure 57.	Profile View of the Small Ice Section as the Three Plate Orientations Contact the Ice Equivalent.	60
Figure 58.	Profile View of the Small Ice Section as the Three Plate Orientations near the End of the Ice Section.	61
Figure 59.	Enlarged Image of the Flow Profile for Tumblehome Plate in the Middle of the Ice Section at 9 Hz.	62
Figure 60.	Enlarged Image of the Flow Profile for the Tumblehome Plate at the End of the Ice Section at 7 Hz.	62
Figure 61.	Percent Change in Strain for the Vertical Orientation during High-Capacity Small Ice Trials.	64

Figure 62.	Percent Change in Strain for the Tumblehome Orientation during High-Capacity Small Ice Trials.....	65
Figure 63.	Percent Change in Strain for the Conventional Orientation during High Capacity Small Ice Trials.....	66
Figure 64.	Percent Change in Strain for the Vertical Orientation at 7 Hz for Different Ice Capacities.....	67
Figure 65.	Percent Change in Strain for the Tumblehome Orientation at 7 Hz for Different Ice Capacities.	67
Figure 66.	Percent Change in Strain for the Conventional Orientation at 7 Hz for Different Ice Capacities.	68
Figure 67.	5 Hz Conventional Trial with no Apparent Impact Point.	69
Figure 68.	Strain and Force Resulting from Large Ice Double Impact at 7 Hz.	70
Figure 69.	Strain and Force Resulting from Large Ice Double Impact at 9 Hz.	70
Figure 70.	Profile View of each Plate Orientation on Approach to the Large Ice Equivalent.	72
Figure 71.	Profile View of each Plate Orientation on Contact with the Large Ice Equivalent.	72
Figure 72.	Profile View of Each Plate Orientation After Contact with the Large Ice Equivalent.	73
Figure 73.	Average Strain Experienced by the Framed Plate during Base Water Trials.	74
Figure 74.	Incident Pressure Resulting from the Plate Travelling through the Ice Equivalent.	75
Figure 75.	Incident Pressure against the Plate for the Case where the Water Line is Lowered.	76
Figure 76.	Ice Accumulation Present Preceding the Tumblehome-Oriented Plate.....	78
Figure 77.	Control Volume with Location of the Inlet, Outlet and Opening Displayed.	82
Figure 78.	Mesh Sizing Used for CFX Control Volume.....	83
Figure 79.	Water Level for Tumblehome (Top) and Conventional (Bottom) Flow Simulations.	87
Figure 80.	Exploded View of Water Level Preceding the Tumblehome (Left) and Conventional (Right) Oriented Plates.....	88
Figure 81.	Exploded View of the Wake Region behind the Tumblehome (Left) and Conventional (Right) Oriented Plates.....	88
Figure 82.	Water Velocity in the Control Volume. Inlet Velocities are 1.0 m/s.....	89
Figure 83.	Pressure Planes Signifying the High Pressure Region Preceding the Tumblehome (Left) and Conventional (Right) Oriented Plates.	90
Figure 84.	Pressure Rise Preceding Both Plate Orientations.	91
Figure 85.	Incident Pressure against the Tumblehome (Left) and Conventional (Right) Oriented Plate Acquired from Ansys Simulation.....	92
Figure 86.	Halligan Hall Tow Tank.	95
Figure 87.	Drain Valve Open (Left) and Closed (Right) Positions.....	95
Figure 88.	Tow Tank Fill Piping.....	96
Figure 89.	Carriage System.....	97

Figure 90.	Carriage System Power Switches.	97
Figure 91.	Carriage Controller.	98
Figure 92.	Strain Gauge Connection to the Quarter-Inch Bridges.	101
Figure 93.	The Towed Plate and the Attachment Bar are Removed from the Control Volume of the Tow Tank Using the Combine Feature in Solidworks. The Plane Created to Generate the Plate Orientation is also Visible.	103
Figure 94.	Mesh Used in CFX Trials.	103
Figure 95.	Variables Created for CFX Analysis, after [27].	104
Figure 96.	Fluid Domain Basic Settings, after [27].	105
Figure 97.	Mesh Adaptation Settings, after [27].	106

LIST OF TABLES

Table 1.	Density Measurements of Sea Ice, from [19].	18
Table 2.	Diameter Variations along LDPE Rods.	22
Table 3.	Density Calculation Summary.	22
Table 4.	Density Results for Tow Tank Water.	23
Table 5.	Test Plan.	38
Table 6.	Percent Change for Force and Strain Values at 1.18 m/s Due to Impact with Large Ice Equivalent.	71
Table 7.	Mesh Parameters of Control Volumes.	83
Table 8.	Fluid Domain Settings Establishing Two-Fluid System, after [27].	84
Table 9.	Inlet Boundary Conditions, after [27].	85
Table 10.	Outlet Boundary Conditions.	85
Table 11.	Opening Boundary Conditions, after [27].	85
Table 12.	Wall Boundaries.	86
Table 13.	Solver Controls, after [27].	86
Table 14.	Elimination of Hydrostatic Force from Peak Pressure Data.	91

THIS PAGE INTENTIONALLY LEFT BLANK

LIST OF ACRONYMS AND ABBREVIATIONS

cm	Centimeter
DOD	Department of Defense
ft	Feet
in	Inch(es)
kg	Kilogram
LDPE	Low Density Polyethylene
m	Meter
mm	Millimeter
NASA	National Aeronautics and Space Administration
NRL	Naval Research Laboratory
ONR	Office of Naval Research
PSU	Practical Salinity Unit
s	Second(s)
SOP	Standard Operating Procedure
UNCLOS	United Nations Convention on the Law of the Sea
U.S.	United States
WSN	Wireless Sensor Network
ϵ	Strain
μ	Micro (10^{-6})

THIS PAGE INTENTIONALLY LEFT BLANK

ACKNOWLEDGMENTS

I'd like to start out by thanking all of the professors at NPS. Every professor I have had in my one year here has been willing to take the time to answer my many questions. Specifically, I would like to thank my advisor, Professor Kwon, for helping me formulate a project that would be challenging, yet could still be fully completed in my short time here. I would like to thank Professor Didoszak for aiding in the camera work and for also helping in my thesis work. I would also like to thank the Rocket Lab for allowing me to borrow their Go-Pro. A special thanks to Dr. Park for his help in applying strain gauges.

I would also like to specifically thank two others who have been a great help in completing my thesis. First, Professor Hobson is responsible for teaching me everything I know involving Ansys and CFX. Throughout the completion of my thesis, I have made many visits to his office to tap his CFX expertise. Finally, a special thanks to the ME Machine shop tech John Mobley. He lent his practical know-how and aided me in smartly fabricating or machining all of the parts needed for the experiment. All of the jobs were professionally done and it was a pleasure to do some hands-on work with him.

THIS PAGE INTENTIONALLY LEFT BLANK

I. INTRODUCTION

A. ARCTIC OPERATING ENVIRONMENT

The emergence of sea lanes throughout the Arctic region is an on-going event that will have an effect on international politics for years to come. Not only is the region experiencing heavier maritime traffic due to more efficient shipping routes, but it also may become an area of interest for many nations in the surrounding area. Both the Beaufort and Chukchi seas are believed to hold the world's largest unrecovered reserves of oil and natural gas [1]. In 2012, the U.S. Coast Guard began operation Arctic Shield in which it assessed its capabilities of operating in the aforementioned seas as Shell prepares to tap into their natural resources [1]. The U.S. Navy also conducts ICEX exercises, which familiarize submarines with operational procedures for transiting the Arctic. These are but a few of the actions the U.S. has begun to prepare for Arctic operations. While the initial probing of the natural resource rich seas in the Arctic has been peaceful, future global demands of such natural resources could spur conflict.

Such a conflict may be similar to the current dispute of the Spratly Islands and the surrounding areas in the South China Sea. There have been numerous incidents involving vessels from China, Taiwan, the Philippines, and Vietnam as they each seek to lay claim over the natural resources in the region [2]. The problem lies in the United Nations Convention on the Law of the Sea, or UNCLOS. This signed document defines a 200 mile exclusive economic zone (EEZ) that extends from a countries shoreline. The proximity of the countries in the South China Sea, shown in Figure 1, skews each country's claim to the islands.



Figure 1. South China Sea Geography Resulting in Territorial Disputes, from [2].

In the 1970s and 1980s, incidents between Vietnam and China resulted in the death of over 130 Vietnamese sailors [2]. Over 40 years later, the dispute over natural resources continues as each country attempts to validate its claim over the islands.

While there have been no known clashes over territory in the Arctic, the same potential for disputes as found in the South China Sea is present. Canada, Denmark, and Russia all assert that the Lomonosov Ridge is an extension of their continental shelves [3]. The clustered Arctic region and various countries' territorial claims are displayed in Figure 2.

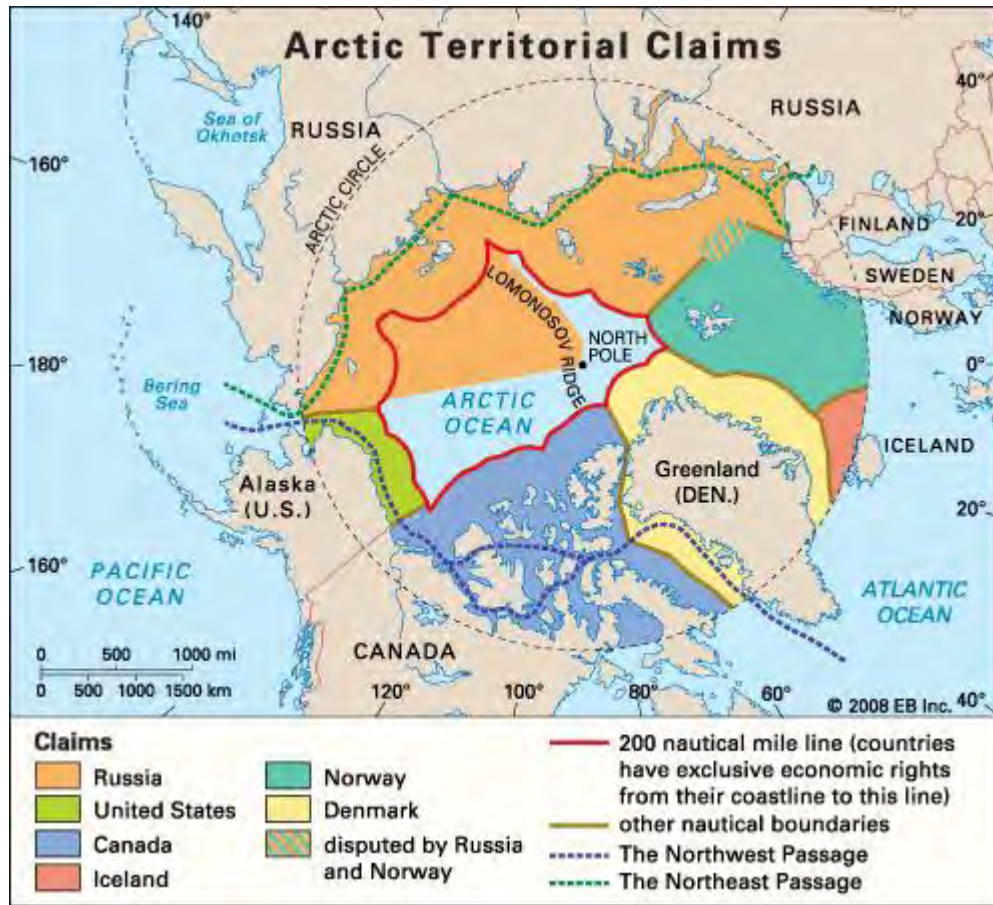


Figure 2. Arctic Region Geography Showing Potential for Disputes over Natural Resources, from [4].

For this reason, it is in the United States' best interests that it should be well versed in operating in the Arctic. The U.S. military has taken initial steps to prepare for Arctic operations. The DOD has published Arctic Strategy and the U.S. Navy Arctic Roadmap [3]. These documents promote the extension of infrastructure and additional research to support Arctic operations. ONR funds facilities such as NRL to conduct operations which better prepare the U.S. for Arctic operations. Countries such as Russia, Canada, and Norway have already begun honing their military prowess in the region [3]. This paper intends to add to the knowledge base by addressing the interaction between a fast-moving composite hulled ship and free-floating ice found in Arctic sea lanes.

B. COMPOSITE STRUCTURES

Considering extensive research has been conducted on the interaction between traditional steel hulls and ice [5], this paper focuses on the interaction between E-Glass and ice. Composite material is becoming more prevalent in construction of cutting edge naval vessels. In 2006, the U.S. navy commissioned an experimental vessel named *M80 Stiletto* [6]. This was the navy's first ship constructed entirely of composite materials. The 24-meter long ship is built from carbon fiber reinforced epoxy. The ship is displayed in Figure 3.



Figure 3. Vessels like the Fully Composite Constructed M80 Stiletto have Potential to Operate in the Arctic Region, from [7].

The ship is intended for littoral operations. The carbon fiber hull results in a lightweight craft with a draft of one meter at its top speed. It is capable of speeds of up to 60 knots [6]. As the craft travels faster, the hull is lifted farther out of the water, reducing the drag which inhibits forward motion. In conjunction with its shape, the composite hull

allows the M80 Stiletto to operate undetected to radar. These attributes make the M80 Stiletto ideal for any special operation mission.

Another topic of interest covered in this thesis is the performance of different hull types as they travel thorough the Arctic. More specifically, these hull types' ability to travel through ice will be assessed. A hull is characterized by its profile at the waterline. The three hull types under investigation are the flared conventional hull type found on the Arleigh Burke Destroyer, the swept tumblehome hull found on the DDG-1000 Zumwalt Destroyer, and the wall-sided (termed "vertical" for the experiment) hull found in some tankers and transport vessels. These hull types are displayed in Figure 4, Figure 5, and Figure 6, respectively.



Figure 4. Tumblehome Hull Exhibited by the DDG-1000 Zumwalt Destroyer, from [8].



Figure 5. Conventional Hull Exhibited by the DDG-51 Arleigh Burke Destroyer, from [9].



Figure 6. Vertical Hull Exhibited by a Medium Sized Norwegian Cargo Vessel, from [10].

Most nautical vessels exhibit the conventional hull of the Arleigh Burke Destroyer-shaped hull. These hulls are most notable for their overall consistent performance and their stability in rough seas; hence every warship in the U.S. Navy other than the DDG1000 has this hull type. The main purpose of the tumblehome design is to significantly reduce the radar cross section of this ship. Another benefit of a tumblehome hull is that the ship travels through the calm seas more efficiently, which helps reduce the cost of fuel. These advantages come at the detriment to the ship's ability to operate in rough seas. Most critics believe the DDG1000 cannot operate safely in hazardous conditions. In 1997, NPS student Brian Ellis concluded that a tumblehome hull has the potential to reduce the maximum righting arm of a ship by 40% when compared to conventional hulls [11]. The current experiment will assess the ability of each hull type to displace and effectively travel through free-floating ice.

C. PRIOR RESEARCH

This study focuses on the impact between floating ice and a composite hull. However, as mentioned before, only one commissioned U.S. Navy vessel utilizes a composite hull. Composite materials are typically only found in the superstructure of large sea-going vessels. The bulk of research involving the impact resistance of composite materials stems from the aviation industry. Pinnell and Sjoblom [12] state that the aviation industry is concerned with two different types of impacts; high-velocity impacts which result in penetration of the composite and low-velocity impacts resulting in visual damage to the composite structure. Their paper focuses on the results of low-velocity impacts which are similar to those experienced by a ship's hull as the hull strikes floating ice. Pinnell and Sjoblom found that low-velocity impacts can result in matrix cracking, delamination, and fiber fracture in two different locations. The two locations they described are the immediate layers at the location of the impact and in the plies just behind the back surface of the composite plate [12]. A NASA technical paper [13] supports these findings and notes that the most severe cracking and delamination occurs on the side opposite of the impact point where the flexural stresses are greatest. Both visual inspection and X-Ray imaging were used to locate surface and subsurface failures in the composite [13].

A common method of testing the impact resistance of composite materials is by completing a drop tower test. This involves the release of a mass from a known height above a composite plate. This test produces repeatable test results. Russell's [14] work shows the repeatability of subsequent trials using a drop tower. Russell's work shows that the same impact parameters results in a different response for a composite plate in air and a composite plate in water. The maximum strain occurs in a different location of a plate and at a higher magnitude in water. This is due to the fluid structure interaction (FSI). The density of water is nearly 784 times denser than air. This results in structures having different responses when perturbed in the different fluids [14]. Another work shows that the presence of water around the structure results in an increased stress response from the impact of nearly 50% [15]. These results will be taken into consideration for this tow tank experiment. Ideally, a composite hull would be fabricated in which only one side would be exposed to water. However, a simple composite plate was used with water present on both sides of the plate as an initial study.

D. OBJECTIVES

The goal of this thesis was to characterize the response of various hull types as they impact free-floating ice which is commonly found in Arctic sea lanes. In order to perform repeatable tow tank experiments, an ice equivalent was found. Upon proof of concept, this ice equivalent may be used in future tow tank experiments which hope to expand the knowledge base for Arctic operations. Video of the front edge of the composite plate was recorded to determine whether the ice equivalent strikes the plate or is displaced by the bow wave generated by the plate. It was possible that there was a critical velocity at which the ice is no longer displaced by the bow wave. Force and strain measurements were recorded to quantify how well each hull orientation progressed through ice infested waters. Two different plates were used in testing. The two plates were same size; however, the boundary conditions of the two were different. The first plate was created for research in a prior thesis. This plate has a frame surrounding the plate. This simulates Dirichlet boundary conditions around the plate. Another composite plate was fabricated and used to simulate Neumann boundary conditions.

A computer model of the tow tank experiment was also generated in hopes of replicating the experimental data. A two fluid domain consisting of air and water was created in CFX to assess the free surface effect at the water's surface and its interaction with the three different hull orientations. A base model was generated which could be improved to better simulate the interaction between free-floating objects and the composite plate.

THIS PAGE INTENTIONALLY LEFT BLANK

II. EXPERIMENT

A. TOW TANK

This experiment utilized the tow tank located in Halligan Hall on the Naval Postgraduate School campus. The tow tank and its dimensions are shown in Figure 7.

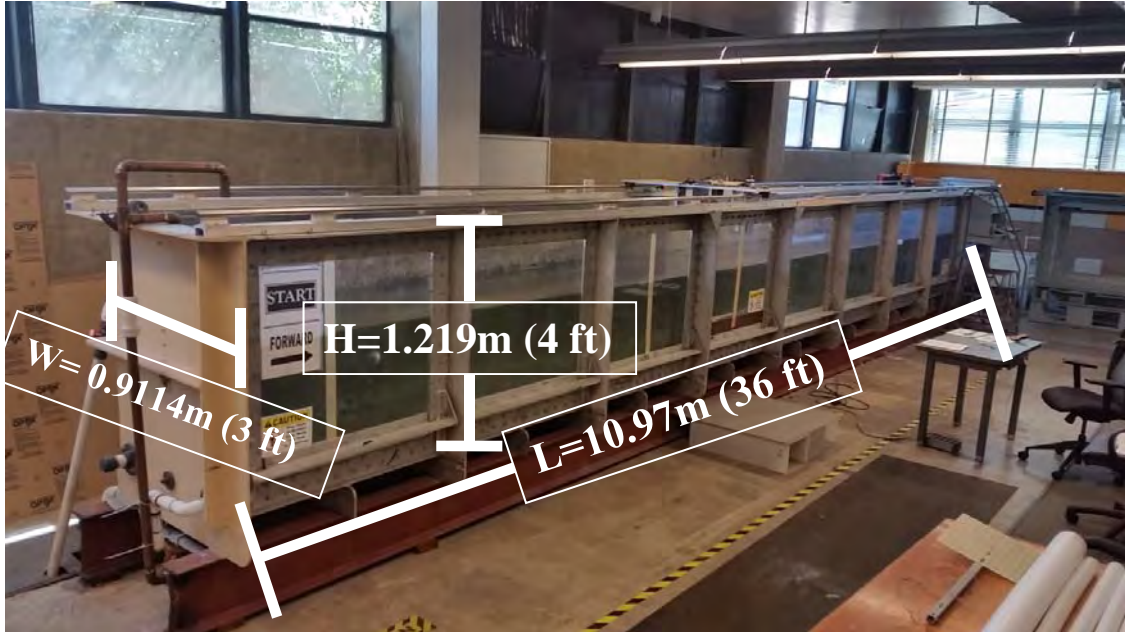


Figure 7. Halligan Hall Tow Tank with Dimensions.

In order to tow objects, a carriage is attached to the top rails with ball bearings. This allows the carriage to translate along the length of the tow tank. The carriage is pulled using a five horse-power motor connected to a pulley system which runs along the length of the tow tank. This motor is controlled with a Baldor controller connected to 30 meters of cable. This allows for the operator to control the carriage at any location around the tank. The operator inputs speeds settings in Hz. A minimum of 2.3 Hz is required to move the carriage. The full set of operating guidelines can be found in the tow tank SOP located in Appendix A. The relationship between the input frequency and the carriage velocity will be shown later. The controller is shown in Figure 8.



Figure 8. Tow Carriage Controller.

In order to tow the composite plate at a specified angle through the water, an angle selector is located on the underside of the carriage. This part was fabricated by the machine shop for previous theses. The angle selector is shown in Figure 9.



Figure 9. Angle Selector for Precise Plate Orientation.

There are two bolt holes in the attachment bar, which align with the top hole and the bottom arc of the angle selector. The attachment bar is a rectangular aluminum tube that connects the towed composite plate to the tow carriage. After tightening the top bolt, the bar can be moved along the arc until the intended plate angle is obtained. The bolt along the arc is then tightened to lock the plate orientation in place. This experiment was done for a vertical plate and with the plate at $\pm 30^\circ$.

The pulley system is connected to the front and rear of the carriage. The pulley wire is bolted to the rear of the carriage in a solid connection. Located on the front of the carriage is a Honeywell Model 41 “Pancake” type load cell. This load cell measures the force at which the pulley system tows the carriage. The other data obtained from this experiment was the strain experienced by the composite plate. The strain gauges were connected to quarter-inch bridge adapters. These adapters and the front load cell were connected to a National Instruments Wireless Sensor Network (WSN). The WSN only allowed for four channels of experimental data to be streamed for data storage to a laptop using a Wi-Fi connection. The four channels were occupied by three strain gauges and the front load sensor. The procedure for connecting the strain gauges to the quarter-inch bridge adapter can be found in Appendix B. The necessary equipment for data acquisition shown in Figure 10 can be found fixed to the top of the tow carriage.

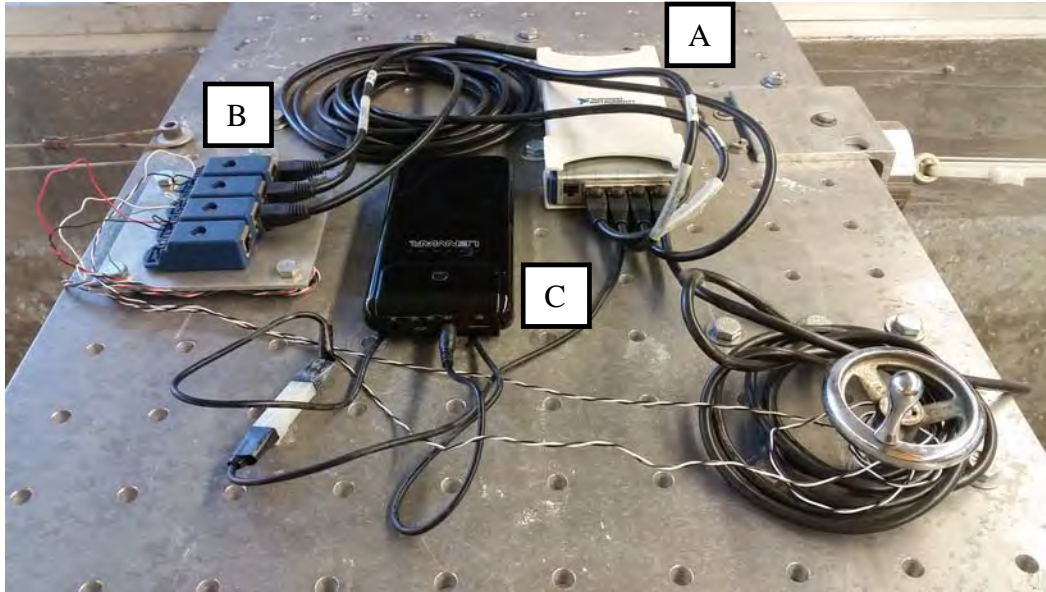


Figure 10. WSN (A), Quarter-Inch Bridge Adapters (B), and External Battery Pack (C) Used to Transmit Strain and Force Values for Data Storage.

The experimental data was recorded to the laptop using a program called Labview. The strain gauge factor was entered into the program in order to obtain valid strain measurements. The computer program display is shown in Figure 11. Example force data from an experimental trial is still displayed on the strip chart.



Figure 11. Labview Computer Program Used for Data Acquisition.

The gauge factor for each strain gauge is entered into the appropriate “GF Ch #” for each strain gauge. The default sample rates were used at 100 samples per second. Real time data can be viewed in the top strip chart. After each trial this chart was cleared of data. Selecting the “Save to File” button allowed for the experimental data to be saved as a tab delineated file which could be imported to excel for data reduction.

The data for each trial can be divided into three stages. The first is the acceleration stage. In this stage, the force peaks rapidly as the pulley system applied the initial force required to begin moving the carriage. The next stage is the steady state condition. At this point, the data is consistent and oscillates about an average value. This is the stage of interest. All data reduction will be conducted in this range of data. Last is the deceleration stage. This stage has the similar erratic behavior found in the acceleration of the carriage and will not be used for data reduction. The typical data for one trial is shown in Figure 12.

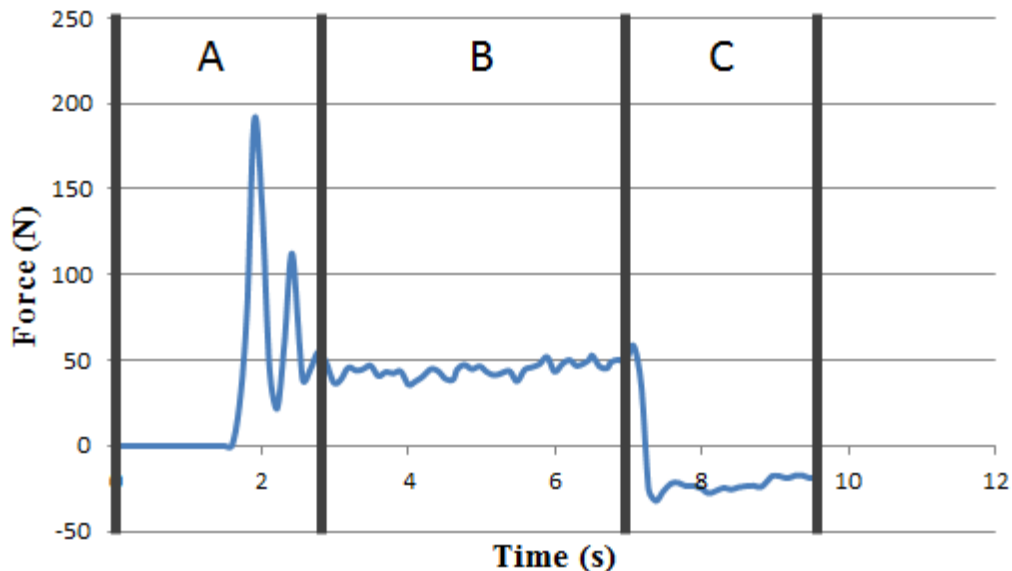


Figure 12. Data Obtained from Experimental Trials Divided into Acceleration Stage (A), Steady State Stage (B), and Deceleration Stage (C).

The data has been divided into the three stages. For each run, the steady state range will be visually selected to match the steady state behavior displayed in Figure 12.

The final data required for the experiment was the velocity of the carriage as it towed the composite plate through the water. This was obtained using an Olympus i-SPEED high-speed camera. In addition to the velocity measurement, the camera allowed for the flow characteristics of the ice equivalent around the plate to be assessed. The camera was placed in front of the glass viewing pane of interest. The average velocity was determined by dividing the distance the plate traveled in the camera's field of view by the total elapsed time required to cover the distance.

B. ICE EQUIVALENT

Ideally, this experiment would be done in an ice tank. An ice tank is a temperature-controlled facility that houses a towing tank. The temperature control allows the working area to remain below the freezing temperature of water, allowing the use of real ice for experiments. There are currently 11 ice tanks around the world. The largest is 102 meters long, 10 meters wide, and 2 meters deep which can be found in St. Petersburg, Russia. Since NPS does not have a climate controlled area, using ice was not possible. For this reason, a viable substitute had to be found which allowed for repeatability in all of the experimental trials. The main goal of this experiment was to match the density ratio between the fresh water tow tank water and the simulated ice to Arctic brash ice and Arctic Ocean seawater. This would give the most realistic floating characteristics for the ice equivalent for the experiment. Brash ice is the accumulations of floating ice made up of fragments not more than 2 meters across [16]. An example of a ship navigating through brash ice is shown in Figure 13.



Figure 13. Vessel Transiting through Brash Ice, from [17].

1. Research

To properly simulate Arctic ice, it is first necessary to have an understanding of the Arctic environment and the interaction between the ice and sea water. When sea water freezes, the salt and the water separate into two different phases: brine and ice. If the salt is captured inside the body of ice, it remains as a pocket of brine. Brine is a salt water mixture with a very high concentration of salt. Any salt that is not physically contained inside the ice dissolves back into the Arctic Ocean [18]. This characteristic results in sea ice having a large range of density values. Numerous density measurements of sea ice have been compiled by Frederking and Timco [19] and are shown in Table 1. The density of sea ice ranges from 720 kg/m^3 to 960 kg/m^3 . Most recorded values are nearest to the upper limit of that range.

Table 1. Density Measurements of Sea Ice, from [19].

Investigator	Measurement technique	Density range Mg m^{-3}	Density (above waterline) Mg m^{-3}	Density (below waterline) Mg m^{-3}	Brine drainage
<i>First-year sea ice</i>					
Malmgren (1927)	—	0.914 to 0.924	—	0.914 to 0.924	NO
Butkovich (1956)	mass/volume	0.78 to 0.92	0.85 to 0.92	0.88 to 0.92	YES
Weeks and Lee (1958)	mass/volume	0.77 to 0.96	—	0.86 to 0.91	YES
Langleben (1959)	mass/volume	0.84 to 0.90	0.84 to 0.90	0.90 to 0.93	NO
Pounder and Little (1959)	specific gravity	0.81 to 0.91	—	—	YES
Pounder and Stalinski (1960)	specific gravity	0.943 ± 0.02	—	—	YES
Brown (1962)	specific gravity	0.92	—	0.92	NO
Langleben and Pounder (1962)	displacement	0.884 to 0.91	0.884	0.91	YES
Kohnen (1972)	mass/volume	0.90 to 0.92	—	0.90 to 0.92	NO
Nakawo (1983)	displacement	0.88 to 0.92	0.88 to 0.91	0.90 to 0.92	NO
Timco and Frederking (1983)	mass/volume	0.904	—	0.904	NO
Sinha (1984)	mass/volume	0.90 to 0.91	0.90 to 0.91	0.90 to 0.91	NO
Sinha (1986)	mass/volume	0.90 to 0.91	0.90 to 0.91	0.90 to 0.91	NO
Timco and Frederking (1986)	mass/volume	0.76 to 0.89	—	—	YES
Urabe and Inoue (1986)	mass/volume	0.75 to 0.88	0.75	0.88	YES
<i>Multi-year ice</i>					
Malmgren (1927)	—	0.857 to 0.893	0.857	0.885 to 0.893	YES
Langleben and Pounder (1962)	displacement	0.91	—	—	—
Cherepanov (1966)	—	0.912 to 0.917	0.912 to 0.915	0.915 to 0.917	NO
Kovacs and Mellor (1971)	—	0.84 to 0.94	0.84 to 0.88	0.90 to 0.94	NO
Hibler et al. (1972)	—	0.910 to 0.915	—	—	—
Sinha (1984)	mass/volume	0.72 to 0.90	0.72 to 0.85	0.89 to 0.90	NO
Jeffries et al. (1988)	mass/volume	0.87 to 0.912	—	—	—

With the density of sea ice known, it was then necessary to find the density of Arctic Ocean seawater. The density of salt water is a function of its temperature and salinity according to the Equation of State of Seawater [20]. In order to obtain values for temperature and salinity, the NOAA database was accessed. The database requires a season and a depth in order to display the expected data for salinity and water temperature. Since Arctic sea lanes would be most accessible in Spring and Summer, those times were selected. The surface layer was selected for depth. The results for the salinity and temperature are found in Figure 14 and Figure 15, respectively.

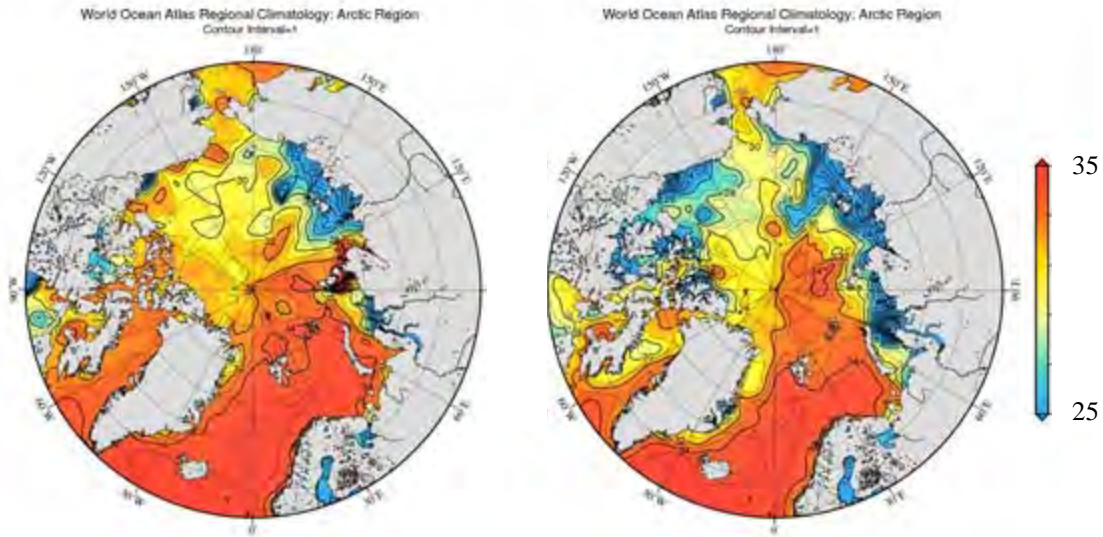


Figure 14. Expected Surface Layer Practical Salinity Unit (PSU) in the Arctic Region Published by NOAA, after [21].

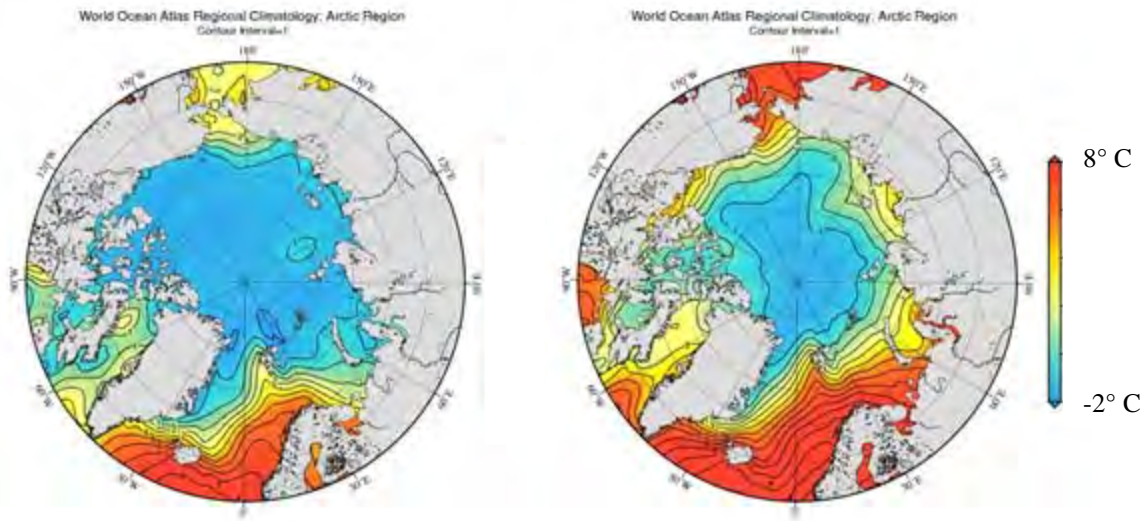


Figure 15. Expected Surface Layer Temperature (°C) in the Arctic Region Published by NOAA, after [21].

This data shows that the salinity varies from 29–35 PSU and the temperature varies from -2°C to 6°C . The maximum extreme of the density value results from the low temperature, high salinity water. The opposite results in the minimum extreme density value. Using the Equation of State of Seawater, the density of the Arctic seawater values

ranged from 1022.8 kg/m^3 to 1028.2 kg/m^3 . This results in a final density ratio of sea ice to Arctic Ocean seawater ranging between 0.70 and 0.94.

In order to get the correct floating behavior of the simulated ice in the fresh water tow tank, the density ratio between the ice and ocean water must match the simulated ice and the tow tank water. It was first assumed that the water used in the tow tank had the typical density of 1000 kg/m^3 common to freshwater. This meant the simulated ice must have a density ranging from 700 kg/m^3 to 940 kg/m^3 . The material must also not absorb the water, as that would change its density during testing. After searching various materials, two seemed best for the experiment. The first was High Density Foam (HDF) machining board, which is common in model making. The next was Low Density Polyethylene (LDPE) plastic. After researching cost, resistance to water absorption, and handiness, LDPE was chosen as the material to simulate ice. LDPE could be ordered in the shape of a rod whereas the HDF would have to be machined into an ice shape from a large rectangular block. The rods simply had to be cut every few inches to create the simulated ice. McMaster Carr advertised a density of 913 kg/m^3 for the LDPE [22]. This fit well in the desired range of ideal densities.

2. Fabrication

In order to fulfill the ice requirements for the desired experiments, two different-sized rods were ordered. Two-inch diameter rods were ordered which would simulate a ship moving through a field of small randomly dispersed sea ice masses. Larger four-inch diameter rods were purchased to simulate impacts with large bodies of ice. The LDPE rods are shown in Figure 16.



Figure 16. LDPE Rods Used to Simulate Arctic Ice.

The density of the LDPE and the tow tank water was then verified to ensure the experiment properly represented the Arctic environment. First, each rod was weighed using a large electric scale, as shown in Figure 17.



Figure 17. Electric Balance Used in Density Measurements.

Then, the diameter of each rod was measured at the top, middle and bottom using calipers. The rod diameter is shown in Table 2.

Table 2. Diameter Variations along LDPE Rods.

Rod Number	1	2	3	4	5	6
Top Diameter (mm)	51.47	51.49	51.43	51.53	51.48	51.44
Mid Diameter (mm)	51.46	51.46	51.43	51.46	51.43	51.45
Bottom Diameter (mm)	51.43	51.45	51.44	51.56	51.39	51.40
Average (mm)	51.453	51.466	51.433	51.517	51.433	51.43

Finally, the length of the rods was measured and their densities calculated. The final results are shown in Table 3.

Table 3. Density Calculation Summary.

Rod Number	1	2	3	4	5	6
Mass (kg)	2.3423	2.3445	2.3471	2.3472	2.35333	2.35587
Length (m)	1.2192	1.2200	1.2208	1.2224	1.2256	1.2287
Average Diameter (m)	0.051453	0.051466	0.051433	0.051517	0.051433	0.05143
Volume (m ³)	0.002533	0.002538	0.002536	0.002548	0.002546	0.002553
Density (kg/m ³)	924.8	923.8	925.4	921.2	924.2	922.9

The final average density of the LDPE was 923.7 kg/m³. This is slightly above the published density is 913 kg/m³. A graduated cylinder and an electric balance were then used to determine the density of the water in the tow tank. This is shown in Figure 18.



Figure 18. Graduated Cylinder and Scale Used for Water Density Measurements.

The tank was filled and allowed ample time to reach temperature equilibrium with the ambient air. Three different trials were done with water taken from the middle and outer edges of the tow tank. The density results are shown in Table 4.

Table 4. Density Results for Tow Tank Water.

	Volume (ml)	Mass (g)	Density (kg/m ³)
Fill End	93.0	92.3	992.4
Middle	98.8	97.5	986.8
Drain End	97.3	96.3	989.7
			Average = 989.7

The final density ratio between the LDPE and the tow tank water was 0.933. The expected value of 0.913 for the density ratio between the LDPE and water would have

been more ideal for the experiment since it was closer to the majority of recorded sea ice density values; however the actual density ratio used in the experiment still fell into the range of density ratios actually recorded for sea ice.

In order to have consistent floating characteristics, the rods were cut into various lengths and placed in the tow tank. The two-inch diameter rod was cut into segments ranging from one inch to two-and-a-half inches, at half-inch intervals. The resulting floating characteristics are shown in Figure 19.

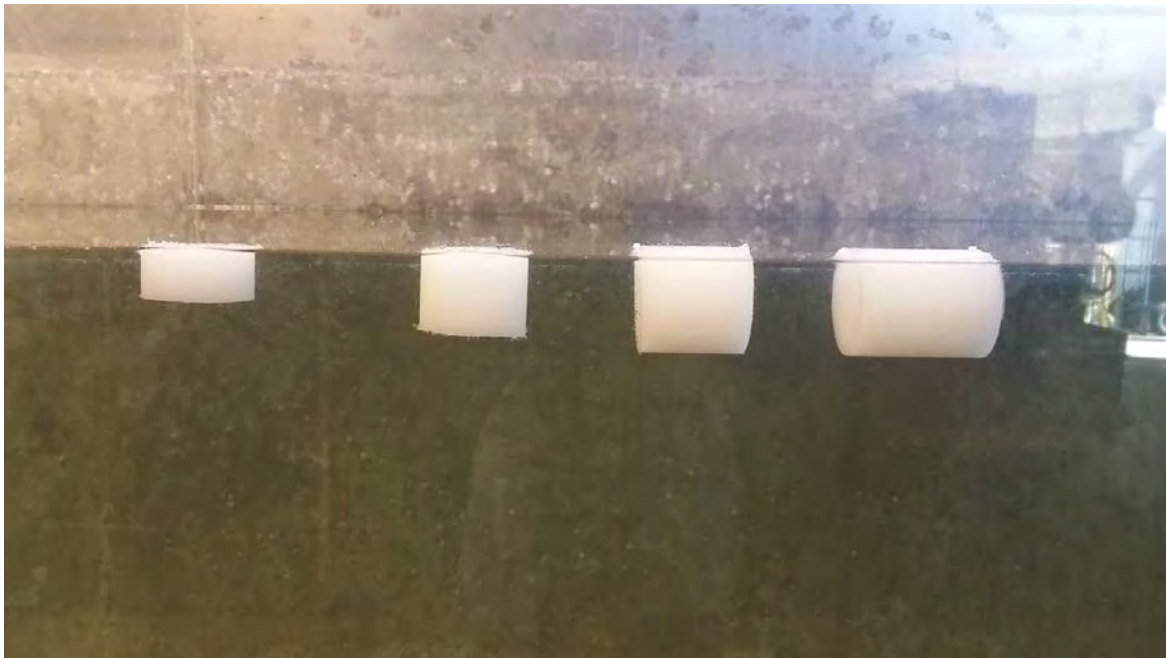


Figure 19. Floating Characteristics of Rods with Lengths 25.4 cm, 38.1 mm, 50.8 mm, and 63.5 mm (1.0 in, 1.5 in, 2.0 in, 2.5 in).

The 38.1 mm (1.5 in) long segment was the longest section that had self-righting properties. The rods were cut using a table mounted buzz saw. Since many cuts were required, a vertical piece of metal was C-clamped to the work bench at a distance from the buzz saw that ensured the rods were cut into 38.1 mm (1.5 in) segments. The setup is shown in Figure 20. This setup allowed the rod to be continuously fed into the buzz saw while also being cut to a near-perfect length.



Figure 20. Small Diameter LDPE Rod Cutting Setup to Maximize Efficiency.

The larger four-inch diameter rods were cut using a vertical band saw. After completing a similar float test to the one mentioned above, the large diameter rod was cut to a length of 76.2 mm (3 in).

C. SIMULATION OF OPERATIONAL ENVIRONMENT

This thesis simulated both small-scale and large-scale collisions between a composite hull and free-floating ice. The small-scale ice was represented by 38.1 mm (1.5 in) long LDPE rod sections with a diameter of 50.8 mm (2 in). The large-scale ice was represented by 76.2 mm (3 in) long LDPE rod sections with a diameter of 101.6 mm (4 in). Multiple scenarios for each ice equivalent size were completed.

1. Small-Scale Ice Interaction

This experiment utilizes two different sizes of simulated ice in order to account for different ice conditions that a vessel may encounter in Arctic sea lanes. The first sea state involves a large quantity of small pieces of ice, as shown in Figure 21.



Figure 21. Small-Scale Ice Present in Arctic Waters, from [23].

The two-inch diameter rods were used to simulate this environment. To ensure repeatability between experiments, a specific surface capacity of LDPE rods was used to determine how many rod sections should be placed in a section of the tow tank. The surface capacity was calculated by dividing the product of the number of rods and the area of each rod by the maximum area of the rectangular section in the tow tank that could be occupied by the circular ice equivalent. The length of the glass panels of the tank determined the length of the area occupied by the ice equivalent. Each glass panel is 37 inches long. The glass panel allows for the use of the high speed camera to observe flow characteristics and the interaction between the towed plate and the ice equivalent. This experiment included low, medium and high ice capacity trials. The experimental setup is for the different surface densities are shown in Figure 22. The green line represents the towed composite plate.

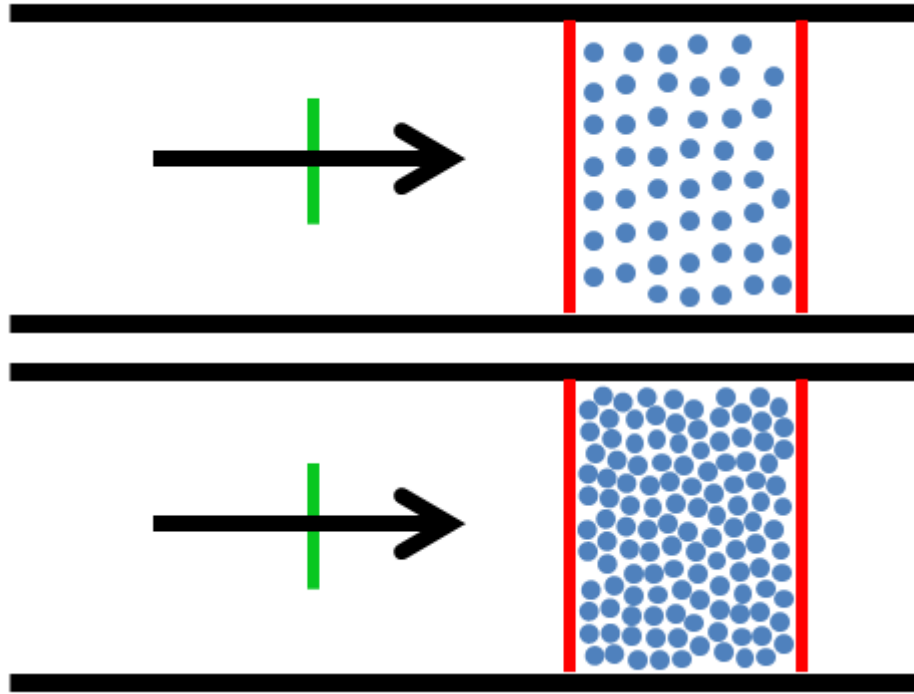


Figure 22. Experimental Schematic to Simulate Conditions in Figure 21.

In order to accomplish this experimentally, the number of rods required to fulfill the surface density requirement were dumped into the tow tank. They were allowed to float randomly within the 37-inch long section of the tow tank. Enough time was given for the rods and tow tank water to reach an equilibrium state.

2. Large-Scale Ice Interaction

The second simulated Arctic operating environment accounted for large free-floating ice that may be present in sea lanes. The goal was to model the impact between one or two large pieces of ice with the composite hull. This operating area would be similar to that shown in Figure 23.



Figure 23. Scattered Large-Scale Ice Present in Arctic Waters, from [24].

Multiple possible impact situations were assessed using the large-diameter LDPE rods. These include a single centered strike, a single off-centered strike, and a double impact. The tow tank schematics in Figure 24 display the different impact situations. These scenarios were completed for the three different hull angles. Videos were taken to qualitatively assess the interaction with each hull shape and the LDPE rods.

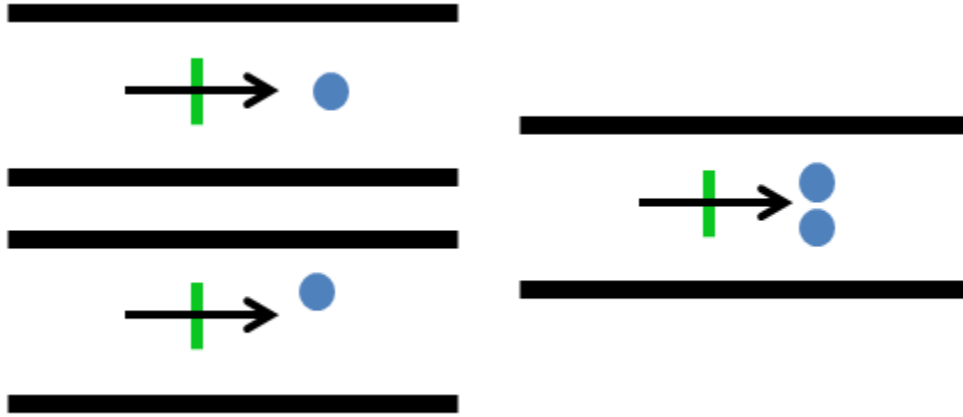


Figure 24. Experimental Schematic to Simulate Conditions in Figure 23.

D. COMPOSITE PLATE FABRICATION

The composite plate used in the tow tank experiment was made using woven glass fabric, resin, and hardener. First, the woven glass fabric was cut to size. Since the plate would be subjected to notable hydrodynamic forces it was decided that the plate would be 10 layers thick. The desired plate dimensions were 30.5 cm by 30.5 cm (12 in by 12 in). Since the woven glass has the potential to move slightly during the layup process, the woven glass fabric was cut into 10 squares with a side length of 13 inches using a sharp cutting wheel. The setup is shown in Figure 25.

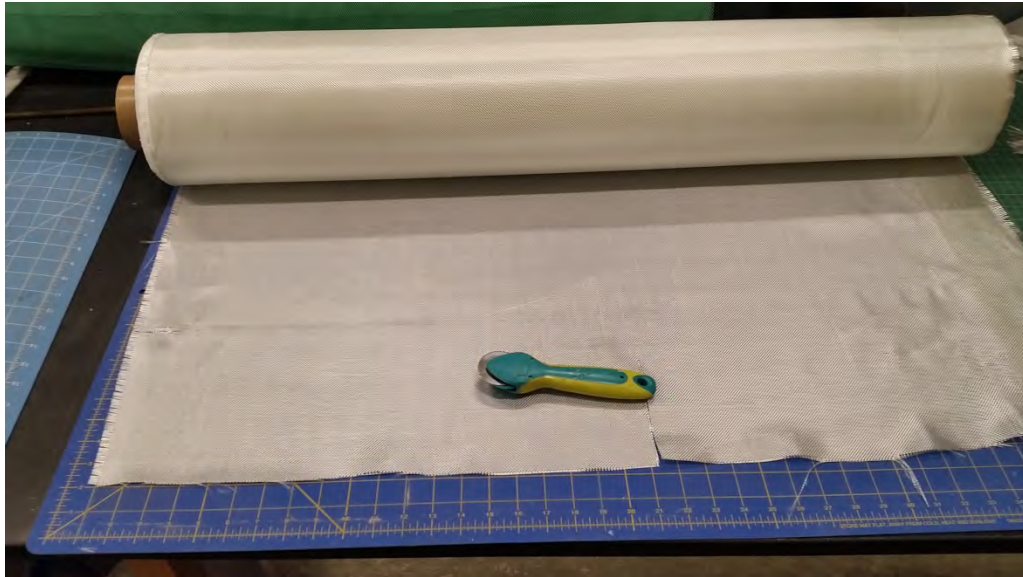


Figure 25. Cutting Wheel Used to Cut Woven E-Glass Sheet.

Next, other necessary materials that were required for the composite plate layup were cut to size. These include release ply paper, nylon peel ply, perforated release ply, bleeder cloth, and a vacuum bag. With the exception of the vacuum bag, these were all cut into squares with a side length two inches longer than the woven glass fabric. This ensured that any excess epoxy would not adhere to the table on the bottom side and would be absorbed by the bleeder cloth on the top. With the necessary materials ready for layup, the resin and hardener were mixed according to the manufacturer's instructions. Pro-Set M1002 Resin and Pro-Set 237 Hardener were used. The two were mixed for five minutes using a weight ratio of 100:24. These were mixed in a mixing container inside of a fume hood. The setup is shown in Figure 26. The table used for layup consists of a large glass pane resting on top of a work bench. The workbench used is shown in Figure 27.

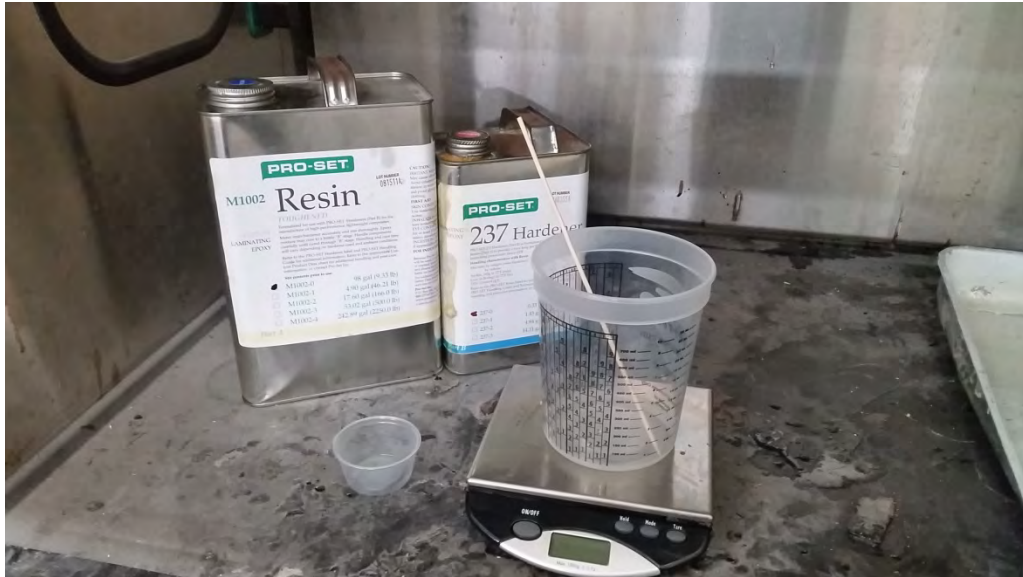


Figure 26. Resin and Hardener Mixed by Weight Ratio in Mixing Container.



Figure 27. Workbench Used for Composite Plate Layup.

To begin, the glass work area was cleared using a metal scraper. The bottom layer consisted of one layer of release ply paper which prevented the plate from curing to the glass work table. Next, a base layer of epoxy was rolled evenly onto the ply paper using the metal roller shown in Figure 27. Alternating layers of glass fiber and epoxy were rolled until the ten layers were completed. Next, the nylon peel ply, perforated release

ply, and bleeder cloth were placed on top. The bleeder cloth absorbed any excess epoxy applied during the rolling process. Finally, a large vacuum bag is sealed around the entire set up using double sided tape. The electrical pump was used to create a vacuum of 15 mmHg. The plate was given 24 hours to cure. The plate was then cut to size in the machine shop. Holes were drilled where the plate was to be bolted to the tow carriage bar.

E. APPLICATION OF STRAIN GAUGES

Strain gauges were used to measure the strain experienced during each of the scenarios depicted in Section C. As mentioned before, the data acquisition system can only transmit data from three strain gauges. For this reason, an Ansys model was created to visualize the strain incurred by the pressure of the water against the front face of the composite plate. The strain gauges were placed in accordance with the results of the Ansys model. The strain gauges were then applied using a series of epoxy and protective coatings which allowed the strain gauges to operate in the presence of water.

1. Determining Strain Gauge Location

First, it was necessary to determine the critical location on the plate where the hydrodynamic forces cause the most deformation in the plate. The data acquisition can only record data from three strain gauges, so the location cannot be chosen haphazardly. In order to do this, a simplified static structural simulation was done in Ansys to obtain qualitative information regarding the strain profile resulting from moving the plate through water. The plate was created in Solidworks and imported into Ansys. The mechanical properties of the E-glass were input into the engineering data. The data was obtained from a prior NPS thesis that used the same E-glass [25]. A fixed support was placed on the back of the plate where the attachment bar is bolted in place. Figure 28 shows the simulation and the experimental setup.

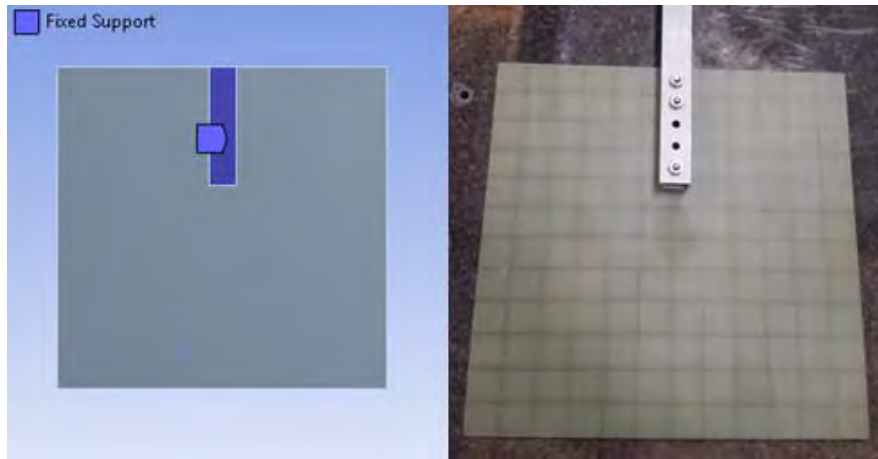


Figure 28. Ansys Boundary Condition Relationship to Composite Plate.

Next, a pressure was added to the front of the plate at the intended water level for experiment. Since this simulation was done before testing, the added height of the bow wave preceding the plate was not accounted for. Figure 29 shows the relationship between the hydrodynamic pressure in the experiment and the ANSYS model.

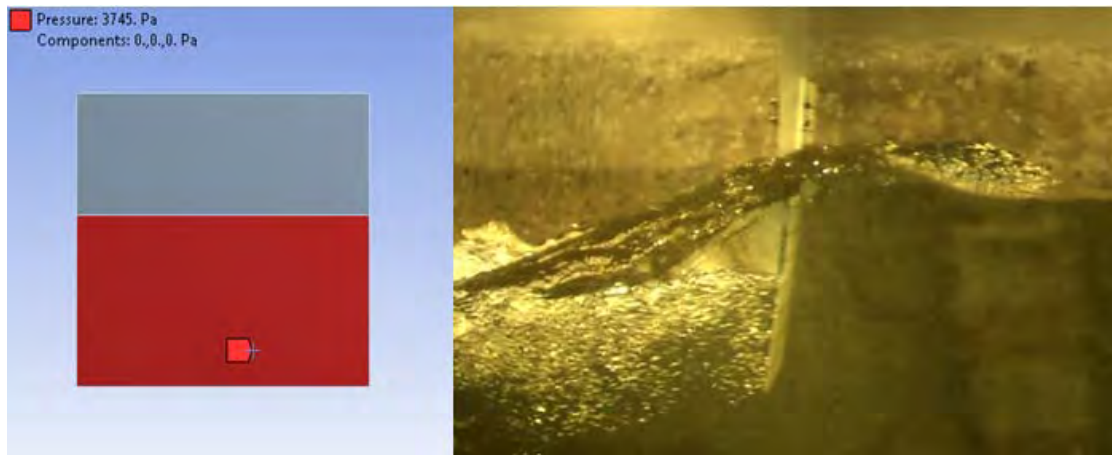


Figure 29. Hydrodynamic Pressure Resulting from Towing Plate.

ANSYS was used to solve for the equivalent Von-Mises stress in the plate. The results are shown in Figure 30. In order to have a better understanding of the location of the fixed support, the setup image is shown next to the final results.

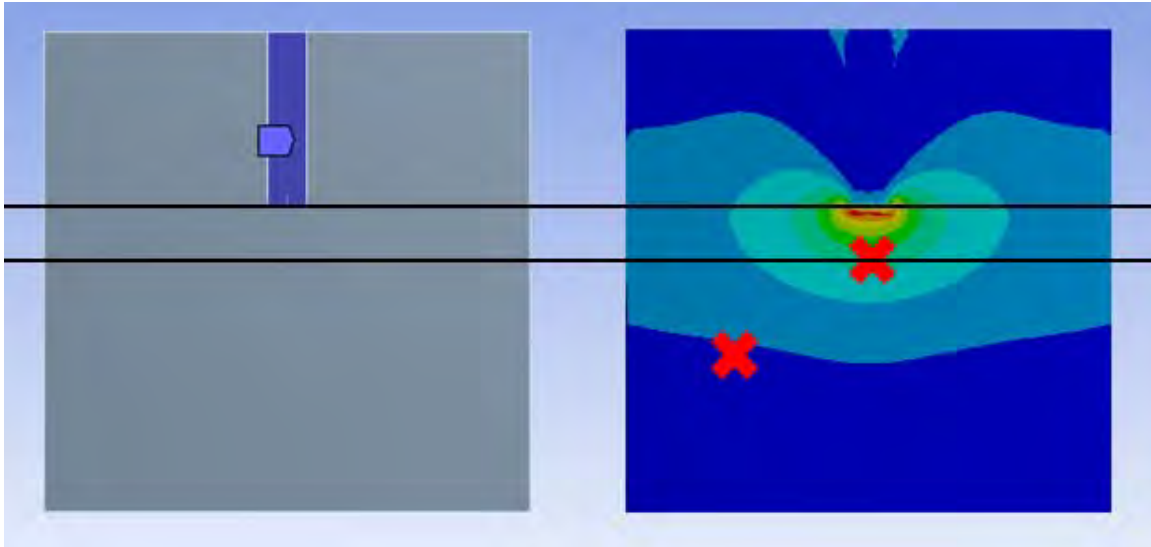


Figure 30. Location of Strain Gauges Noted by Red X's on Stress Profile.

This image shows the strain is greatest just below the attachment bar. Since wires had to be soldered to the strain gauges they could not be placed directly underneath the attachment bar. The top line indicates how far the attachment bar extended onto the plate, which was 11.18 cm (4.4 in) from the top of the plate. The bar was 2.54 cm (1 in) wide. The second line shows the plane on which the first strain gauge was placed. A strain gauge capable of measuring strain in the vertical direction was placed on the centerline of the plate at this location. One 90° Tee Rosette capable of measuring strain in both the vertical and horizontal directions was placed midway between the center and the side and midway from the first strain gauge to the bottom of the plate. The locations of the strain gauges on the framed composite test plate had an impact on the locations of the strain gauges as well. This allowed for the strain resulting from the two different boundary conditions to be assessed.

2. Strain Gauge Application

With the location of the strain gauges established, the plate was prepared for the bonding agent. The location of each strain gauge was just above the five-inch grid line. The procedure is listed below.

1. Cleaning Strain Gauge Location: The two strain gauge locations were sanded with fine sand paper to ensure the bonding surface was clean of

any imperfections and any contaminants that might result in delamination of the strain gauge. The area was then cleaned with ethanol and a gauze pad. This cycle was repeated twice.

2. Placement of Strain Gauges: Using tweezers, the strain gauges were moved into place. Scotch Tape was then placed over the strain gauges and then peeled back into a loop. This allows the bonding agent to be applied to the underside of the gauge while ensuring the strain gauge will remain in its intended location. The end result of this process is shown in Figure 31.

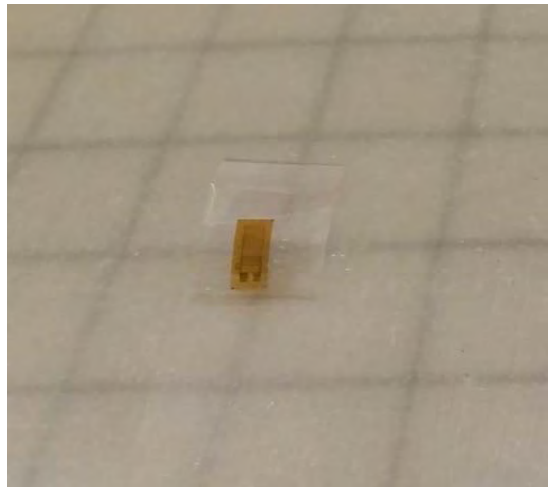


Figure 31. Taped Back Strain Gauges Prior to Application of Bonding Agent.

3. Application of Bonding Agent: An M-Bond AE-10 Adhesive Kit manufactured by Micro-Measurements was used to adhere the strain gauge to the composite plate. The kit consists of a two part epoxy, a dropper, and a plastic stirring rod. The dropper was filled up to the preset mark with hardener. The hardener was added to the small jar of resin. After finishing the required five minute mix time, a very small amount of epoxy was applied to the strain gauges. The tape was then unlooped and pressed against the plate firmly.
4. Curing Time: Weights were placed on top of the strain gauges to ensure they remain flush against the surface. This is shown in Figure 32. While the epoxy does partially cure in six hours, it was given 48 hours to achieve its maximum elongation capabilities. This will ensure that when the plate is flexed from the hydrodynamic forces, the strain gauge will not experience delamination from the plate's surface.



Figure 32. Application of Weights to Ensure Proper Bonding between Strain Gauges and Composite Plate.

5. Soldering Leads: After the 48 hour cure time, the tape was removed. This exposed the terminals to which the wire that connects the gauge to the sensor is applied. After ensuring the terminals were clean with a dental pick, the leads were then soldered to the terminals.
6. Waterproofing: There were two coats required to properly insulate the strain gauge and wire connection from the tow tank water. The first was a general purpose laboratory coating called M-Coat A. A liberal coating was applied over the entire strain gauge and exposed wire. This coat was allowed to cure for 6 days as recommended by the manufacturer. Next, Dow Corning MIL-A-461 RTV Coating, a room temperature curing silicone rubber, was generously applied on the strain gauge and wire connection. The wires were then routed through the attachment bar. This eliminates the need to tape the wires to the attachment bar. The waterproofed strain gauges are shown in Figure 33.

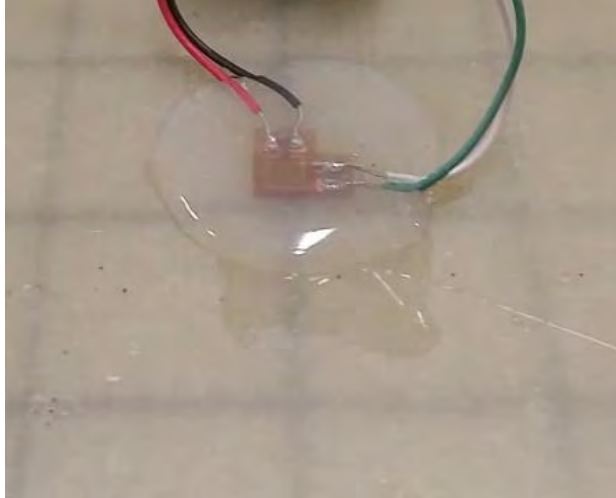


Figure 33. Waterproofed Strain Gauges.

F. TEST PLAN

The goal of this experiment was to characterize how well each hull performed in the presence of the different-sized ice equivalent. This test plan was completed with both the framed composite plate and the frameless plate. The framed composite plate is shown in Figure 34. The strain experienced by the framed plate is expected to decrease for all trials when compared to the strain experienced by the frameless plate.

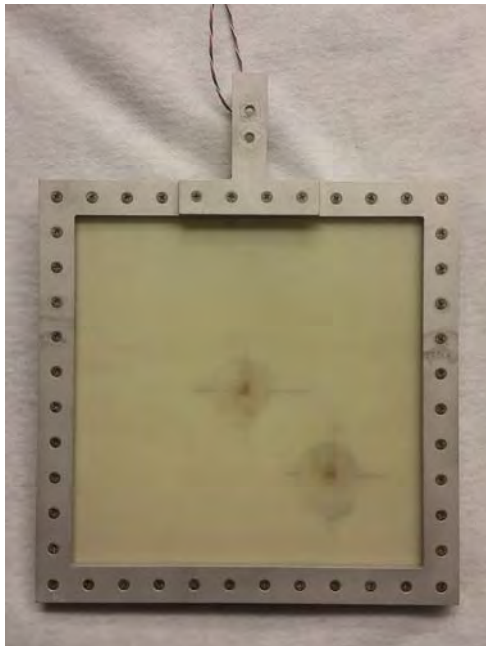


Figure 34. Framed Composite Plate Used in Testing.

In order to compare performances of each hull type, the strain experienced by the plate and the force required to travel through the media were recorded for the base water trials, 50% ice capacity, and for an impact with two large piece of ice. Additional trials for smaller ice densities were completed to determine the relationship between increasing ice density and the resultant forces and strain values. The other situations described in the Ice Equivalent section were also tested. The full test plan followed to obtain the necessary data is shown in Table 5. Figure 35 shows the difference between the tumblehome orientation and the conventional orientation. As mentioned before, the two orientations will be angled at 30°.

Table 5. Test Plan.

Run	Trial Type	Desired Data	Speed/Orientation
1	Base Air Trials	Force	3 Hz / Vertical
2			5 Hz / Vertical
3			7 Hz / Vertical
4			9 Hz / Vertical
5	Base Water Trials	Force, Strain, Velocity	3 Hz / Vertical
6			5 Hz / Vertical
7			7 Hz / Vertical
8			9 Hz / Vertical
9			3 Hz / Tumblehome
10			5 Hz / Tumblehome
11			7 Hz / Tumblehome
12			9 Hz / Tumblehome
13			3 Hz / Conventional
14			5 Hz / Conventional
15			7 Hz / Conventional
16			9 Hz / Conventional
17	16.67% Capacity Small Ice Trials	Force, Strain	9 Hz / Vertical
18			9 Hz / Tumblehome
19			9 Hz / Conventional
20	33.3% Capacity Small Ice Trials	Force, Strain	9 Hz / Vertical
21			9 Hz / Tumblehome
22			9 Hz / Conventional

Table 5 (cont'd) Test Plan.

Run	Trial Type	Desired Data	Speed/Orientation
23	50% Capacity Small Ice Trials	Force, Strain, Video	3 Hz / Vertical
24			5 Hz / Vertical
25			7 Hz / Vertical
26			9 Hz / Vertical
27			3 Hz / Tumblehome
28			5 Hz / Tumblehome
29			7 Hz / Tumblehome
30			9 Hz / Tumblehome
31			3 Hz / Conventional
32			5 Hz / Conventional
33			7 Hz / Conventional
34			9 Hz / Conventional
35	Single Centered Large Ice Trial	Force, Strain, Video	9 Hz / Vertical
36			9 Hz / Tumblehome
37			9 Hz / Conventional
38	Single Off-Centered Large Ice Trial	Force, Strain, Video	9 Hz / Vertical
39			9 Hz / Tumblehome
40			9 Hz / Conventional
41	Double Centered Large Ice Trial	Force, Strain, Video	3 Hz / Vertical
42			5 Hz / Vertical
43			7 Hz / Vertical
44			9 Hz / Vertical
45			3 Hz / Tumblehome
46			5 Hz / Tumblehome
47			7 Hz / Tumblehome
48			9 Hz / Tumblehome
49			3 Hz / Conventional
50			5 Hz / Conventional
51			7 Hz / Conventional
52			9 Hz / Conventional

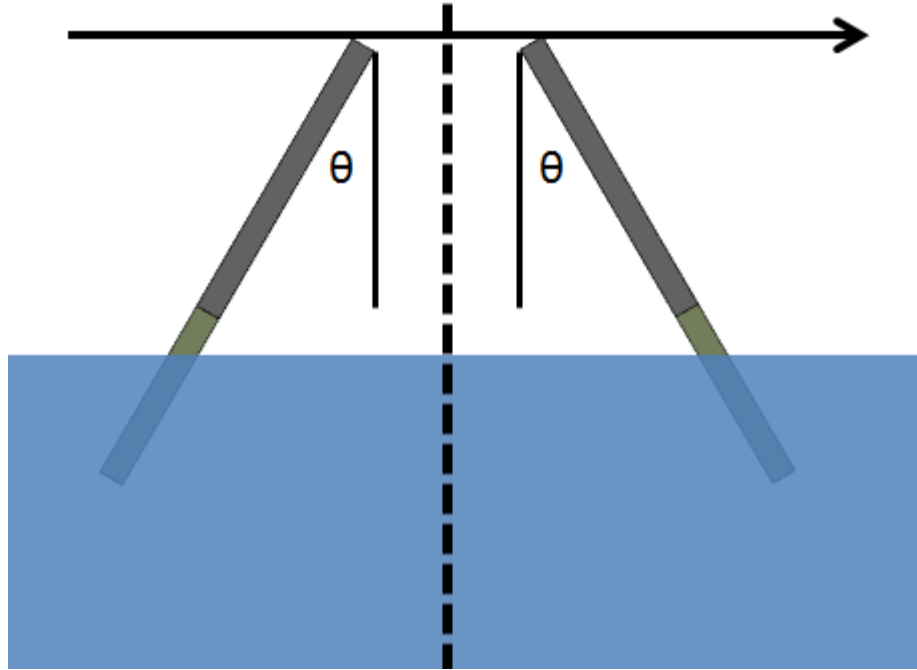


Figure 35. Conventional Hull (Left) and Tumblehome Hull (Right) with $\theta=30^\circ$.

G. PROCEDURE

Before each trial, the carriage was positioned near the left end of the tow tank. This ensured that the carriage reached steady state conditions when it arrived at the center of the tank. This was important since the ice equivalent would be placed near the center of the tank. Using previous NPS tow tank experimental data [25], test speeds of 3 Hz, 5 Hz, 7 Hz, and 9 Hz were chosen. According to previous data, these inputs should result in carriage velocities ranging from 0.40 m/s to 1.11 m/s. Approximately one m/s was desired as a maximum carriage speed for safety consideration due to the short length of the tow tank. The first step was to verify the speed results from the previous tow tank experiments.

The speed of the carriage was determined using the high speed camera. Since the plate glass and the water refract the visible light in accordance to Snell's Law, the distance the plate traveled in the video could not be perfectly calculated. For this reason, the distance traveled by the plate was determined experimentally. The camera was set up at the distance which allowed the entire glass pane to be in view. The plate was moved

just into view of the camera and stopped. The nearest vertical edge of the plate was the point of reference. The starting location was marked on the tow tank. Next, the plate was moved across the field of view of the camera and stopped at the far right of the camera's field of view. At this point, only the rear bolts of the attachment bar were visible. The final location was marked on the tow tank and the distance between the two points were measured. Figure 36 shows the imaging process used to determine the distance traveled by the plate.

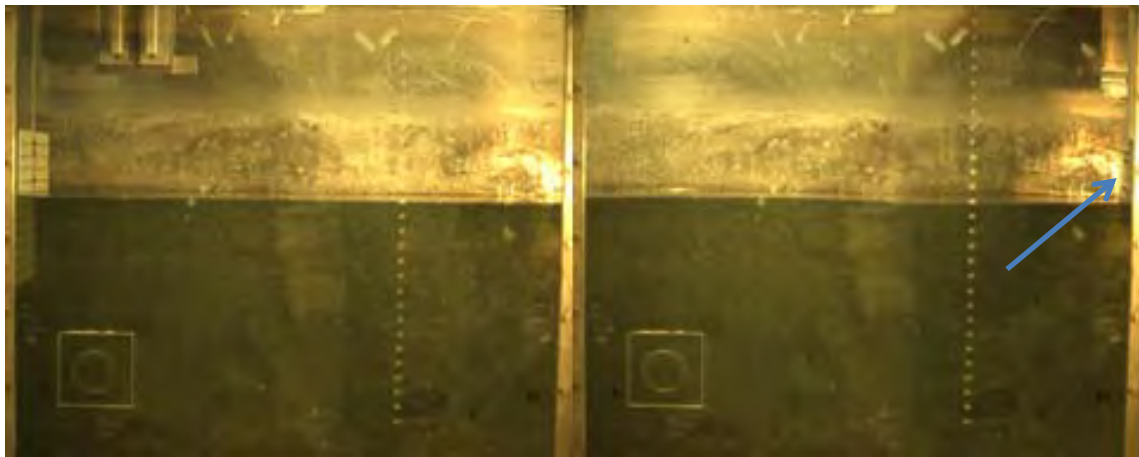


Figure 36. Beginning and End Locations Used for Measuring Average Speed.
Only the Attachment Bar Bolts are Visible as Indicated by the Arrow.

It was determined that the carriage travelled 1.07 m (42.2 in) to pass through the camera's field of view. The time stamp of the frame at the beginning and end of each trial was recorded to determine the average velocity of the carriage. The velocity of the carriage for each speed setting is shown in Figure 37.

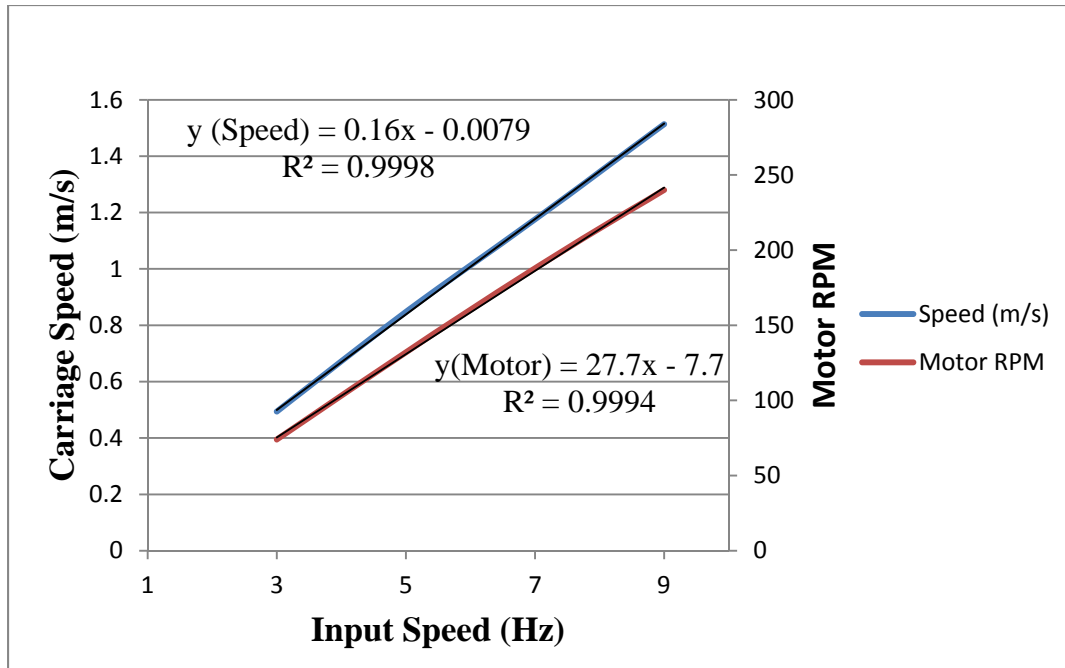


Figure 37. Correlation between Input Speed Setting (Hz) and both Velocity (m/s) and Motor RPM.

With the plate velocity known for the four desired speed inputs, the experiments described previously in the test plan were conducted. The base trials without the ice equivalent were straight forward. In order to complete the trials with the two-inch diameter LDPE, the 94 cm (37 in) section of the tow tank in front of the high speed camera was isolated with two wooden rods. The LDPE sections were placed into three different groups. Each group contained 54 rods, which equated to a 0.1667 ice density ratio for the tow tank segment. When all rods were added to the tow tank section, it was at 50% capacity. The term capacity is used because it is impossible to fully cover a rectangular area with circles. A 100% capacity would be the maximum number of LDPE rods that could be placed inside the ice section. The actual percent area of the section covered by the ice equivalent at 50% capacity is 37.5%. A rectangular pattern of circles was used for this calculation. All trials for the various hull orientations were completed first for the lower ice density. Time was allowed between trials for the tow tank water and LDPE rods to reach a state of rest. Upon the completion of the low ice density ratio testing, the additional LDPE segments required for higher ice density ratio were added to the tow tank. The experimental setup before each trial is shown in Figure 38.



Figure 38. Setup for 50% Capacity Small Ice Trials.

Next, the four-inch diameter LDPE chunks were added to the tow tank in accordance with the test plan. In order to ensure the LDPE segment remained in place, holes were drilled near the top of the rods. A small loop of soldering wire was inserted in one of the rods for the single strike tests. Two other rods were connected with a small length of soldering wire at the desired separation length. The wire was loosely placed in the second rod so the bow wave would separate the two rods from each other. Soldering wire was used because it deforms easily. The attachments are shown in Figure 39.

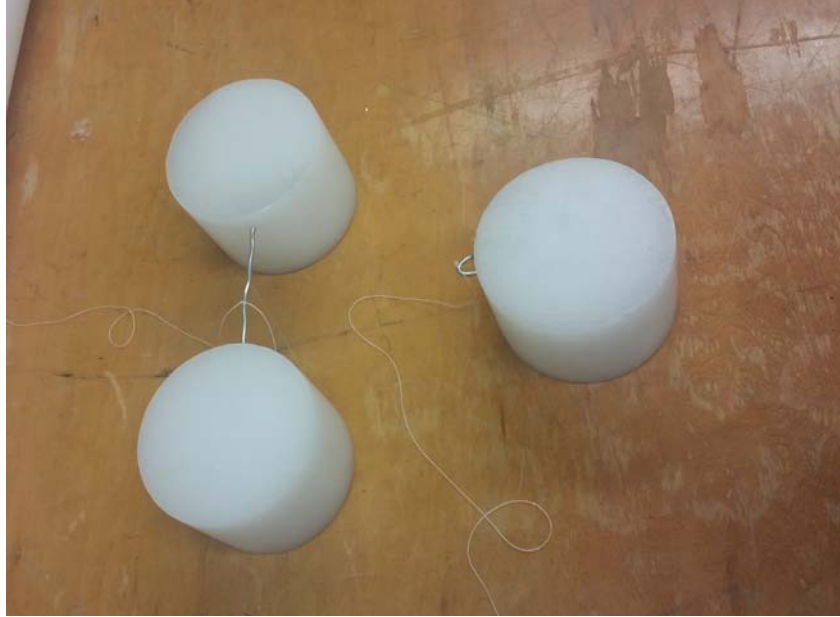


Figure 39. Soldering Wire Attachments to Aid in Stabilizing Large Ice Equivalent.

A length of thread was attached to the soldering wire. The thread was then connected to the pulley system, which was located along the centerline of the tow tank. Once the rods came to a state of rest at the center of the tank, the line was removed from the pulley system. The dangling thread was assumed to have a negligible effect on the experiment. The rod had to be manually placed for the off-centered single strike impact test. If the footage showed the rod moved out of location, the trial was repeated. The setup for the large ice impact tests is shown in Figure 40.

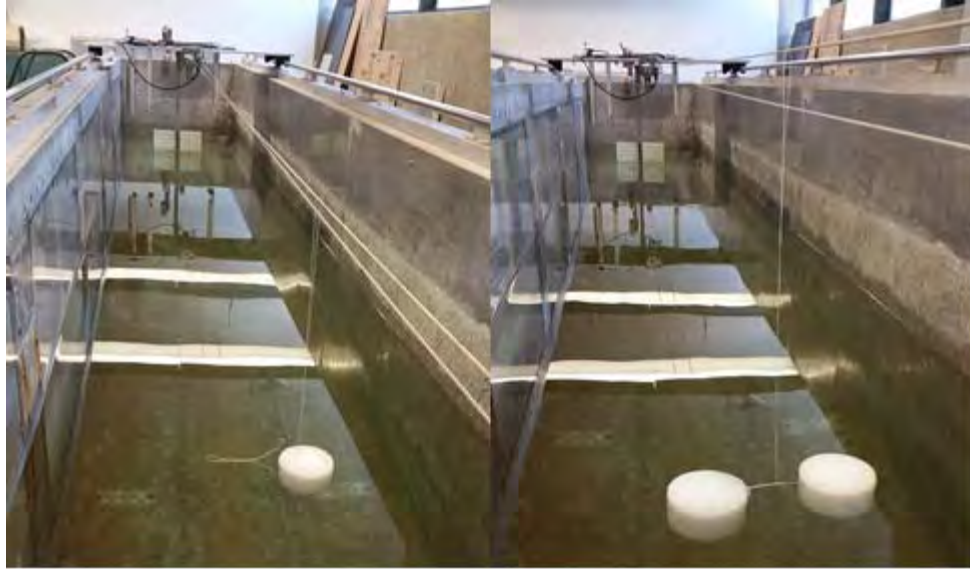


Figure 40. Large-Diameter Impact Test Setup.

Once all of the experimental data was obtained, a Go-Pro was attached to the bottom of the plate. The Go-Pro was used to record underwater footage of the area immediately preceding the plate. The goal was to capture the interaction between the bow wave of various hull types and the ice equivalent in the plate's path. The composite plate with the Go-Pro is shown in Figure 41.



Figure 41. Go-Pro Used to Record Underwater Footage.

THIS PAGE INTENTIONALLY LEFT BLANK

III. RESULTS

A. EXPERIMENTAL DATA REDUCTION

This experiment resulted in 104 Excel spreadsheets of raw experimental data. The data for each trial consisted of the force required to pull the carriage and the values recorded by the three strain gauges. First, there was a permanent bias in the force sensor attached to the front of the carriage. This was removed by subtracting the bias from the data sets. The tension experienced by the load sensor was recorded as a negative value. For this reason, the force data was also inverted. An example of the raw for and force data is shown in Figure 42.

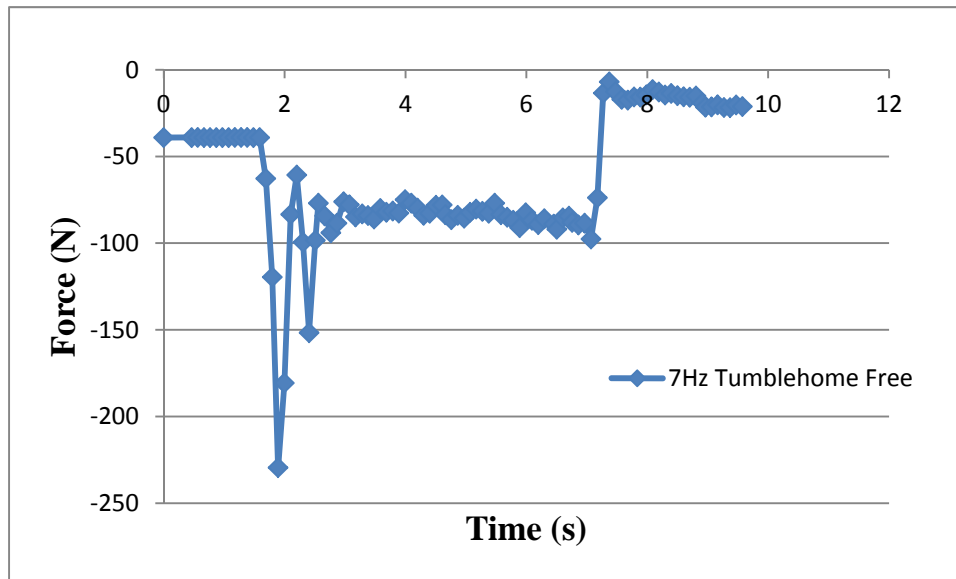


Figure 42. Raw Experimental Force Data.

This data shows the force is originally offset by 40 Newtons (N). The purpose of the base water trials was to measure the average force required to pull the plate through the water for different speeds and orientations. This was obtained by taking the average of the steady state section of the data defined in Figure 12. The corrected experimental data for the trial shown in Figure 42 is displayed in Figure 43. Smooth lines were used to make the data curves more visible.

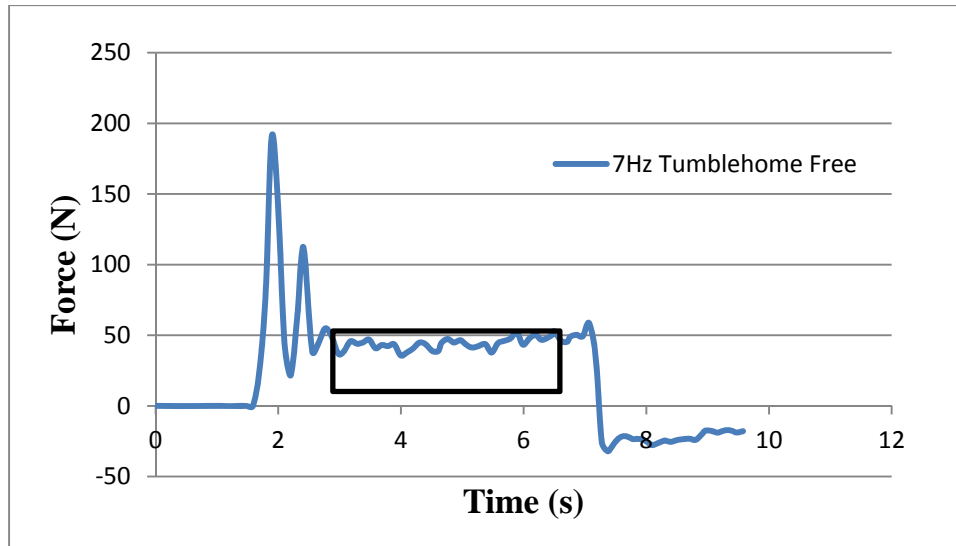


Figure 43. Corrected Experimental Force Data Used in Analysis with Steady State Region Isolated.

The strain data also had a permanent bias for each strain gauge that had to be accounted for. The same process used on the force data was used on the strain data. Typical corrected strain data is shown in Figure 44. Figure 45 shows the location of the strain gauges and the terminology used to describe the strain location being discussed.

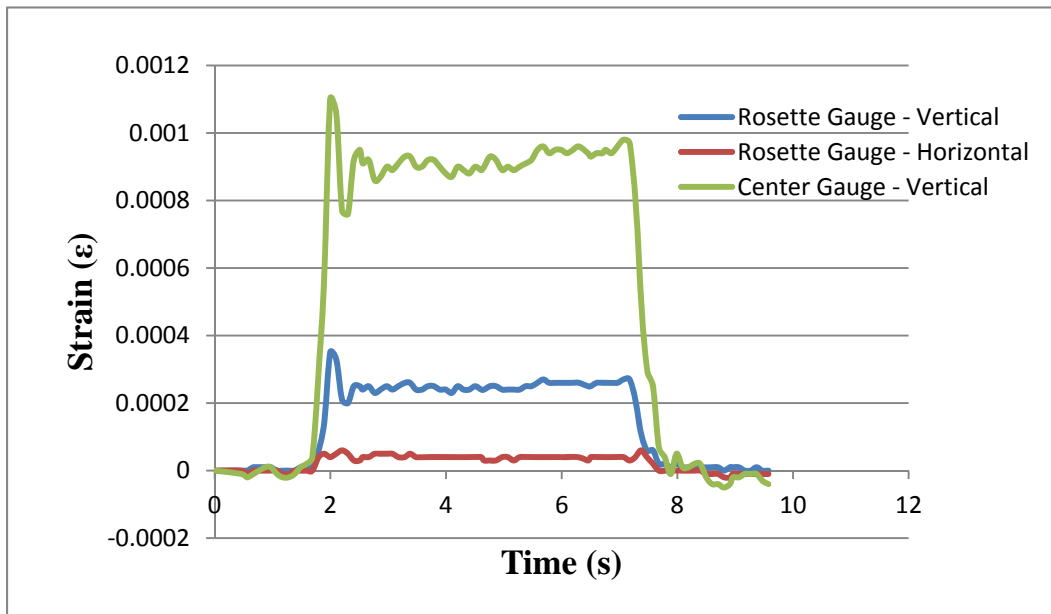


Figure 44. Corrected Experimental Strain Data Used in Analysis.

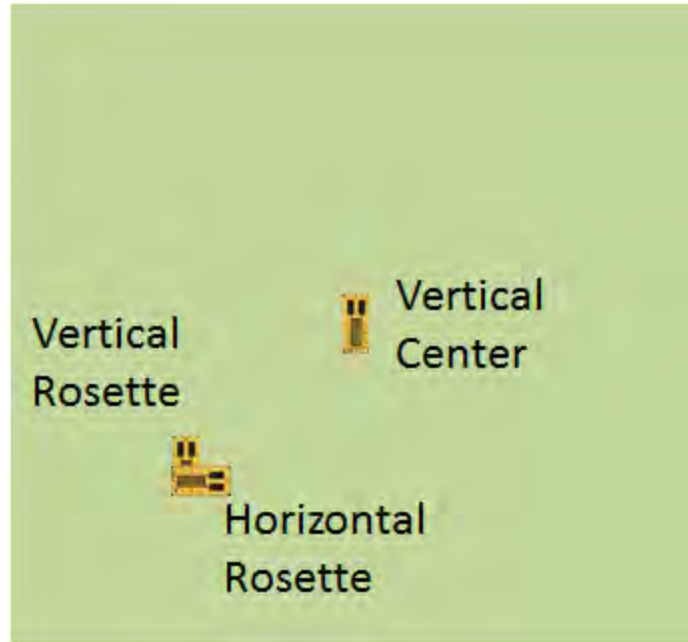


Figure 45. Strain Gauge Location and Terminology.

B. BASE WATER TRIALS

While not the focus of this study, the performance of the semi-submerged plates for the three orientations was investigated. These trials show that it required nearly half the amount of force to move the conventional plate through the tow tank than the force required to move the other two plates. The average force required to move each plate orientation is shown in Figure 46.

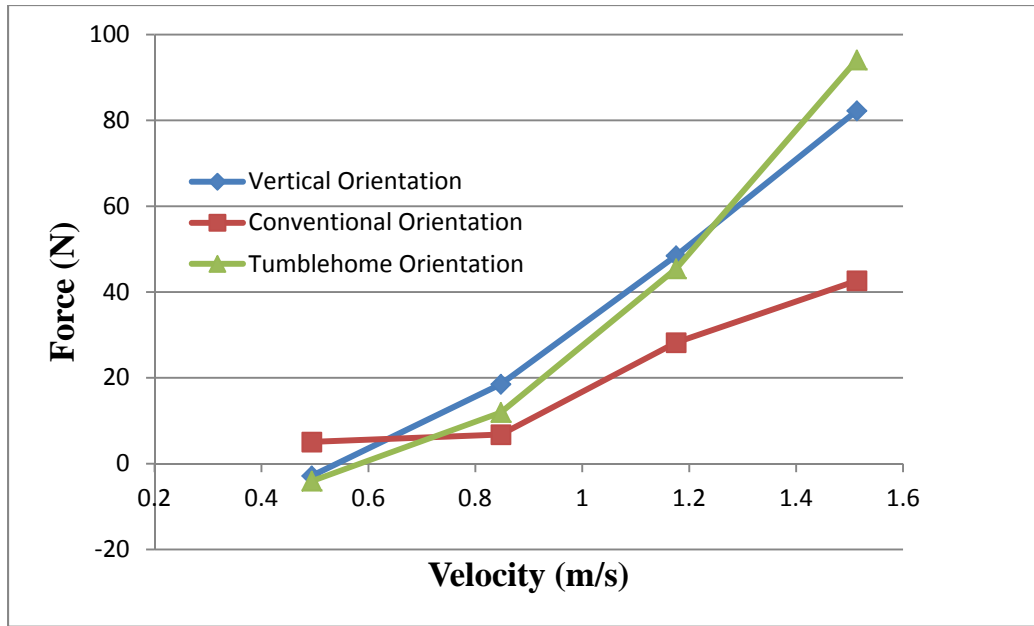


Figure 46. Average Force Required to Tow Different Plate Orientations for Base Water Trials.

The disparity in the towing forces most likely stems from the flow characteristics of the water around each plate orientation. When the tow tank was at rest, 12.7 cm (5 in) of the composite plate was above the waterline. The length of the plate above the waterline will be mentioned as the freeboard. The conventional oriented plate deflects the water down, whereas the tumblehome plate deflects the water up. This creates a large bow wave in front of the tumblehome hull. The water also rises higher on the tumblehome plate as it travels faster through the water resulting in little to no freeboard. As the plate velocity increased, the water partially topped the tumblehome oriented plate. This results in the tumblehome plate having to displace more water, increasing the force experienced by the load sensor attached to the pulley system. On the other hand, most of the five inches above the waterline remained dry as the conventional plate was towed through the water. The vertical plate exhibited the middle ground between the two extremes of the tumblehome and conventional flow profiles. The flow around the vertical plate is shown in Figure 47. This shows that the amount of freeboard was slightly reduced as the plate moved through the water. Figure 48 shows that water flowing over the tumblehome plate. Figure 49 shows the freeboard does not appreciably change for the

conventional plate. These images show the turbulent nature of the water flowing around the vertical and tumblehome oriented plates when compared to the flow around the conventional oriented plate.



Figure 47. Flow Around Vertical Plate at 9 Hz Exhibiting Partial Freeboard.



Figure 48. Flow Around Tumblehome Plate at 9 Hz Exhibiting Overflow.



Figure 49. Flow Around Conventional Plate at 9 Hz Exhibiting Full Freeboard.

The flow profile around each plate orientation is also responsible for the strain experienced by the composite plate. The tumblehome orientation resulted in the greatest strain experienced by the plate, while the conventional orientation resulted in the lowest strain experienced by the plate. As predicted by the Ansys model, the center strain gauge experienced the most strain. This is a result of its close proximity to the fixed support. The strain recorded by the vertical strain gauges is displayed in Figure 50.

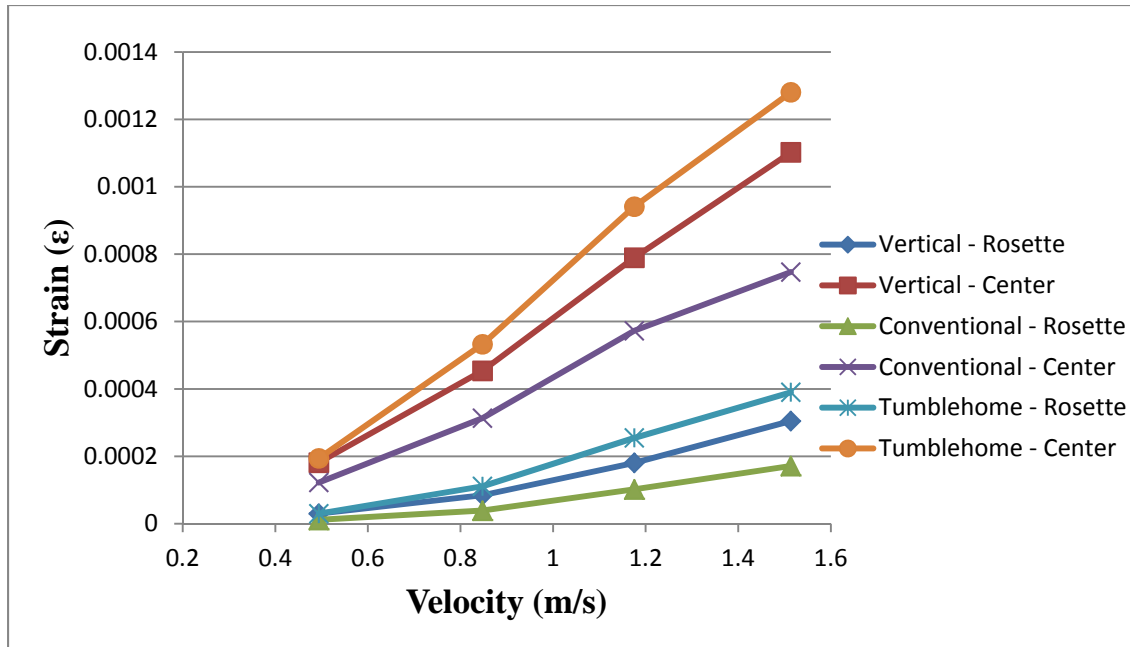


Figure 50. Average Strain Experienced by Vertical Strain Gauges during Base Water Trials.

The strain experienced by the horizontal strain gauge was more complex when compared to the vertical strain. It is logical for the strain experienced by the plate to increase as it travels faster through the water. This is exhibited by the vertical strain gauges. The horizontal strain values reveal a different strain profile. This is shown in Figure 51.

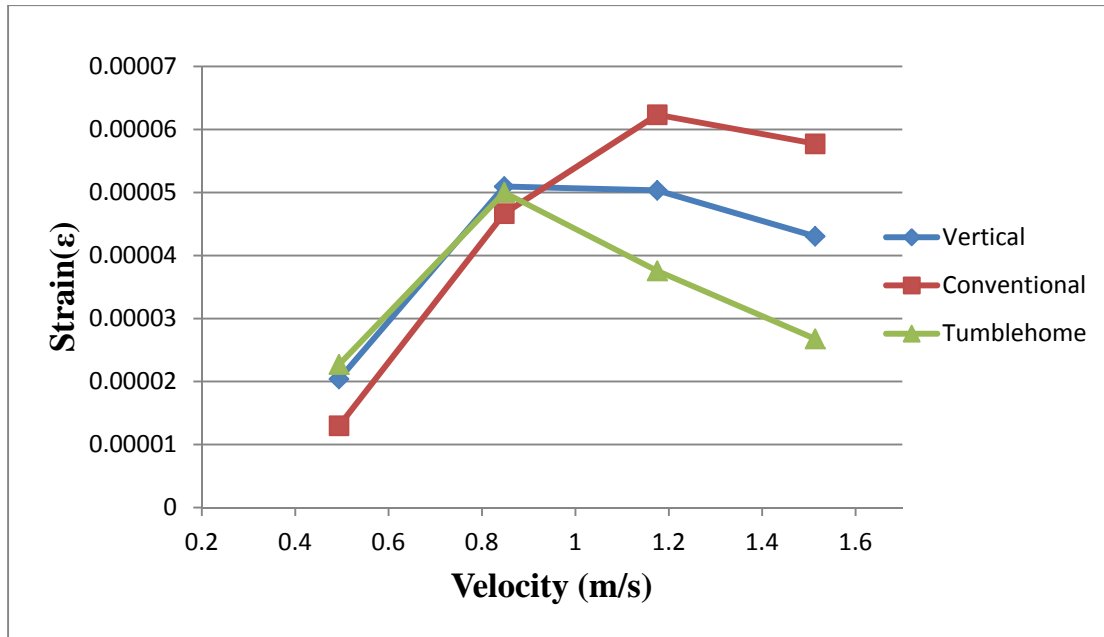


Figure 51. Average Strain Experienced by the Horizontal Strain Gauge for Base Water Trials.

This strain profile is believed to be the result of two different modes of deformation competing with each other. The two different modes of deformation are bending around the vertical centerline of the plate and bending around the horizontal centerline of the plate. To begin, it is important to notice that strain values in the horizontal direction are between one and two orders of magnitude less than the strain experienced in by the vertical strain gauges. This is a product of the location of the fixed support and the waterline. Since most of the pressure against the plate is below the fixed support, the plate primarily experiences bending around the horizontal centerline. Bending along both centerlines gradually increases until the strain reaches a critical point near 0.9 m/s. At this point, the deformation along the horizontal centerline becomes the dominant mode. As deformation increases in one mode, it decreases the amount of deformation for the other. Figure 50 shows that the vertical strain is greatest for the tumblehome orientation. This means the plate is bending more around the horizontal centerline. This explains why the strain decreases the most in the horizontal direction for the tumblehome orientation at high velocities. Conversely, the vertical strain for the conventional plate orientation has the lowest strain. Therefore the strain in the horizontal

direction has the potential to be the highest value amongst the three orientations. The two modes of deformation are shown in Figure 52. The trade-off in deformation was also apparent in the small ice density tests where strain in the horizontal and vertical direction was inversely proportional.

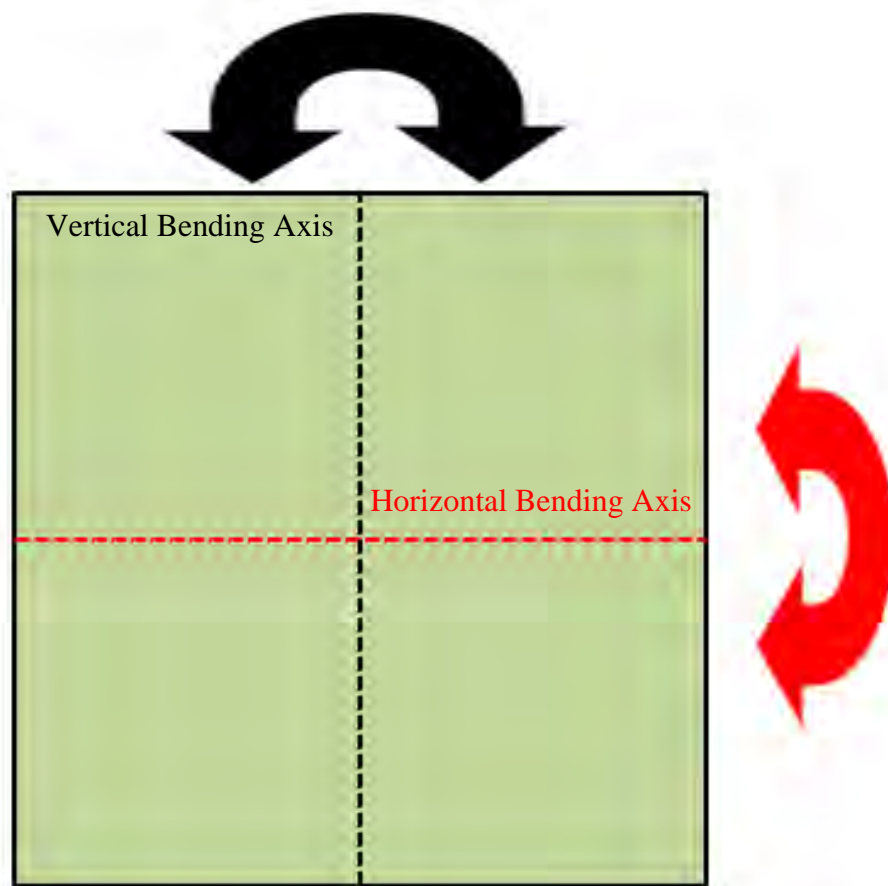


Figure 52. Competing Deformation Modes at High Velocities.

C. SMALL ICE DENSITY TRIALS

In order to assess how the presence of the two-inch diameter LDPE rods affected the strain experienced by the plate and the force required to pull the plate through the water, the collision event was isolated. The distance from the starting location of the carriage to the LDPE rods was measured. Using the velocities obtained from the high speed camera, the amount of time required for the composite plate to reach the section of

ice was calculated. This time was then overlaid on the experimental data for the strain and force graphs. If the LDPE had an effect on the strain or force, it should have been visible on the plotted graphs at, or immediately following the calculated time of impact. For example, using the carriage velocity from the 7 Hz speed trial, it would take the carriage three seconds to reach the ice section. A three second window was created in the strain data. This window started at the first large strain spike at two seconds which indicates that the carriage began moving. The window stops just after five seconds. The spike in strain values that immediately follow the time window results from the interaction between the LDPE rods and the composite plate. An example of this process is shown in Figure 53.

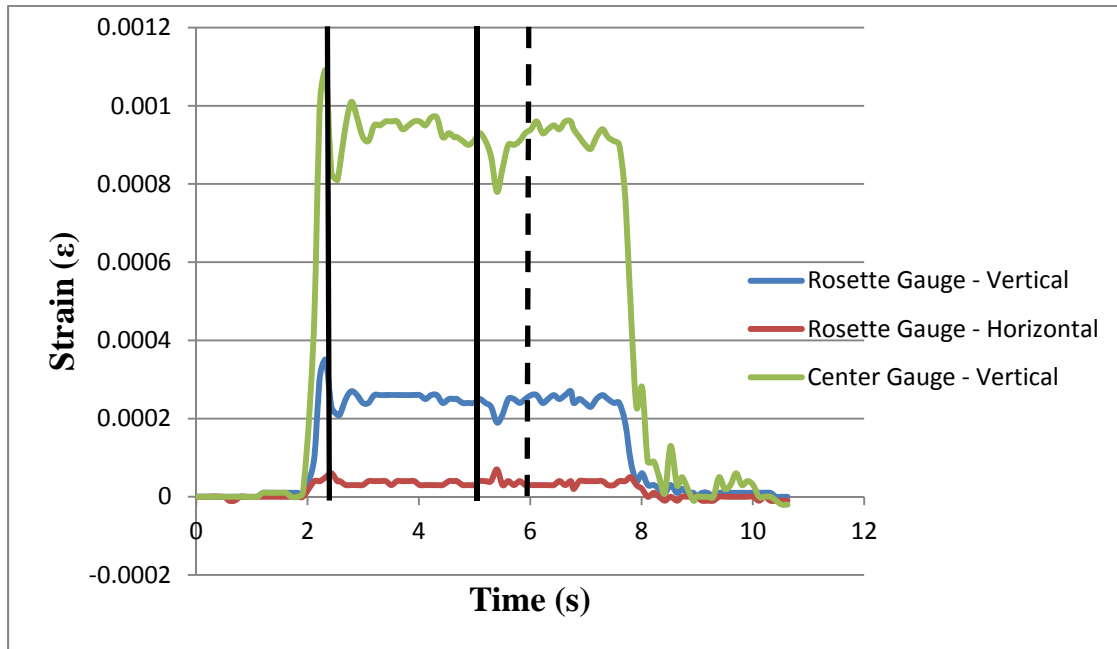


Figure 53. Use of Carriage Velocity and Distance to Ice Equivalent Section to Verify Impact Time.

The section immediately after this window was then isolated in order to obtain the difference between the peak strain from the steady state strain experienced prior to the impact. The isolated section of strain data lies between the last solid vertical line and the dashed vertical line in Figure 53. This is shown in Figure 54. The peaks are less defined

than in those in Figure 53 because the time scale has been expanded nearly tenfold. This process was also completed for the force values.

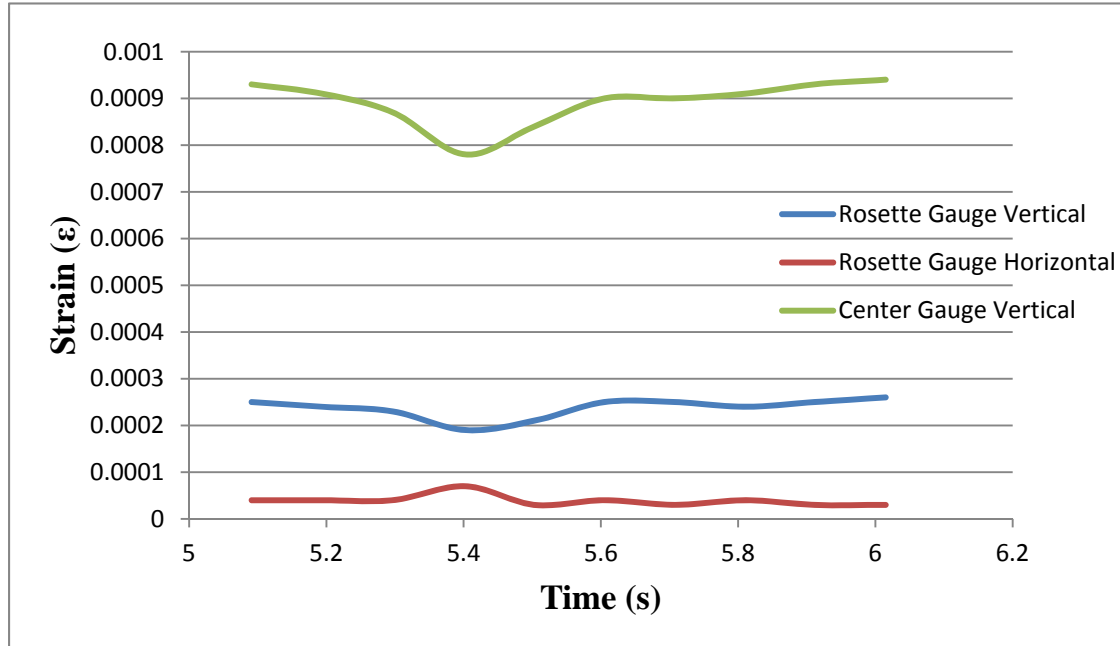


Figure 54. Isolated Impact Strain Data.

It was difficult to make comparisons between the performances of each hull orientation as they interact with the ice equivalent. The steady state strain and force values for each plate orientation are different. Since the values are different, the performance of each plate orientation was assessed by the percent increase or decrease between the steady state value (strain or force) prior to the ice impact and the peak value that resulted from the collision with the ice equivalent. Trials at 3 Hz were excluded from this analysis because the variation in the strain and force values was too inconsistent.

1. Peak Force Analysis

The analysis of the ice trials at 50% capacity yielded a common trend for the percent increase in the peak force required to tow the composite plate. The percent increase in force for the different plate orientations is shown in Figure 55.

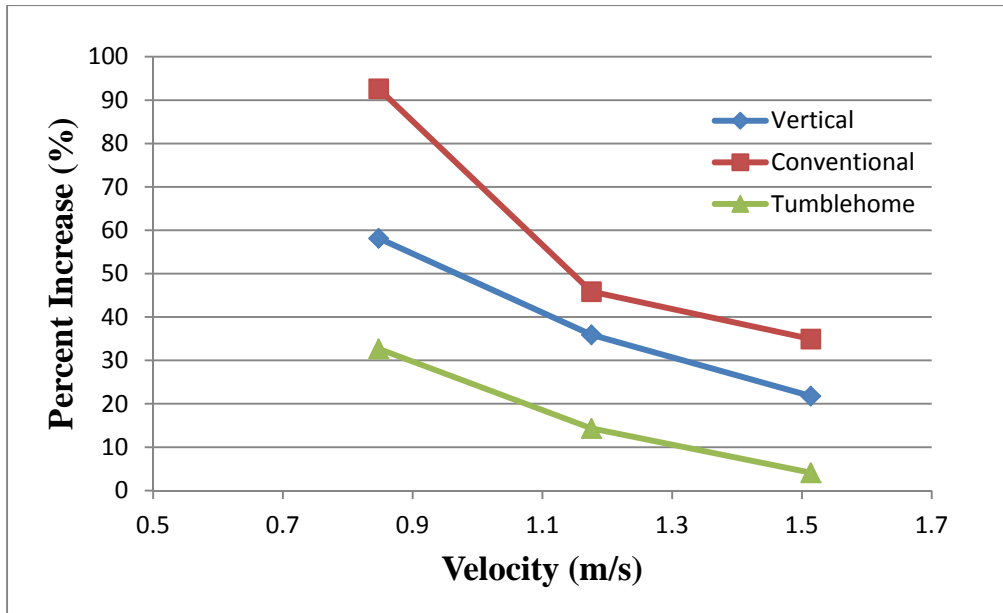


Figure 55. Peak Force Percent Increase for High Capacity Ice Trials.

As the velocity of the plate was increased, the percent increase in the peak force gradually decreased. This is due to the fact that the force required to move the carriage at high velocities is much higher than the force required to move the plate at low velocities. The force of drag on the plate is a function of velocity squared. While the percent increase in peak velocity diminishes, the increase in value is still notable. For instance, at a speed setting of 5 Hz (0.85 m/s), the average force required to pull the conventional oriented plate before it reached the ice section was 5.35 N. The 92% increase resulted in a peak force of 10.3 N, a rise of 4.95 N. On the other hand, at 9 Hz (1.51 m/s) the average force was 45 N. The 34% increase in force increased the value to 61 N, an increase of 16 N. That increase is more than three times that of the lower speed trial.

The data shows that the tumblehome orientation experienced the smallest increase in peak force values. This initial study shows that a tumblehome hull travels more efficiently through Arctic sea lanes congested with free-floating ice. The footage recorded by the high-speed camera supports the fact that the tumblehome orientation navigates better in the presence of ice. Still images of the footage were taken at three locations along the ice section in the tow tank. The first set of images shown in Figure 56 display the three plate orientations as they approach the ice section.

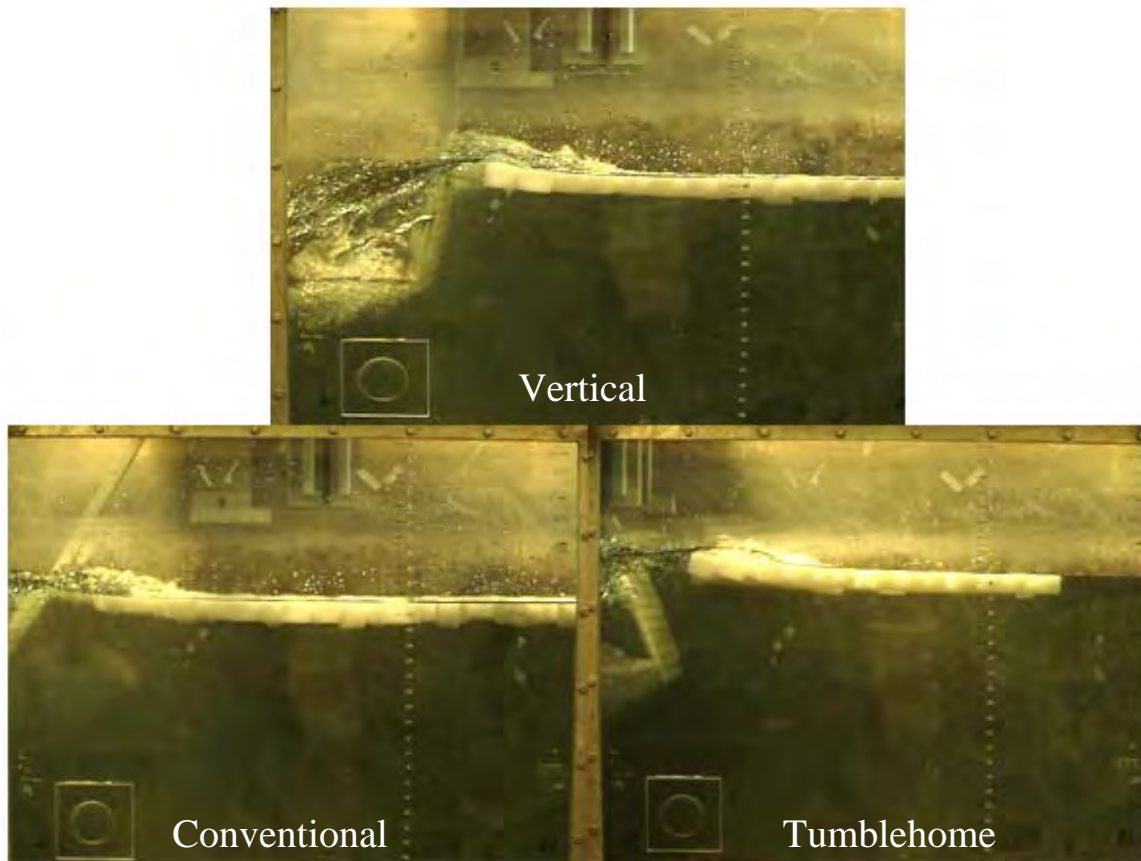


Figure 56. Profile View of the Small Ice Section as the Three Plate Orientations Approach the Ice Equivalent.

While the flow patterns around the plate were not drastically different to begin with, slight differences are noticeable. For instance, as the tumblehome-oriented plate approached the ice equivalent, the ice equivalent was pushed away from the plate. Not only was it pushed away in the lateral direction, but the rods began to rise in the bow wave generated by the plate. The bulbous bow of large navy ships most likely creates a bow wave similar to that of the tumblehome plate, which displaced the ice equivalent. However, small craft such as the *M-80 Stiletto* are not large enough to constitute the addition of a bulbous bow. The ice equivalent did not experience much displacement for the other two plate orientations. The next sets of images in Figure 57 were taken as the plate contacted the ice equivalent.

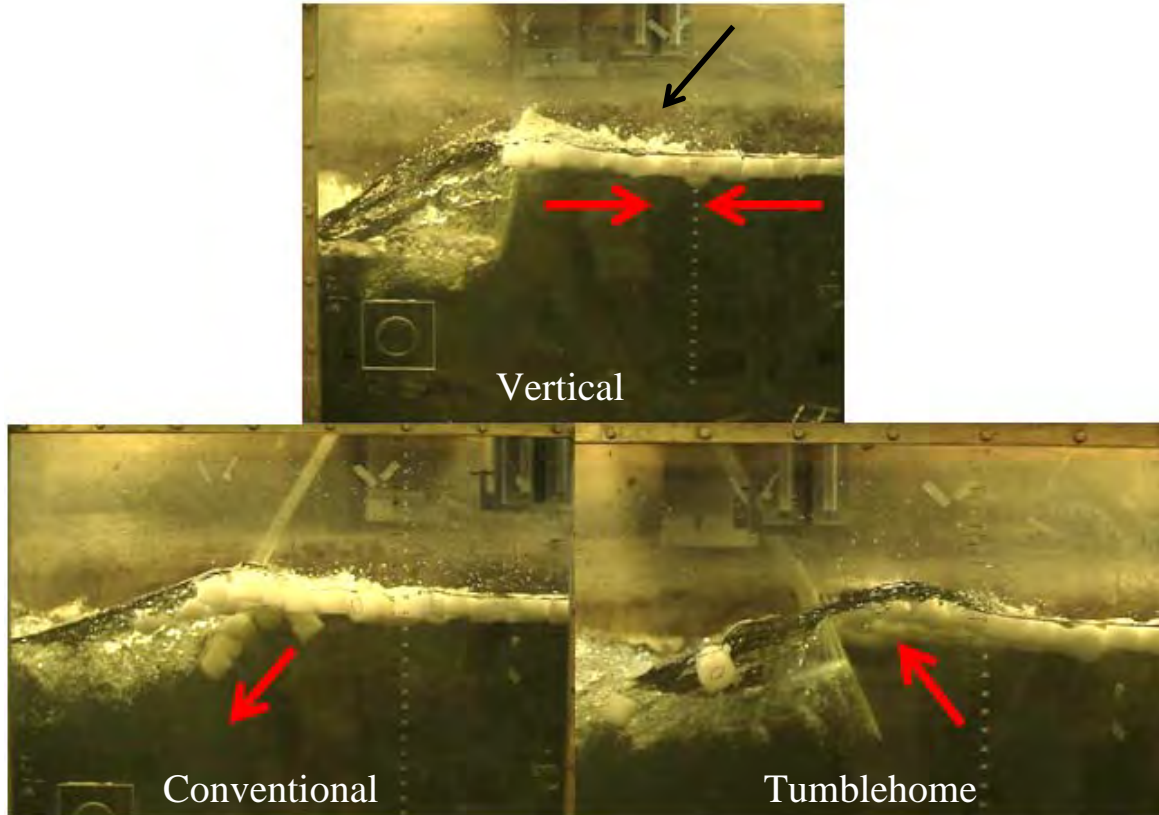


Figure 57. Profile View of the Small Ice Section as the Three Plate Orientations Contact the Ice Equivalent.

Each image has a red arrow which shows the direction in which the ice equivalent was deflected once it contacted the plate. The image of the vertically oriented plate shows perturbations in the water in front of the plate highlighted by the black arrow. This is the result of the individual ice equivalent segments impacting one another. Unlike the other two plate orientations, the vertical plate orientation does not deflect the ice equivalent up or down. This causes the ice equivalent in the front of the section to be driven into the ice equivalent behind it. The conventional-oriented plate deflected the ice equivalent deeper into the water and underneath the plate. This may be problematic for sea-going vessels as the ice may deteriorate the quality of the propellers over time, resulting in a decrease in performance and an increased noise signature. On the other hand, the tumblehome-oriented plate pushed the ice equivalent up. The difference between these two flow profiles demonstrates why the tumblehome oriented plate experienced a smaller percentage increase in peak force when compared to the conventional oriented plate.

Rather than colliding with the ice equivalent, the tumblehome orientation displaces the ice around the plate. The last set of images in Figure 58 show various plate orientations near the end of the ice section.

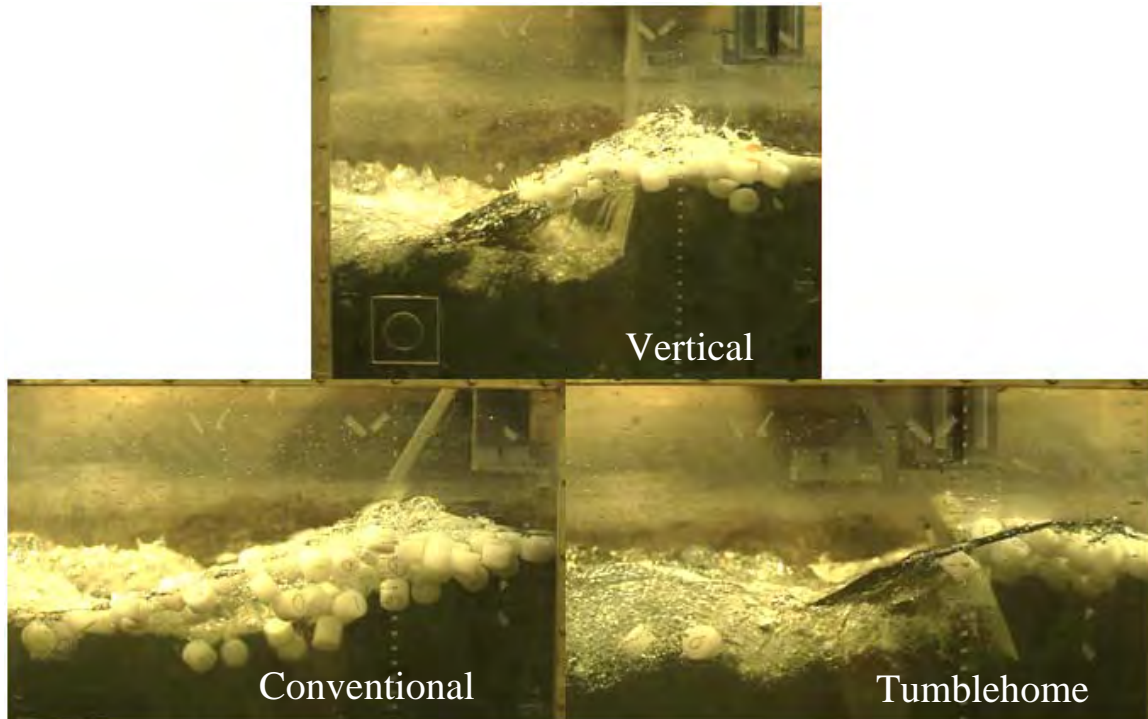


Figure 58. Profile View of the Small Ice Section as the Three Plate Orientations near the End of the Ice Section.

These images provide further evidence of the findings mentioned above. The image of the conventional orientation shows a large amount of ice equivalent being displaced deep into the water. On the contrary, there appears to be a large concentration of ice equivalent remaining in front of the tumblehome oriented plate. The ice equivalent also remains near the water level for the vertical plate. It appears that nearly half of the ice equivalent has flowed around the vertical plate. Two enlarged images that display the flow profile of the ice equivalent around the tumblehome-oriented plate are shown in Figure 59 and Figure 60. These better show the flow of the ice equivalent around the plate.

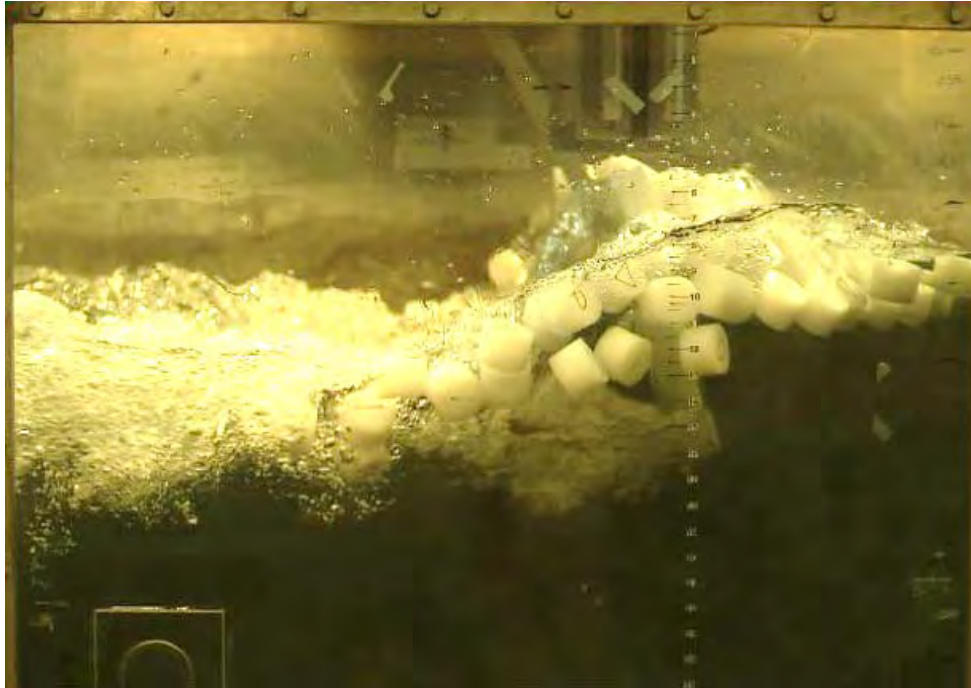


Figure 59. Enlarged Image of the Flow Profile for Tumblehome Plate in the Middle of the Ice Section at 9 Hz.

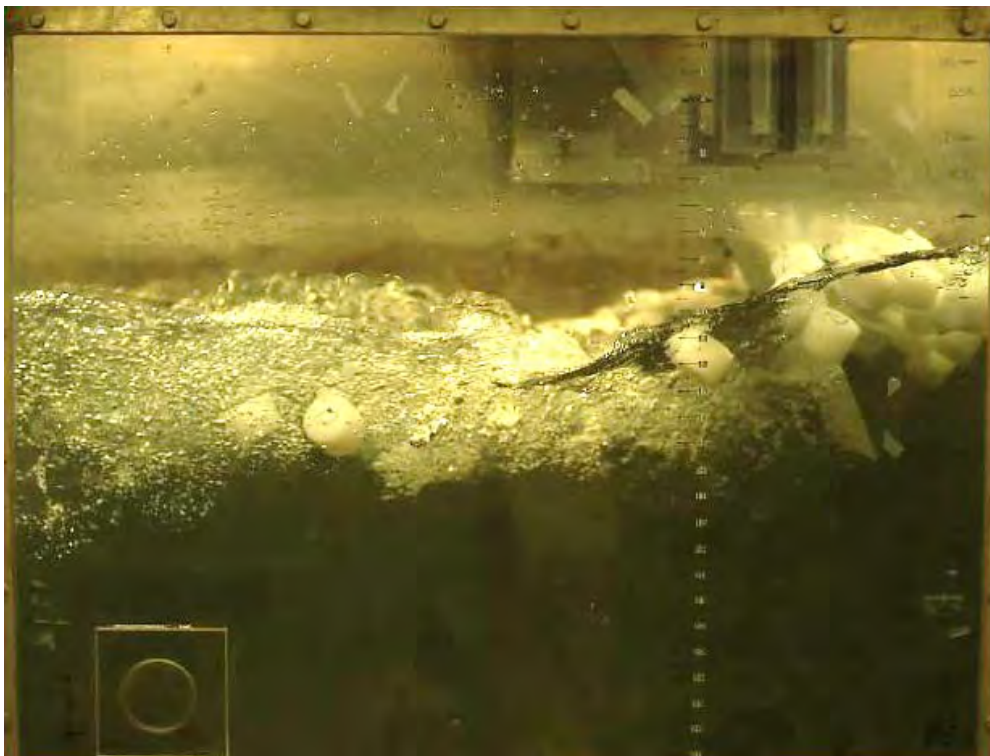


Figure 60. Enlarged Image of the Flow Profile for the Tumblehome Plate at the End of the Ice Section at 7 Hz.

2. Peak Strain Analysis

The composite plate experienced the same phenomena mentioned in the base water section where the bending around the horizontal and vertical axis was inversely related. The strain values recorded from each gauge was expected to increase when the plate collided with the ice section. Instead, the horizontal strain increased while the vertical strain values decreased. This behavior is attributed to the competing deformation modes explained in the base water trials section. The collision with the LDPE rods caused the plate to experience increased bending along the vertical centerline. This was because the ice equivalent was present at the waterline. When the bow wave was accounted for, the ice equivalent at the waterline added pressure against the plate near the top of the plate where the fixed support was present. This added pressure resulted in bending about the fixed support. The increased deformation around the vertical centerline decreased the amount of bending around the horizontal centerline. The peak strain in the horizontal direction always increased. The data is presented to allow for the comparison between the peak strain values experienced by the different plate orientations. Figure 61 shows the percent change in strain experienced by the vertical rosette strain gauge. The 220% increase in the plot was due to the low value of the average strain before the impact event. The strain recorded from the horizontal strain gauge increased from $50\ \mu\epsilon$ to $160\ \mu\epsilon$, while the vertical strain at the same location decreased from $160\ \mu\epsilon$ to $100\ \mu\epsilon$. The average strain was in the denominator for the percent change calculation.

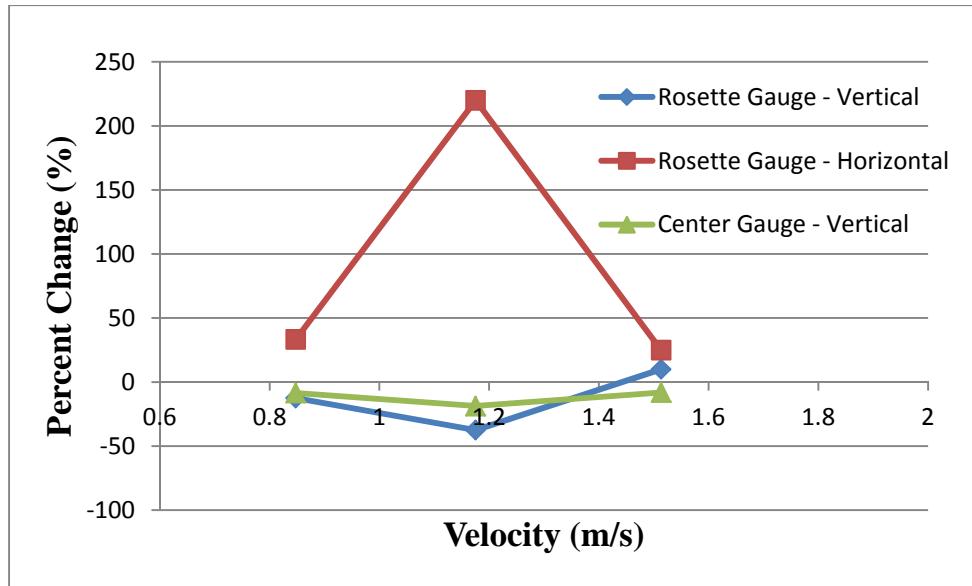


Figure 61. Percent Change in Strain for the Vertical Orientation during High-Capacity Small Ice Trials.

The 7 Hz (1.18 m/s) speed trial (center data point) for the vertical plate resulted in the largest percent change for all strain gauges. This trend is also present for the data obtained in the tumblehome trials. This is most likely due to the bow wave generated in front of the composite plate for the vertical and tumblehome plate orientations. The images of the different oriented plates as they approach the ice section shown in Figure 56 display this bow wave. The plate velocity affects the interaction between the plate and ice equivalent in two ways. First, the force resulting from impact is directly related to the speed at which the plate strikes the ice. Increasing impact velocities result in greater incident forces. The velocity of the plate also affects the size of the bow wave generated. Increasing plate velocity results in an increased bow wave. This bow wave aids in displacing the ice equivalent, lowering the initial impact between the plate and ice equivalent. There is a critical point for the plate velocity where, at some speed slightly higher than the 7 Hz speed setting, the diminishing effect on the incident force from the bow wave generated by the plate surmounts the amplification in force resulting from the impact at higher speeds. The percent change in strain for the tumblehome orientation is shown in Figure 62.

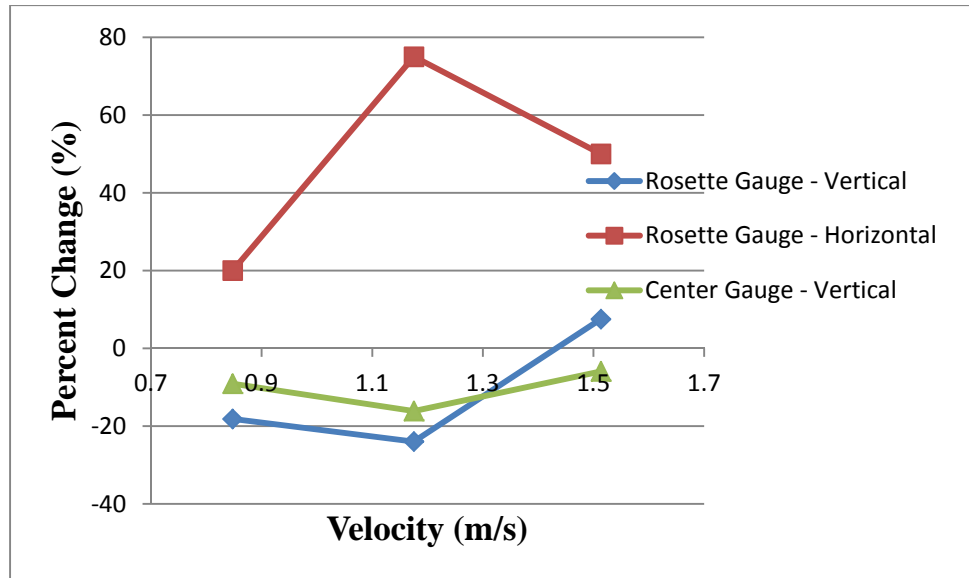


Figure 62. Percent Change in Strain for the Tumblehome Orientation during High-Capacity Small Ice Trials.

The dominant bow wave effect is apparent between the second and third data points for the three strain gauges. The strain experienced by the conventional oriented plate is unique. Since the bow wave generated is smaller, its diminishing effects appear at lower velocities. With the exception of one trial, the high-speed trial resulted in the greatest increase in strain. The percent increase in strain for the conventional oriented plate is displayed in Figure 63.

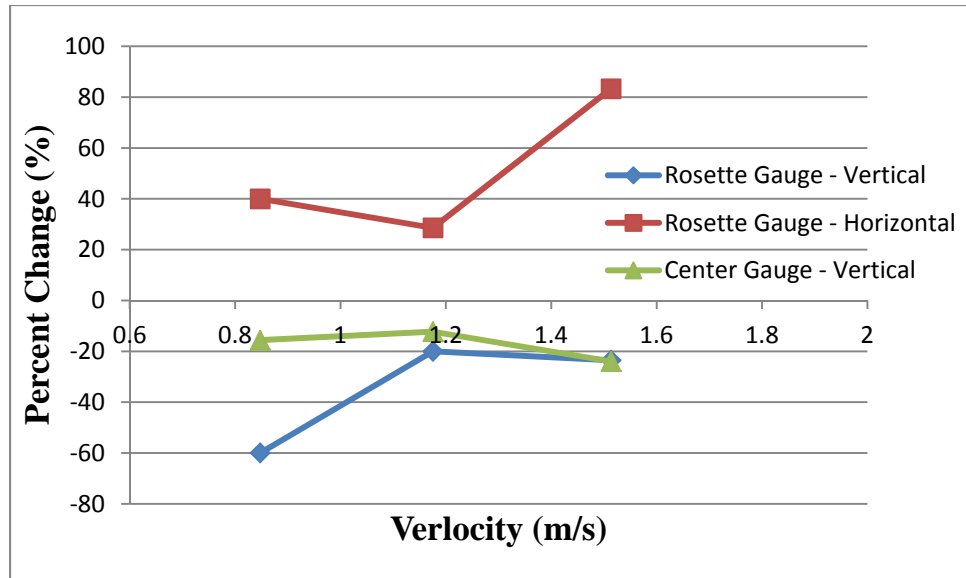


Figure 63. Percent Change in Strain for the Conventional Orientation during High Capacity Small Ice Trials.

Some trials displayed a dynamic response after the initial impact. The resulting strains values appeared to be random in nature and no trends could be determined. The dynamic response can be explored in a future experiment in which the section of ice extends for a larger percentage of the tow tank. In this experiment, the ice section was only 94 cm (37 in) long. If the post-impact dynamic response is desired, the ice section should extend at least three meters. A three meter ice section at 50% capacity would require 531 two-inch diameter LDPE rods. While this would complicate running multiple trials, it would be necessary to fully characterize the performance of each hull orientation in the Arctic environment.

3. Ice Capacity Effect

This experiment showed that ice capacity does not have a large effect on the initial peak in strain values produced from the impact of the plate and the ice section. All trials were completed at 7 Hz (1.18 m/s). The largest percent change in strain for all trials was 2.2%. The largest percent change for the center strain gauge was 0.16%. Once again, the percent change in strain for the vertical and tumblehome orientations have similar trends, while the conventional orientation has a unique data trend. An increasing ice

capacity yields greater percent change in strain for the vertical and tumblehome orientations. The percent change in strain for the varying plate orientations is shown in Figure 64, Figure 65, and Figure 66. Most values of percent change were negligible.

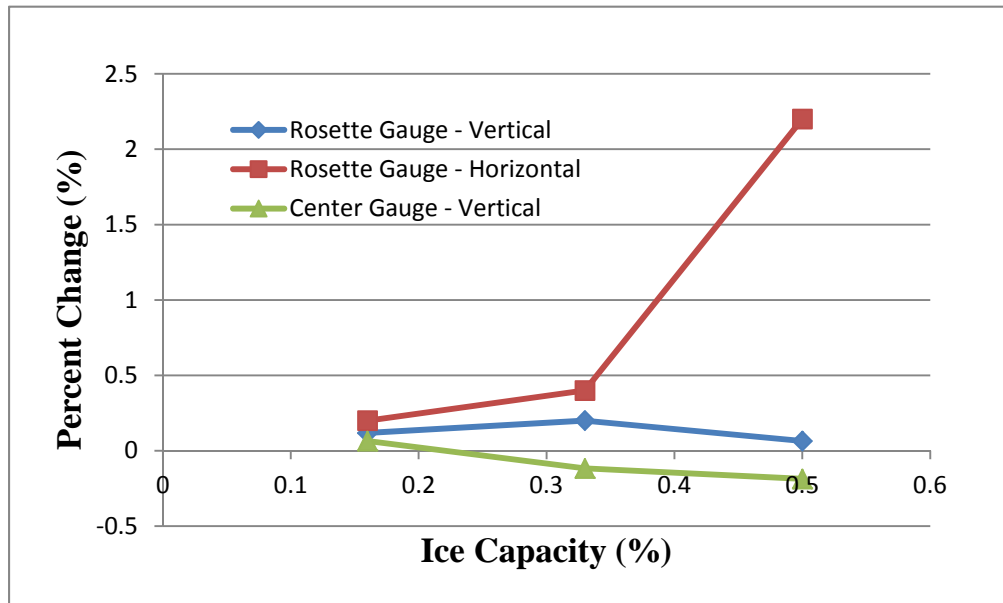


Figure 64. Percent Change in Strain for the Vertical Orientation at 7 Hz for Different Ice Capacities.

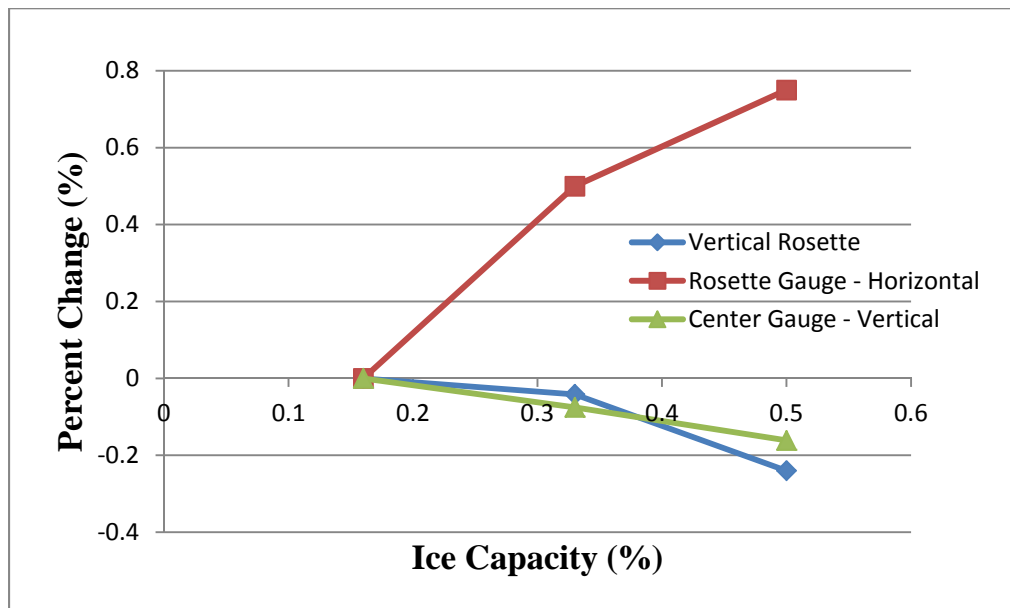


Figure 65. Percent Change in Strain for the Tumblehome Orientation at 7 Hz for Different Ice Capacities.

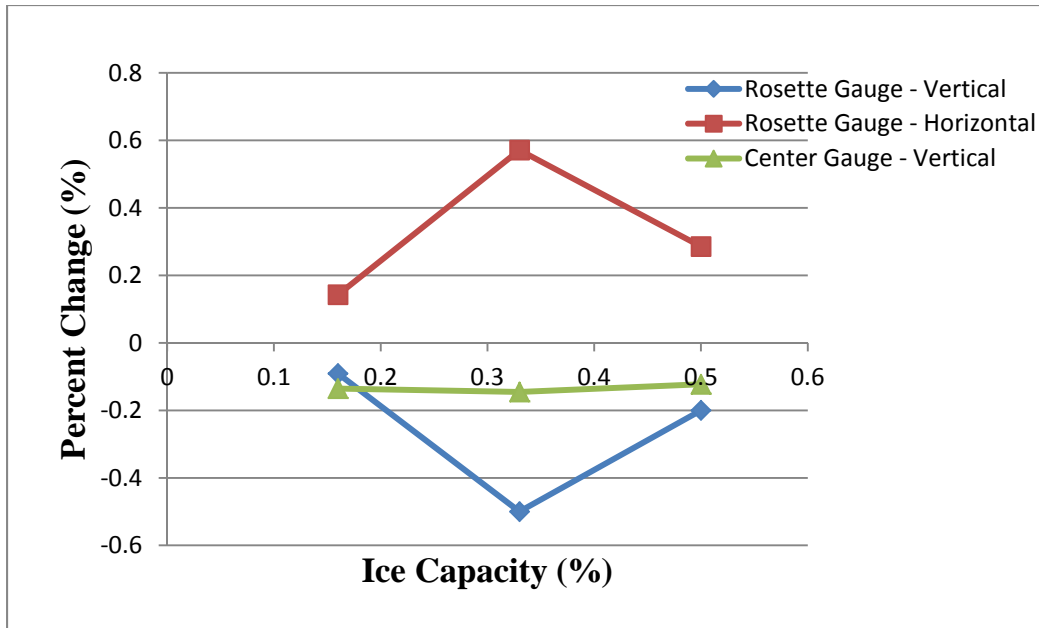


Figure 66. Percent Change in Strain for the Conventional Orientation at 7 Hz for Different Ice Capacities.

D. LARGE ICE TRIALS

After viewing the data obtained from both the single impact and double impact large ice trials it was determined that, with one exception, a single impact event with the large diameter ice equivalent could only be isolated for the 7 Hz (1.18 m/s) speed trials. The pulley system used to translate the carriage across the tow tank creates too much variation in the recorded values of force and strain. The impact event is concealed in the fluctuating force and strain values for low carriage speeds. This is shown in Figure 67. The vertical line indicates the time at which the impact should have occurred. The strain recorded by the center strain gauge was added to the plot. The strain values aid in visually identifying the moment of impact.

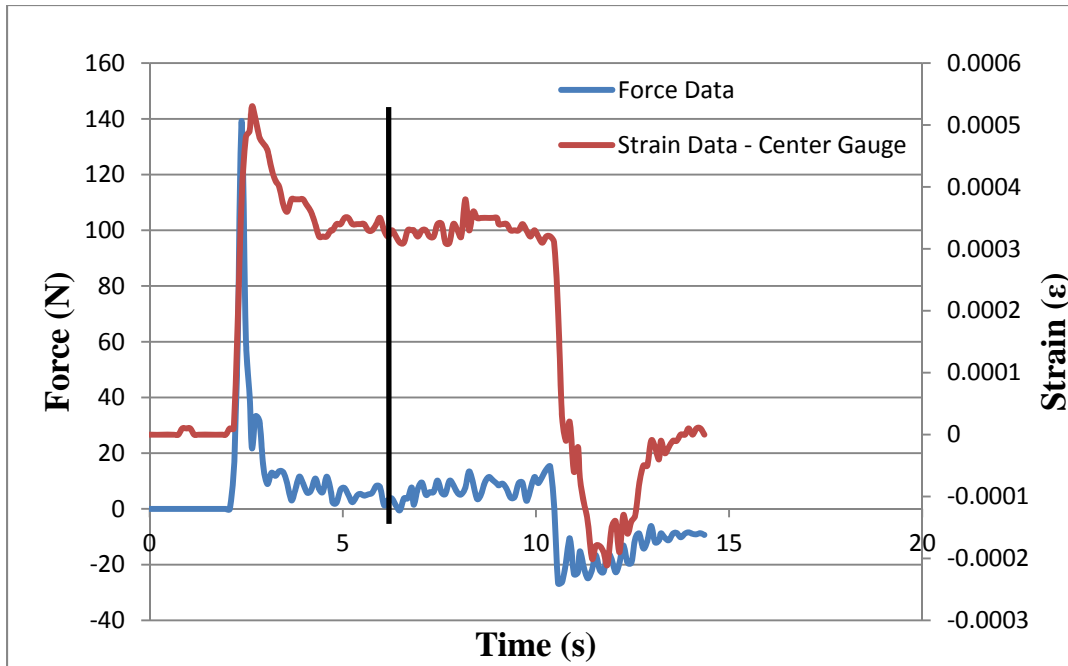


Figure 67. 5 Hz Conventional Trial with no Apparent Impact Point.

The fact that only the trials from the 7 Hz yielded noticeable results may not be by chance. As discussed for the small ice trials, 7 Hz was the critical speed at which the bow wave had yet to diminish the impact between the plate and ice equivalent. This also pertained to larger sized ice equivalent. The exception to this fact is the high speed conventional trial. This is due to the insignificant bow wave created by the conventional orientation. The difference between the data obtained from a 7 Hz trial and a 9 Hz trial is shown in Figure 68 and Figure 69, respectively. The spike in strain is most evident.

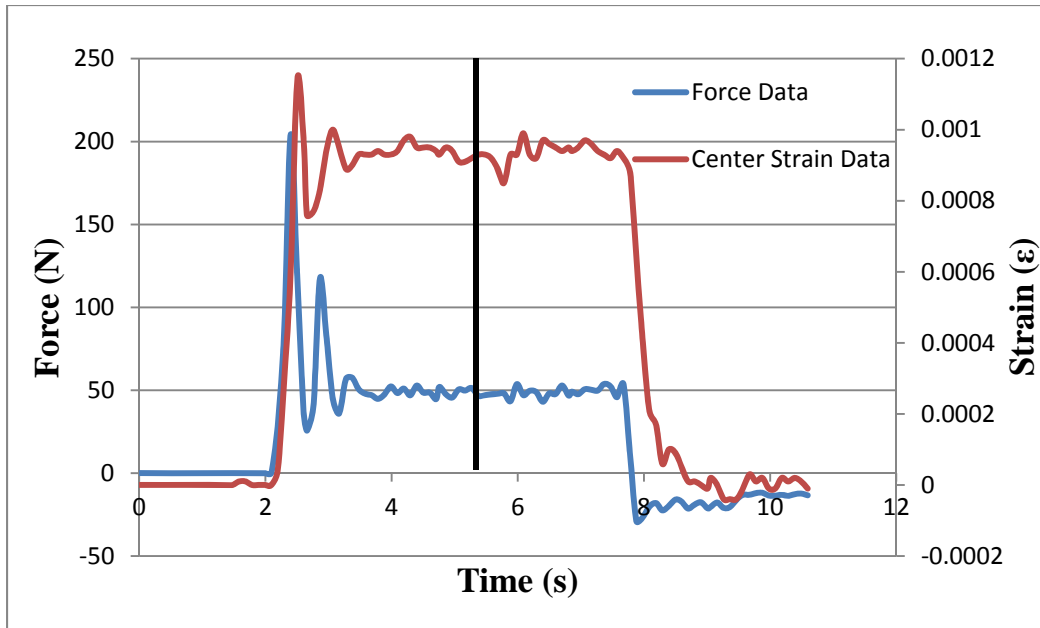


Figure 68. Strain and Force Resulting from Large Ice Double Impact at 7 Hz.

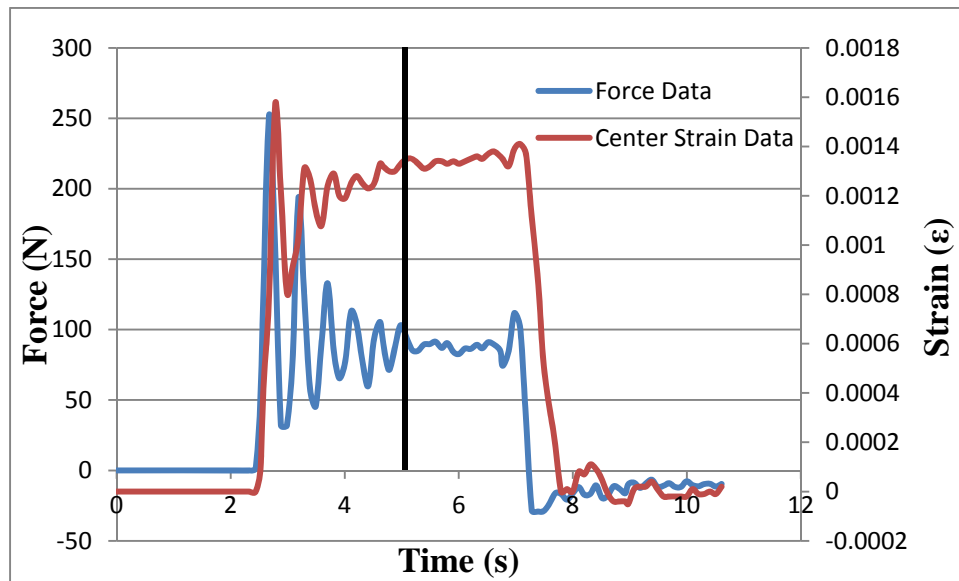


Figure 69. Strain and Force Resulting from Large Ice Double Impact at 9 Hz.

The percent change in stress and strain for the 7 Hz trials is tabulated in Table 6. The spike in force was greatest for the conventional orientation. The bow wave was not large enough to begin displacing the ice equivalent. This would have softened the impact between the plate and ice equivalent.

Table 6. Percent Change for Force and Strain Values at 1.18 m/s Due to Impact with Large Ice Equivalent.

Orientation	Force	Vertical Rosette	Horizontal Rosette	Vertical Center
Vertical	6.68%	-25.00%	140.00%	-11.84%
Conventional	42.70%	-41.67%	85.71%	-16.95%
Tumblehome	15.01%	16.00%	100.00%	-8.60%

The results in Table 6 are best explained by inspecting the still images taken during the large ice trials. These images show that the relationship between the different plate orientations and the resulting behavior of the ice equivalent are similar to those of the small ice trials. The only difference between the two is that the larger rods have more inertia. This increase in inertia lessens the pushing effect of the bow wave preceding the plate. The images are presented just as they were presented in the small ice section. The first set of images in Figure 70 shows the composite plate as it first approaches the large ice equivalent. The plate in the tumblehome orientation displaces the ice equivalent upwards and away from the plate. Conversely, the ice equivalent experiences little to no displacement for the conventional plate orientation. The next set of images in Figure 71 show the profile view immediately following the impact between the plate and the ice equivalent. The conventional oriented plate deflects the ice equivalent deeper into the water, whereas the ice equivalent moves with the tumblehome oriented plate. The ice equivalent also remains in front of the vertical oriented plate. The final set of images in Figure 72 show the continuation of each process. The ice equivalent continued to travel in front of the plate for the vertical and tumblehome oriented plates. The interaction between the ice equivalent and the plate in these orientations is prolonged. This results in a low force impact for a long length of time. On the other hand, the conventional orientation results in a nearly instant, high force impact.

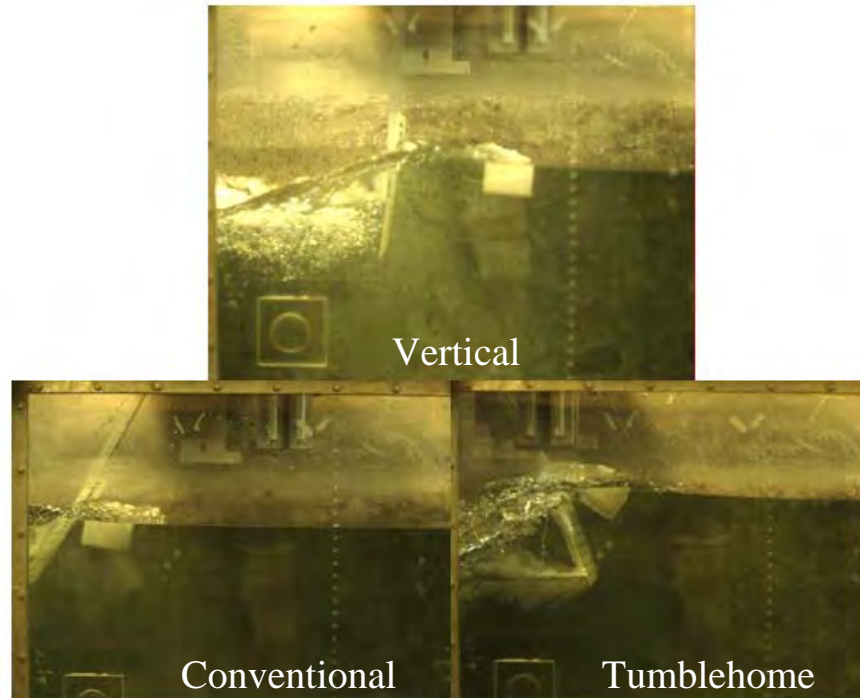


Figure 70. Profile View of each Plate Orientation on Approach to the Large Ice Equivalent.

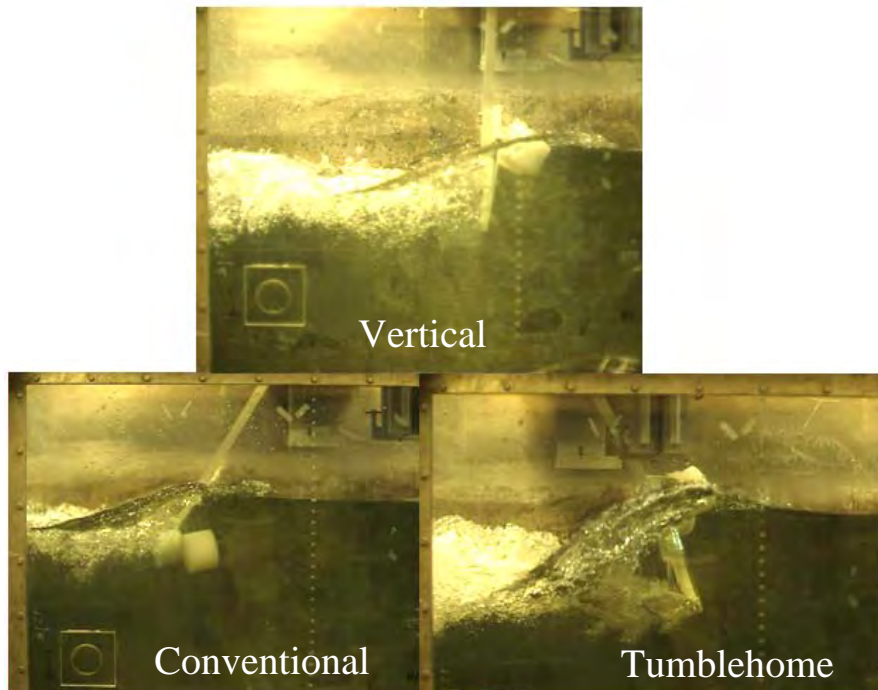


Figure 71. Profile View of each Plate Orientation on Contact with the Large Ice Equivalent.

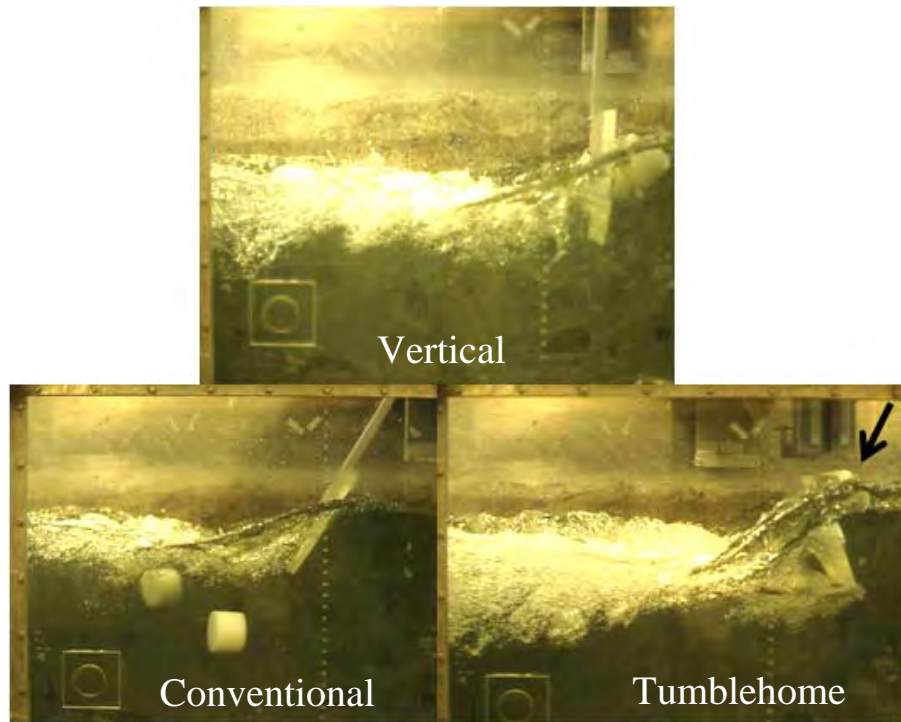


Figure 72. Profile View of Each Plate Orientation After Contact with the Large Ice Equivalent.

E. FRAMED COMPOSITE PLATE

For the plate fixed to the attachment bar, there was a notable difference between the strain at the center of the plate and at the offset location. This difference was not as evident when the frame was used to attach the plate to the attachment bar. The average strain in the vertical direction is shown in Figure 73. The maximum value in strain was still located at the center of the plate. The data from the center strain gauge is designated by the dashed lines.

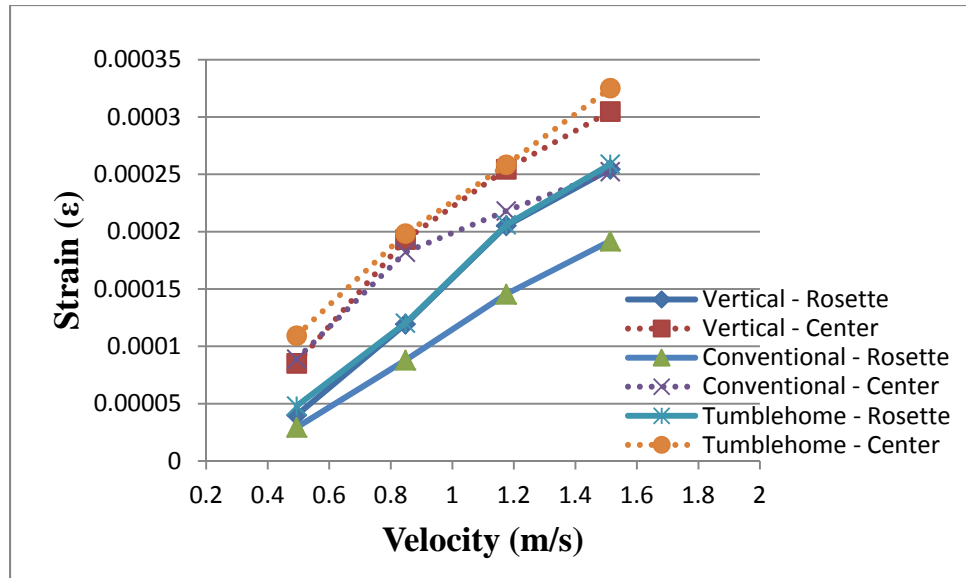


Figure 73. Average Strain Experienced by the Framed Plate during Base Water Trials.

As predicted, the change from the fixed support of the attachment bar to the fixed boundary conditions from attaching a frame to the composite plate greatly reduced the strain experienced by the plate. The strain values ranged from 13 $\mu\epsilon$ to 1280 $\mu\epsilon$ for the plate attached to the attachment bar. The framed boundary condition resulted in this range to be decreased to 14 $\mu\epsilon$ to 325 $\mu\epsilon$. The same pattern occurred for the horizontal strain gauge.

The interaction between the ice equivalent and the framed plate was visible in the strain data. For the most part, there was a response in the strain gauges at the time of impact. However, it would not make sense to compare the percent increase or decrease in strain to the frameless plate. Since the strain values are very small, a small change in strain would appear to have a large impact on the percent change in strain. For example, for the framed plate at 7 Hz, a change of 10 $\mu\epsilon$ would result in a 10% change in strain value. If the strain of the frameless plate was changed by 10 $\mu\epsilon$, the resulting percent difference would only be 2.4%. The difference in the location of the fixed support results in the two plates having different modes of deformation. For this reason, it makes little sense to compare the two.

F. SUMMARY OF EXPERIMENTAL RESULTS

The results of this experiment were highly dependent on the location of the waterline of the towed composite plate in relation to the location of the fixed support pulling the plate through the tank. The composite plate was originally given 12.7 cm (five inches) of freeboard in hopes that the water would not flow over the top of the plate for high speed trials. With the exception of the 9 Hz (1.51 m/s) tumblehome trials, the water did not flow over the plate. The location of the waterline was important because the goal of this thesis was to evaluate the performance of different hull orientations as they travel through ice-congested waterways. The interaction between the plate and the ice occurs at the surface of the water. Figure 74 shows the spatial orientation of the fixed support of the plate and the pressure generated by the impact between the plate and ice equivalent. The yellow area signifies the ice equivalent along the waterline.

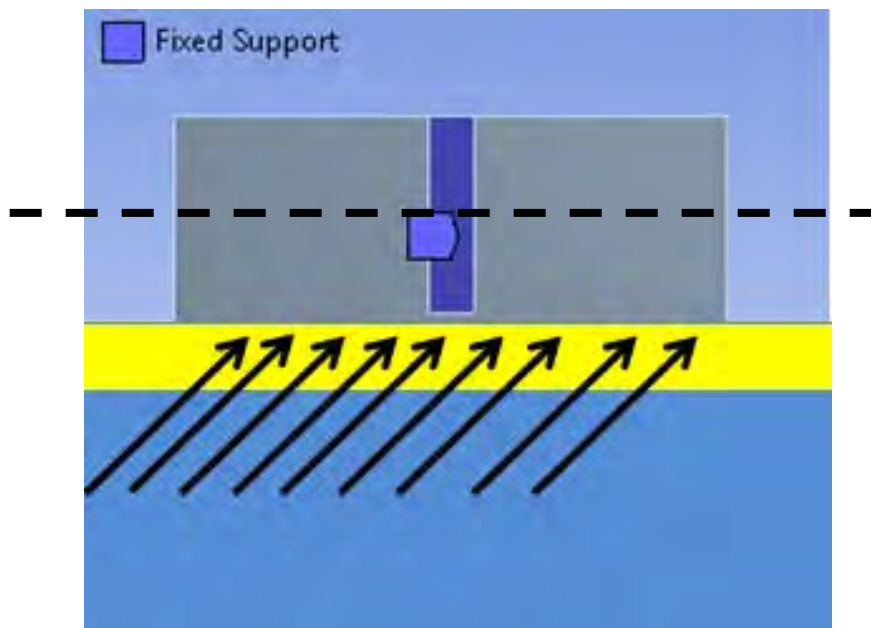


Figure 74. Incident Pressure Resulting from the Plate Travelling through the Ice Equivalent.

The resulting force of the ice equivalent against the plate will incur bending about the vertical centerline. After observing the tow tank trials, it was apparent that the bow wave increased the height of the location of the ice equivalent as it impacted the plate. A

more realistic impact plane is designated by the black dashed line. The competing deformation modes of the plate were discussed heavily in the results section. Any deformation in the horizontal direction resulted in decreased deformation in the vertical direction and vice versa. This was first evident in the base water trials where increased vertical deformation decreased the amount of deformation recorded by the horizontal strain gauges. The same phenomena occurred during ice density trials. The presence of the ice equivalent resulted in increased bending about the vertical centerline, reducing the strain recorded by the vertical strain gauges. The results of this experiment would have been very different had the fixed support been placed higher on the plate. This is portrayed in Figure 75.

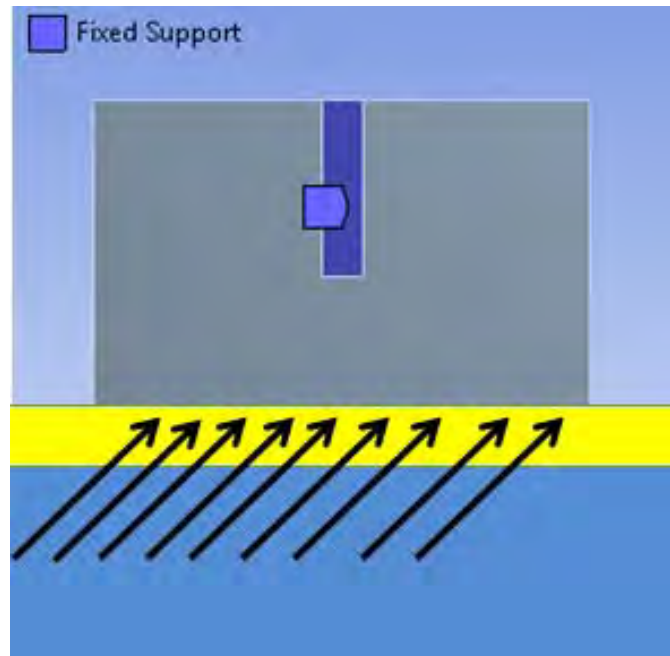


Figure 75. Incident Pressure against the Plate for the Case where the Water Line is Lowered.

If this was the case, the plate would experience little to no strain in the horizontal direction. The impact force of the ice equivalent would further increase the strain in the vertical direction. All of this proves the dependability of the strain experienced by the plate on the physical location of the waterline on the plate and the location of the fixed support.

The strain data is unique to this experiment. For this reason, the most valuable information obtained during this experiment was the effect of the ice on the force required to tow the composite plate and the footage obtained that show the interaction between each plate orientation and the ice equivalent. Both of these showed that the conventional plate orientation performed the worst in the presence of ice. The still images of the footage revealed a lack of bow wave generated by this orientation. This resulted in an immediate and violent impact between the plate and the ice equivalent. The tumblehome oriented plate experienced the lowest percent increase in peak force incurred by the impact. The video demonstrated that the ice equivalent was displaced up and around the plate due to the bow wave, resulting in little to no impact. This bow wave may still be present for large navy ships with conventional hulls due to their bulbous bow. However, small craft operating in Arctic sea lanes are not large enough for bulbous bows and will experience flow patterns similar to this experiment. Furthermore the footage of the conventional oriented plate revealed that after the impact, the ice equivalent is forced underneath the plate, pushing it deep into the water. This could result in the ice being ingested by the propellers. If this occurs for a prolonged amount of time, the propellers could experience a decrease in performance and an increase in the noise signature of the vessel. One potential problem with the flow profile of the ice around the tumblehome oriented plate is the accumulation of ice in front of the plate. This build up was apparent for the small ice equivalent section used in this experiment. This is shown in Figure 76. It is possible that if enough ice is accumulated in front of the plate it could impede the motion of the plate. If the accumulation was severe, the ice would grind against the composite. This grinding motion could result in the failure of the fibers of the composite.



Figure 76. Ice Accumulation Present Preceding the Tumblehome-Oriented Plate.

Another outcome of this experiment was the validation of LDPE as an ice equivalent. Throughout testing, the plastic maintained the same density and did not absorb any water. It allowed for repeatable experimentation and was simple to maintain and use. This method forgoes the extensive energy requirement of ice tanks that maintain the working area at freezing temperatures.

1. Recommendations for Future Work

If further information is sought regarding the flow of ice around moving structures, this methodology is recommended. Special consideration should be taken while considering the boundary conditions of the structure being towed through the tow tank. Testing on a prototype composite hull would be ideal. If another plate is used, a thin frame boundary condition would provide the most insight since most hulls are constructed of plates connected to the framework of the ship. A new frame should be

constructed, as the frame used in this experiment was too bulky and reduced the area of the plate exposed to the water.

Future experimentation should be conducted to better characterize the dynamic response of the plate after the initial impact with the ice section. To accomplish this, the ice section must be extended much farther than the one in this experiment. A three-meter ice section should allow for a full analysis of the response following the initial impact. A prolonged ice section would also answer the question of whether or not the ice accumulation effect exhibited by the tumblehome orientation would negatively influence its performance. It may also lead to further insight into the performance of the other plate orientations. This testing should be conducted with both small and large diameter LDPE rods. This experiment showed that the inertia of the ice equivalent has an effect on the interaction between the ice equivalent and the plate. If a longer ice section is used, an efficient method used to collect the ice equivalent would be necessary. The experiment can also be repeated using higher ice capacity values to simulate more congested sea lanes.

THIS PAGE INTENTIONALLY LEFT BLANK

IV. CFX MODEL

A CFX model of the experiment was created in an attempt to replicate the experimental data. Ideally, the CFX model would have been coupled to a structural model. This would allow for the pressure against the test plate calculated by the CFX model to be imported into a structural analysis tree. In order to do this there must be nodal connectivity between the fluid and the structure. This means the mesh of the fluid domain must be the same as the mesh of the structural analysis. This analysis has been completed for a fully submersed structure [26]. This CFX analysis was more complicated as it involved a semi-submerged plate. This CFX simulation required a mesh refinement in order to accurately model the free surface effect along the air-water interface. Without the mesh refinement, the boundary between the air and water would become indistinct. In order to assess the performance of each orientation, the incident fluid pressure on the plate was determined. All CFX results were steady state solutions. In the end, the presence of ice could not properly be modelled in the CFX analysis. The model presented does accurately show the free surface effect of the two-fluid domain around the plate for the conventional and tumblehome orientations. Ansys tutorials [27] were used as the basis for creating the two-fluid domain. This analysis was done for the conventional and tumblehome hull types.

A. CONTROL VOLUME

The control volume used for the CFX simulation was created in Solidworks. The control volume had the same width and height of the tow tank, but was shortened in order to keep the amount of mesh elements relatively low. Even with the reduction of the meshing elements, each CFX run required around 13 hours to meet the solver control requirements defined later. After trial and error it was determined that the control volume would extend 1.52 m (five feet) upstream of the plate and 3.048 m (10 feet) downstream of the plate for the angled orientations. This volume allowed for ample space to visualize the flow characteristics around the plate. The control volume for the vertical plate was 3 m (9.84 feet) long.

The test plate was created by creating a void inside of a rectangular prism (the tow tank volume). The first step in creating the control volume was to create a rectangle with the dimensions of the tow tank. The plate orientation was then established by creating a plane at the desired plate location. The plate orientation is shown in Figure 93 located in Appendix C, which contains all of the supplemental information regarding the Solidworks and CFX processes. The plate was then drawn and extruded from this plane. The “Merge Results” box was checked when extruding the attachment bar from the plate. The attachment bar was extruded a distance that allowed it to protrude from the rectangular prism of the tow tank once the rectangle was extruded. The rectangle was then extruded 4.572 m to achieve the necessary control volume in front and behind the test plate. Finally, the plate and attachment bar were removed from the control volume by selecting “Insert” from the drop down menu and selecting “Features...”, “Combine.” The subtract feature was selected and the plate was removed from the control volume. This is shown in Figure 93 of Appendix C as well. The control volume was then imported into CFX. This process was completed for the three different hull orientations used in the experiment. The control volume for the tumblehome oriented plate is shown in Figure 77.

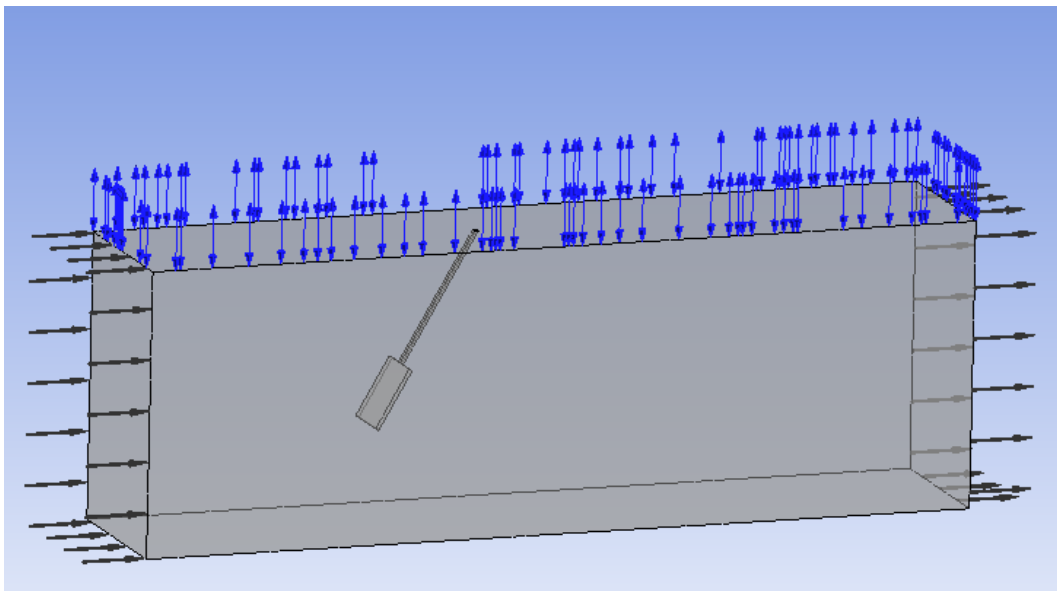


Figure 77. Control Volume with Location of the Inlet, Outlet and Opening Displayed.

The three control volumes were then meshed using the sizing parameters shown in Figure 78. The resulting mesh parameters of each control volume are shown in Table 7. An image of the mesh used can be found in Figure 94 of Appendix C. Tetrahedron mesh elements were used.

Sizing	
Use Advanced Size Function	On: Curvature
Relevance Center	Coarse
Initial Size Seed	Active Assembly
Smoothing	Medium
Transition	Slow
Span Angle Center	Fine
<input type="checkbox"/> Curvature Normal Angle	3.0 °
<input type="checkbox"/> Min Size	2.5e-002 m
<input type="checkbox"/> Max Face Size	2.5e-002 m
<input type="checkbox"/> Max Size	2.5e-002 m
<input type="checkbox"/> Growth Rate	Default (1.20)
Minimum Edge Length	2.e-002 m
Inflation	
Use Automatic Inflation	None
Inflation Option	Smooth Transition
<input type="checkbox"/> Transition Ratio	0.77
<input type="checkbox"/> Maximum Layers	5
<input type="checkbox"/> Growth Rate	1.2
Inflation Algorithm	Pre
View Advanced Options	No

Figure 78. Mesh Sizing Used for CFX Control Volume.

Table 7. Mesh Parameters of Control Volumes.

Plate Orientation	Vertical	Conventional	Tumblehome
Nodes	237,599	611,014	610,977
Elements	1,361,902	3,535,883	3,535,750

1. Fluid Parameters and Boundary Conditions

Next, the boundary conditions of the fluid domain were defined. First, variables were created that were used to define fluid properties such as water height, densities, pressures, and volume fractions between the air and water. The full list of expressions created and their values is shown in Figure 95 in Appendix C. The water heights were fine-tuned in order to achieve the proper water level against the plate identical to that of the experiment. All fluid velocities were set to one m/s.

The two-fluid domain was created under the default domain tree, which highlights the entire control volume. Both air (at 25°C) and water were defined. Buoyancy was accounted for in the model in order for the air and water to separate into two distinct bodies. The Basic Settings of the fluid domain is found in Figure 96 in Appendix C. Table 8 shows the fluid models used. The boundary conditions of the control volume are defined in Table 9. Table 10. Table 11. and Table 12.

Table 8. Fluid Domain Settings Establishing Two-Fluid System, after [27].

Tab	Setting	Input
Fluid Models Multiphase	Homogenous Model	Checked
	Free Surface Model	Standard
Fluid Models Heat Transfer	Homogeneous Model	Checked
	Fluid Temperature	25 [C]
Fluid Models Turbulence	Option	k-Epsilon
	Wall Function	Scalable
Fluid Pair Models Air Water	Surface Tension Coefficient	Checked
	Surf. Tension Coeff.	0.072 [N m ⁻¹]
Fluid Pair Models Surface Tension Model	Option	Continuum Surface Force
	Primary Fluid	Water
Fluid Pair Models Interphase Transfer	Option	Free Surface
	Mass Transfer Option	None
Initialization Static Pressure	Option	Automatic With Value
	Relative Pressure	UpPres
Initialization Turbulence	Option	Medium (Intensity = 5%)
Initialization Volume Fraction-Air	Option	Automatic with Value
	Volume Fraction	UpVFAir
Initialization Volume Fraction-Water	Option	Automatic with Value
	Volume Fraction	UpVFWater

Table 9. Inlet Boundary Conditions, after [27].

Tab	Setting	Input
Basic Settings	Boundary Type	Inlet
	Location	Inlet
Boundary Details	Normal Speed	1 [m s ⁻¹]
	Turbulence	Intensity and Length Scale
	Fractional Intensity	0.05
	Eddy Length Scale	UpH
Fluid Values	Air	Value-UpVFAir
	Water	Value-UpVFWater

Table 10. Outlet Boundary Conditions.

Tab	Setting	Input
Basic Settings	Boundary Type	Outlet
	Location	Outlet
Boundary Details	Flow Regime	Subsonic
	Mass and Momentum	Option-Average Static Pressure
	Relative Pressure	DownPres
	Pres. Profile Blend	0.05

Table 11. Opening Boundary Conditions, after [27].

Tab	Setting	Input
Basic Settings	Boundary Type	Opening
	Location	Opening
Boundary Details	Mass and Momentum	Option-Entrainment
	Mass and Momentum	Relative Pressure - 0 [Pa]
	Turbulence - Option	Zero Gradient
Fluid Values	Air	Value-1
	Water	Value-0

Table 12. Wall Boundaries.

Tab	Setting	Input
Basic Settings	Boundary Type	Wall
	Location	Walls
Boundary Details	Mass and Momentum	Option-Free Slip Wall
	Mass and Momentum	Wall Adhesion-None

2. Solver Control and Mesh Adaptation

In order for CFX to complete the simulation, upwind differencing had to be used. The other options resulted in the error messages part-way through the simulation. A mesh adaptation was added to better define the interface between air and water. This was required since adding a semi-submerged plate into the flow greatly increased the complexity of the flow field. Later images show the high resolution of this boundary. The solver controls are defined in Table 13. The added mesh refinement can be found Figure 97 in Appendix C.

Table 13. Solver Controls, after [27].

Tab	Setting	Input
Basic Settings	Advection Scheme	Option-Upwind
	Turbulence Numerics	Option-First Order
	Convergence Criteria	Type-RMS
		1e-06
Advanced Options	Dynamic Model Control	Checked
	Multiphase Control	
	Surface Tension Coefficient	
	Volume Fraction Coupling	Option-Coupled

B. CFX RESULTS AND DISCUSSION

All of the simulations were completed at 1 m/s. For this reason, the flow profile around the plate is tamer in the simulations when compared to the flow profiles visible in the images taken during the experiment. The waterline in the two-fluid domain was

highlighted using an isosurface. The isosurface was placed at the “Water.Volume Fraction” value of 0.99. A vertical plane was also created that ran the length of the control volume. This shows that the water was below the isosurface. Figure 79 shows the water level for the entire control volume for both orientations.

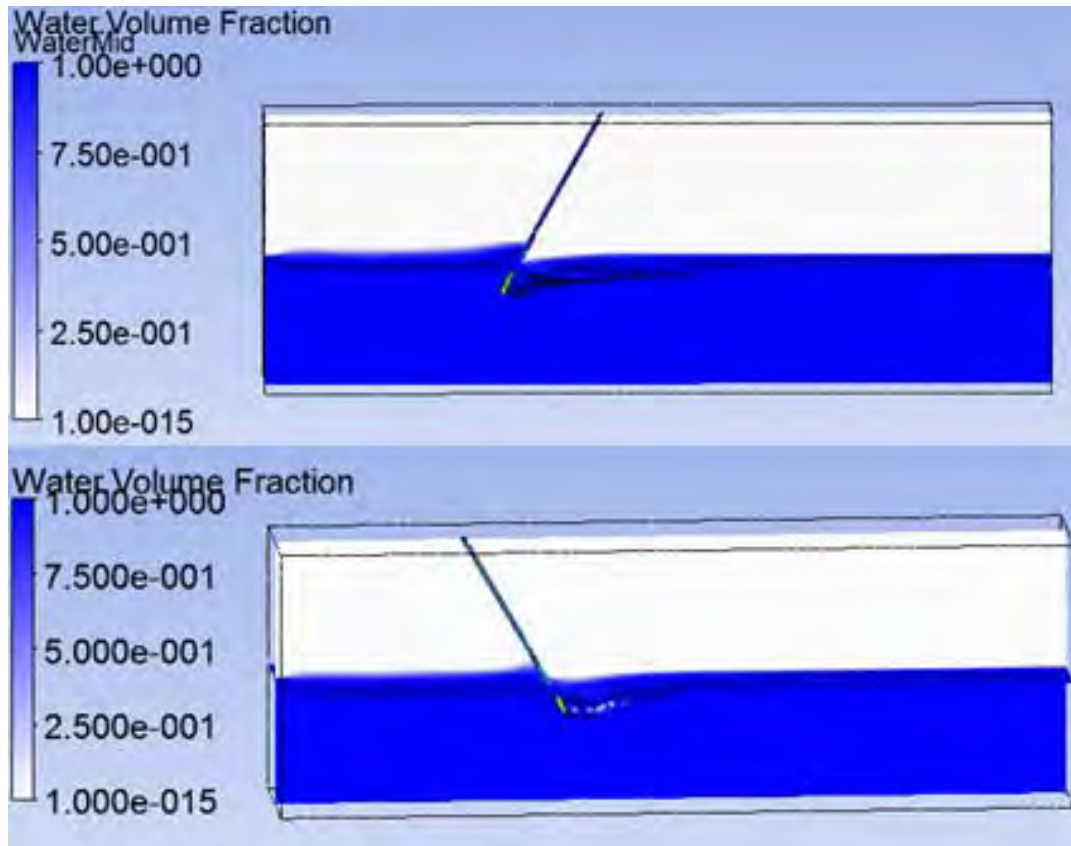


Figure 79. Water Level for Tumblehome (Top) and Conventional (Bottom) Flow Simulations.

Next, the region before the plate was expanded to view the bow wave created by each orientation. As expected, the bow wave was larger for the tumblehome trial. It appears that there is a small region of air trapped between the plate and the water for the conventional trial. The wake also extends farther back for the conventional trial. The tumblehome oriented plate is fully submerged. The region in front of the plate is found in Figure 80. The wake region is shown in Figure 81. These images prove that the setup

used for the simulation was correct. For comparison, the tumblehome trial can be found on the left, while the conventional trial can be found on the right.

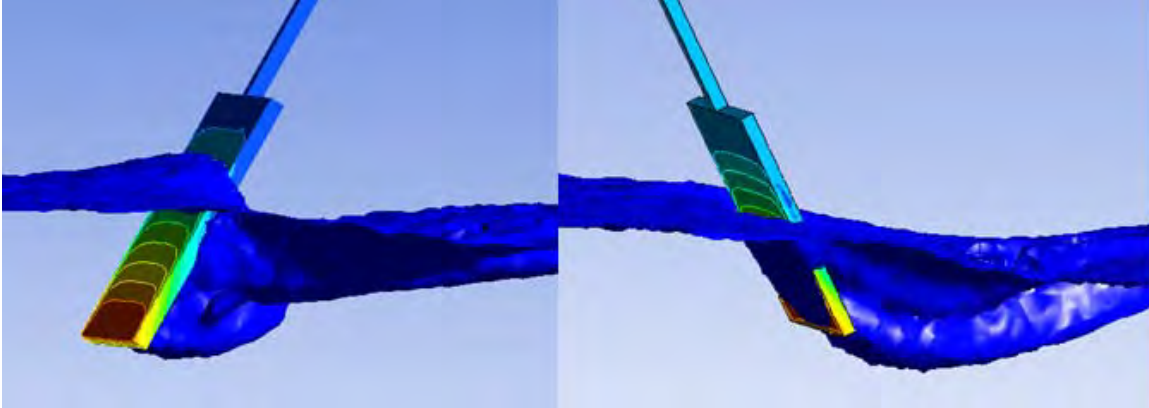


Figure 80. Exploded View of Water Level Preceding the Tumblehome (Left) and Conventional (Right) Oriented Plates.

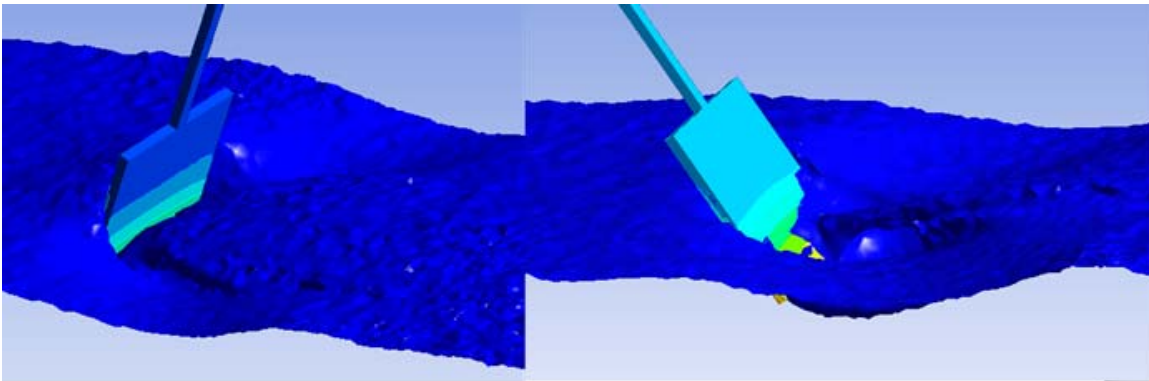


Figure 81. Exploded View of the Wake Region behind the Tumblehome (Left) and Conventional (Right) Oriented Plates.

The velocity profile of the water was also inspected. The velocity profile presented in Figure 82 shows high velocity regions to the left and right of the plate. The highest water velocity this region was 1.272 m/s, which is 27% faster than the inlet flow. There is a low velocity region immediately behind the plate. This image shows water velocity vectors above the fluid domain as well. Figure 79 shows that the lowest water volume fraction in the control volume is $1.0 \cdot 10^{-15}$. This would be the equivalent of the amount of water present in the air due to humidity. The presence of this extra fluid is

assumed to have negligible effects on the results. Water velocities were similar for both orientations.

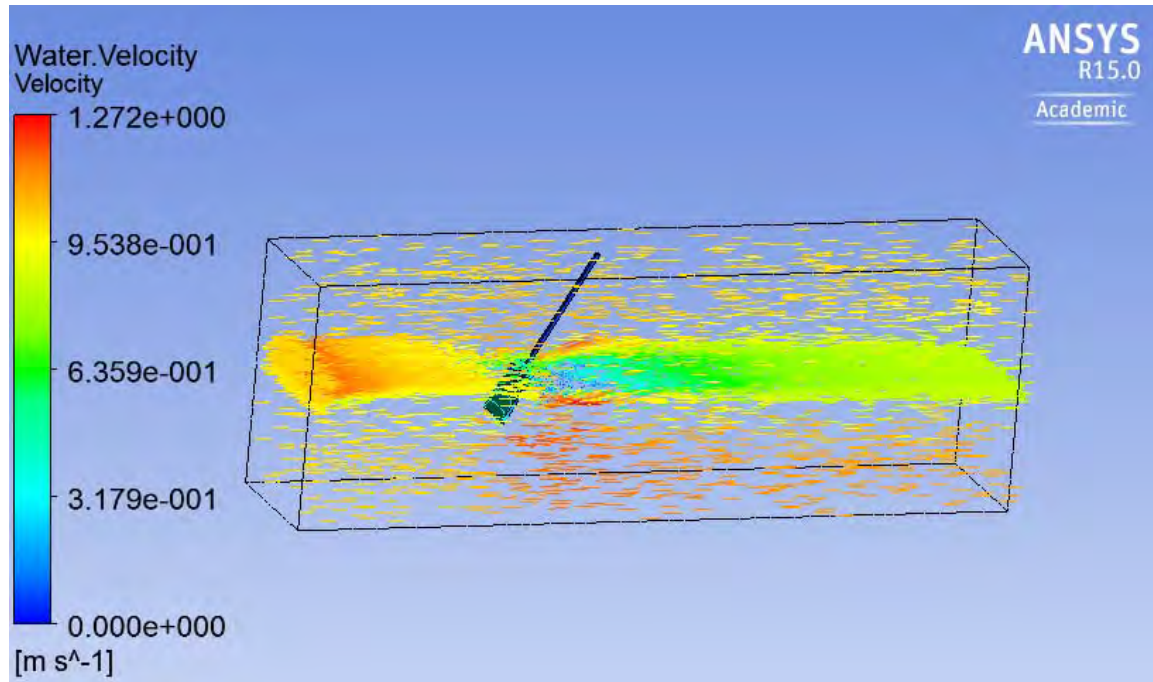


Figure 82. Water Velocity in the Control Volume. Inlet Velocities are 1.0 m/s.

There were two desired results from this analysis. Since ice could not be added to the system, the first goal of this initial Ansys analysis was to locate the high pressure fluid in front of the plate that aided in displacing the ice equivalent in the experiment. The second was to determine the incident force found on the plate.

In order to examine the pressure in the fluid, horizontal planes were created in the control volume at various heights along the plate. Horizontal planes had to be used because the hydrostatic pressure increases as the depth increases for water. Any comparison using vertical planes showed high pressures at the bottom of the tank. The next set of images compares the pressure surrounding the plate. As before, the tumblehome trials can be found on the left while the conventional trials are on the right. Figure 83 shows the pressure ranging from the plane at the bottom to the plane at the surface of the water. The distance between the heights of each plane is 7 cm (2.75 inches).

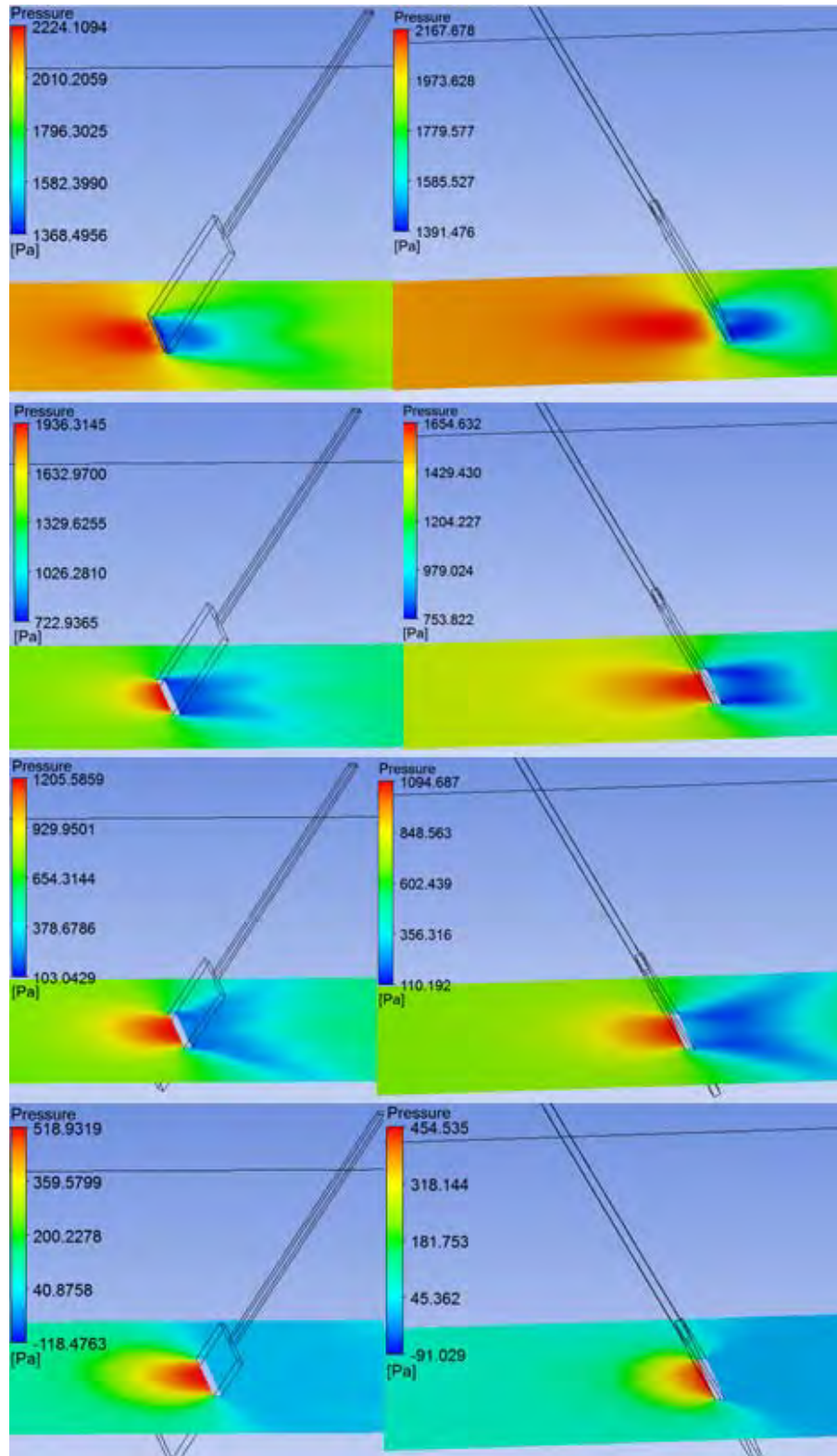


Figure 83. Pressure Planes Signifying the High Pressure Region Preceding the Tumblehome (Left) and Conventional (Right) Oriented Plates.

The pressure preceding the tumblehome oriented plate was consistently greater than the pressure in front of the conventional oriented plate. In order to properly assess the pressure rise created by the plate, the hydrostatic pressure was subtracted from the pressure values from each plane. Table 14 shows the process of correcting the peak pressure value for each plane. It was assumed that the density of the water was 1000 kg/m^3 and that the highest plane was located at the water level. The latter assumption was made because the bow wave made it difficult to find the exact water level of the water. Regardless, the tumblehome trial consistently had greater pressure values than the conventional trial. The information was plotted in Figure 84.

Table 14. Elimination of Hydrostatic Force from Peak Pressure Data.

Plane Depth (cm)	Resulting Hydrostatic Pressure (Pa)	Pressure from Tumblehome Trial (Pa)	Pressure from Conventional Trial (Pa)	Final Tumblehome Pressure (Pa)	Final Conventional Pressure (Pa)
21	2060.1	2224.1	2167.7	164.0	107.6
14	1376	1936.3	1654.6	560.3	278.6
7	686.7	1205.6	1094.7	518.9	408.0
0	0	518.9	454.5	518.9	454.5

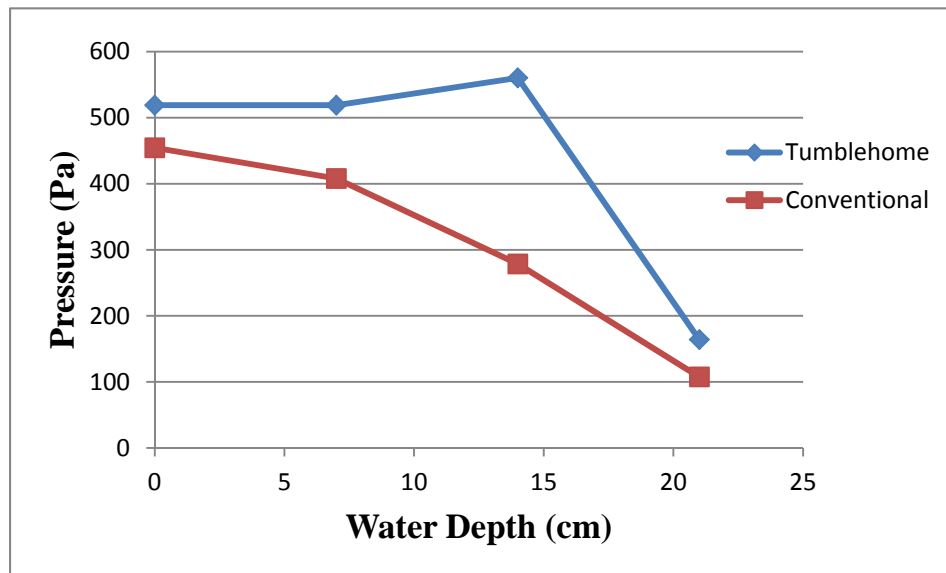


Figure 84. Pressure Rise Preceding Both Plate Orientations.

This increase in pressure may be the source of the ice displacing property exhibited by the tumblehome oriented plate in the experiment. The greatest pressure differential between the pressure in front of each orientation was near the lower section of the plate.

Finally, the incident pressure against the plate was determined. The data from the base water trials showed that it required nearly twice the force to tow the tumblehome oriented plate through the water than to tow the conventional oriented plate. The Ansys trials support this finding. The results of the Ansys trials shown in Figure 85 show that the incident pressure is consistently greater on the tumblehome oriented plate. The incident force against the plate is the integral of the pressure over the surface area of the plate.

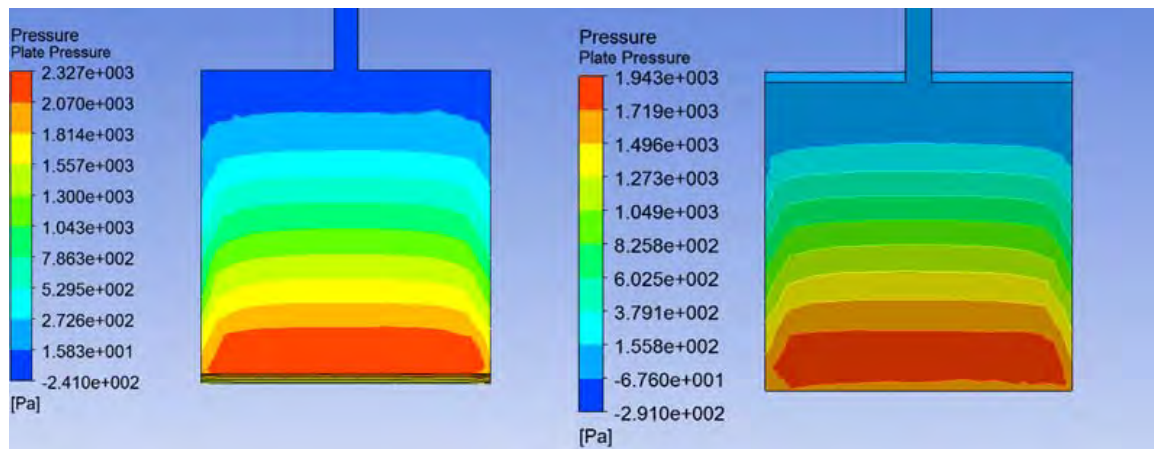


Figure 85. Incident Pressure against the Tumblehome (Left) and Conventional (Right) Oriented Plate Acquired from Ansys Simulation.

C. SUMMARY OF CFX ANALYSIS

The CFX simulation properly constructed the tow tank environment. The two-fluid domain was established with the free surface present at the same location of the water line on the plate in the experiment. The high pressure region preceding the plate for both the tumblehome and conventional orientation was successfully simulated. The pressure in front of the plate was greater at all water levels for the tumblehome-oriented plate. This increased pressure aided in the plate's ability to displace the ice equivalent

during experimental trials. By displacing the ice, the impact between the plate and the ice equivalent was lessened. The incident pressure against the plate was also plotted. Once again, the simulation supported the findings in the experiment. In the experiment, the tumblehome oriented plate required a greater towing force than the conventional oriented plate required. The Ansys analysis determined that the pressure on the tumblehome oriented plate was greater than the pressure incident to the conventional oriented plate.

1. Recommendations for Future Work

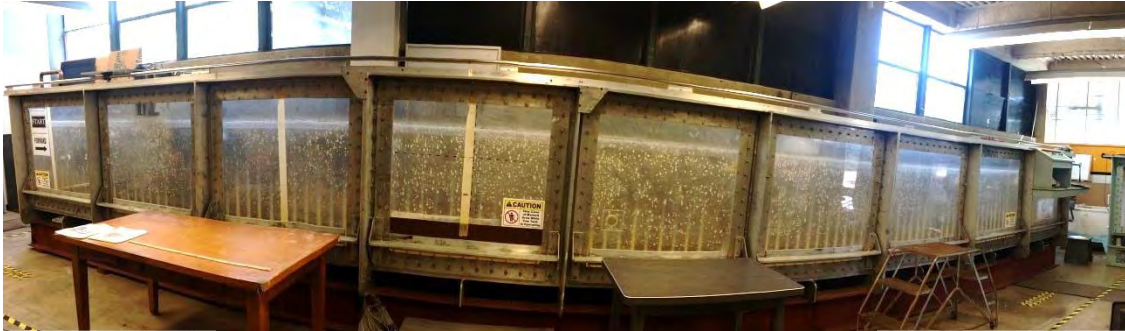
While the high pressure region was successfully simulated, adding the ice equivalent to the Ansys analysis was not accomplished. A complete analysis would be completed if two tasks were accomplished. First, future work can be done to insert the ice equivalent into the Ansys simulation. It may be possible that Ansys is not capable of accounting for solid free-floating particles. If this is the case, different modeling software suitable for FSI FEM must be used. Finally, in a complete analysis, a structural analysis of a composite plate would be coupled to the CFX analysis for the two tank experiment. This would allow for the incident pressure on the plate to be imported to a structural analysis to determine the stress and strain experienced by the composite plate.

THIS PAGE INTENTIONALLY LEFT BLANK

APPENDIX A. TOW TANK SOP

A. FILLING AND DRAINING

In order to operate the tow tank it is necessary to understand the filling and draining procure. The tow tank is shown below in Figure 86.



Fill Valve

Figure 86. Halligan Hall Tow Tank.

Drain Valve

It is 36 feet long, three feet wide, and four feet high. These dimensions allow the tank to effectively house a total of 2423 gallons of water. This calculation used a total water height of three feet rather than the tank height of four feet to allow for the waves incurred during experimentation. In order to fill the tank the first step is to close the drain valve. As shown in the figure, the drain valve is located on the right side of the tank. The open and closed position of the valve is shown in Figure 87.



Figure 87. Drain Valve Open (Left) and Closed (Right) Positions.

Once this valve is closed, the tank may be filled with water. The water line can be found on the opposite side of the tank from the drain valve. The open and close positions are identical to the drain valve. Copper piping has been added to the original system due to issues involving back flow, which resulted in the flooding of the laboratory floor. Rather than the water being added from the bottom of the tank where the water pressure is notably high once full, the water is redirected and is added from above the tank as shown in Figure 88.



Figure 88. Tow Tank Fill Piping.

B. CARRIAGE OPERATION

With the tank ready for testing, the next step any experiment is to understand how the carriage operates. The carriage translates along the length of the tow tank along rails shown in Figure 89. The areas along the rails should be cleared of any objects. For safety reasons, when the tow tank is in operation, all personnel must stay behind the yellow floor tape surrounding the tank. A pulley system is used in connection with the motors to translate the carriage along the tank.



Figure 89. Carriage System.

Operators should exercise caution when the carriage is at the outer limits of the tow tank. There is no safety mechanism to stop the carriage from hitting the wall. This will cause major damage to the pulley system and its connections. First, the motor must be powered on using the outlet boxes located between the tow tank entrance of Halligan Hall and the drain valve. The motor switches are shown in Figure 90. The on position is clearly marked on the box. For powering on, the middle switch should be powered on before powering on the right box. For powering off the carriage system, simply reverse the order.



Figure 90. Carriage System Power Switches.

The carriage is controlled with the controller shown in Figure 91. The controller has 100 feet of cable allowing its use along the entire tank.



Figure 91. Carriage Controller.

The important keys for operation are explained below:

ENTER: Used to change speed settings. Different speeds are represented in Hz. Change the speed setting by using the up and down arrows, then pressing Enter again.

LOCAL/REMOTE: Must be toggled until “Local” is displayed in the upper right corner of the controller.

FWD/REV: Moves the carriage forward or backwards at the speed inputted. As of this thesis, REV moves the carriage from left to right. **Carriage continues to move until Stop is pressed.**

JOG: Pressing Jog will illuminate a green light on the corner of the button. This feature allows the operator to move the carriage forward and backwards only when the FWD/REV button is depressed. The carriage will move at the 3 Hz speed setting only while the FWD/REV button is depressed under Jog operations.

A summary for operation is found on the next page. A table with the resulting RPM of each speed setting is shown after the summary.

Operational Use–Summary

Read Entire Page Before Operation

- Ensure that the rails that the carriage moves on is clear of any objects
- Power on the tank using the switches located near the entrance
 - Powering On – First flip middle switch, then outside switch (Labeled “Tow Tank”)
 - Powering Down – First flip outside switch, then middle switch
- Retrieve the controller
 - Press “Local/Remote” until “Local” is displayed in upper right hand corner.
 - Press Enter to select a speed. Toggle up or down then press Enter again.
 - Ensure all personnel are outside the area cordoned off by the yellow caution tape on the floor.
 - Press Forward or Reverse to move carriage at selected speed. **Carriage continues to move until Stop is pressed.**
 - Another movement option is Jog. Jog moves the carriage only when the Forward or Reverse button is depressed. Press Jog (Green corner light will light up), then hold the desired direction for the carriage to move.
- Power off the switches when finished with the tow tank

Exercise caution near the outer limits of the tank. There are no safety mechanisms to stop the carriage from moving. A collision with the wall may break the pulley system or its connections.

Carriage Speeds in Water

Entered Speed (Hz)	Resulting RPM	Carriage Speed (m/s)
2.0	N/A	N/A
2.5	N/A	N/A
3.0	74	0.4995
3.5	88.5	0.58415
4.0	103	0.6688
4.5	117.5	0.7534
5.0	132	0.8381
5.5	146.5	0.9228
6.0	161	1.0074
6.5	175.5	1.0921
7.0	188	1.1767
7.5	200	1.2614
8.0	214.5	1.3460
8.5	227	1.4307
9.0	240	1.5153

APPENDIX B. STRAIN GAUGE CONNECTION: QUARTER-INCH BRIDGE ADAPTER

Each time a new plate is tested in the tow tank, the strain gauges must be connected to the data acquisition system. This section summarizes how to install a new set of strain gauges. The first step is to use a small flathead screwdriver to open the ports of each quarter-inch bridge adapter. The two wires from the strain gauges should be inserted to ports 0 and 2. The screws should be tightened to secure the wire inside the port. Finally, a bridge needs to be fabricated from a small length of wire. This experiment used a one-inch section of wire with its ends stripped. This small wire should connect ports 1 and 2. This wire creates a ground for the voltage to travel to. To ensure the strain gauges are set up properly a voltmeter can be used to check the resistances across ports 0 and 1. As long as there is a resistance between the two ports it will function properly. The resistance may not be the published resistance of the strain gauge. Figure 92 shows the connections for a plate with three strain gauges.

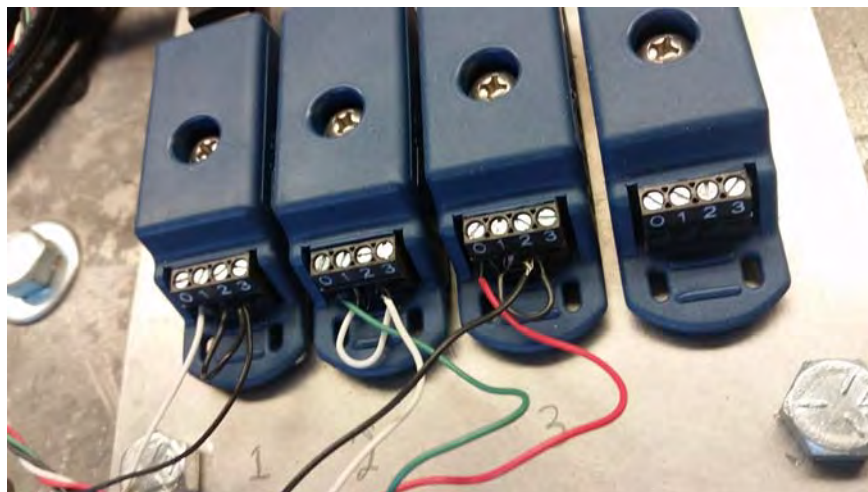


Figure 92. Strain Gauge Connection to the Quarter-Inch Bridges.

THIS PAGE INTENTIONALLY LEFT BLANK

APPENDIX C. SUPPLEMENTAL CFX IMAGES

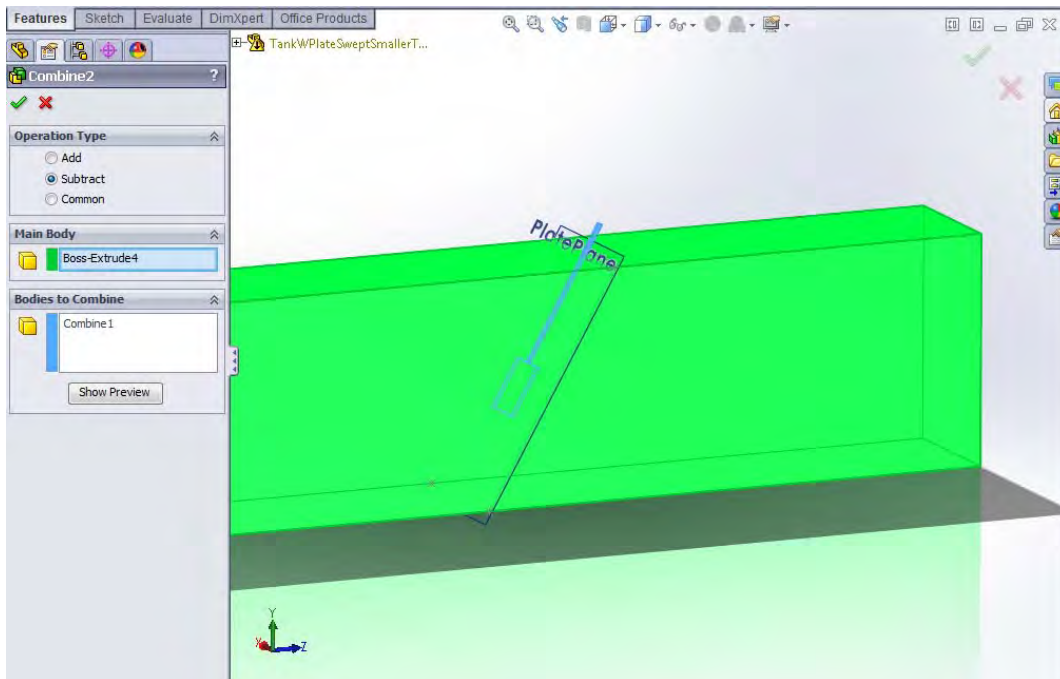


Figure 93. The Towed Plate and the Attachment Bar are Removed from the Control Volume of the Tow Tank Using the Combine Feature in Solidworks. The Plane Created to Generate the Plate Orientation is also Visible.

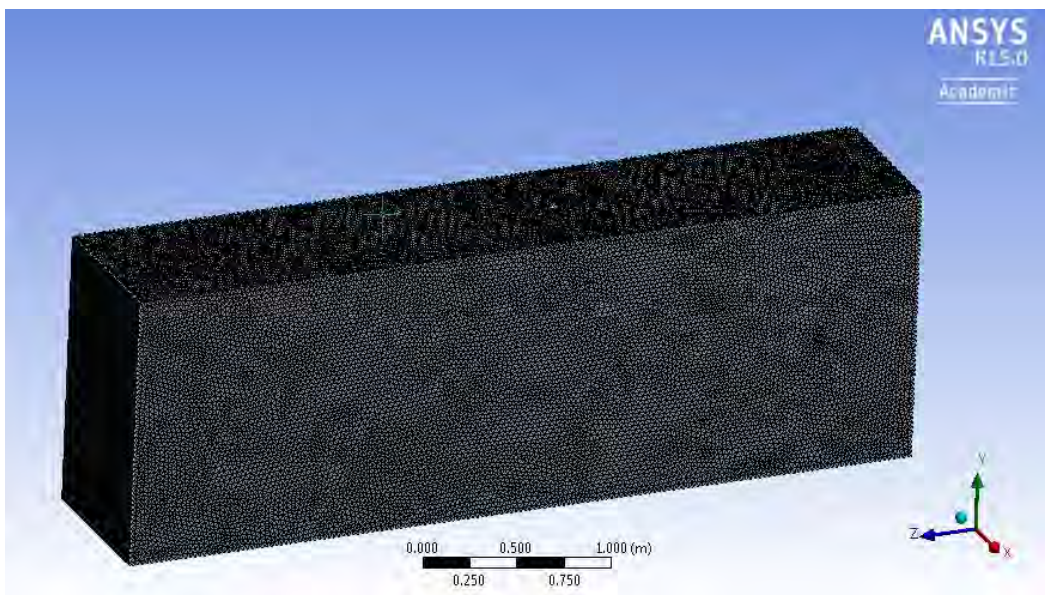


Figure 94. Mesh Used in CFX Trials.

Expressions		
✓α	DenH	$(DenWater - DenRef)$
✓α	DenRef	$1.185 [kg\ m^{-3}]$
✓α	DenWater	$997 [kg\ m^{-3}]$
✓α	DownH	$0.73152 [m]$
✓α	DownPres	$DenH * g * DownVFWater * (DownH - y)$
✓α	DownVFAir	$step((y - DownH)/1 [m])$
✓α	DownVFWater	$1 - DownVFAir$
✓α	UpH	$0.73152 [m]$
✓α	UpPres	$DenH * g * UpVFWater * (UpH - y)$
✓α	UpVFAir	$step((y - UpH)/1 [m])$
✓α	UpVFWater	$1 - UpVFAir$

Figure 95. Variables Created for CFX Analysis, after [27].

Details of **Default Domain** in **Flow Analysis 1**



Basic Settings	Fluid Models	Fluid Specific Models	Fluid Pair Models	Initialization
Location and Type				
Location		B158		...
Domain Type		Fluid Domain		
Coordinate Frame		Coord 0		
Fluid and Particle Definitions...				
Air Water		 		
Water				
Option		Material Library		
Material		Water		...
Morphology				
Option		Continuous Fluid		
<input type="checkbox"/> Minimum Volume Fraction				
Domain Models				
Pressure				
Reference Pressure		1 [atm]		
Buoyancy Model				
Option		Buoyant		
Gravity X Dirn.		0 [m s ⁻²]		
Gravity Y Dirn.		-g		
Gravity Z Dirn.		0 [m s ⁻²]		
Buoy. Ref. Density		DenRef		
Ref. Location				
Option		Automatic		
Domain Motion				
Option		Stationary		
Mesh Deformation				
Option		None		

Figure 96. Fluid Domain Basic Settings, after [27].

Outline

Mesh Adaption

Details of **Mesh Refinement in Flow Analysis 1**

Basic Settings

Advanced Options

☒ Activate Adaption

Region List

B158

☐ Save Intermediate Files

Adaption Criteria

Variables List

Air Volume Fraction

Max. Num. Steps

2

Option

Multiple of Initial Mesh

Node Factor

4

Adaption Method

Option

Solution Variation

Minimum Edge Length

0.0

Adaption Convergence Criteria

Max. Iter. per Step

100

Residual Type

RMS

Target Residual

0.001

Basic Settings

Advanced Options

Node Alloc. Parameter

1.6

Number of Levels

2

Figure 97. Mesh Adaptation Settings, after [27].

LIST OF REFERENCES

- [1] M. Begich. (2013, Jan. 01) Increased activity in the Arctic calls for more U.S. preparation, leadership. *Sea Technol.* [Online]. 54(1) pp. 34–35. Available: <http://search.proquest.com/docview/1287417719?accountid=12702>
- [2] Q&A: South China Sea dispute. (2015, Apr. 17). BBC News. [Online]. Available: <http://www.bbc.com/news/world-asia-pacific-13748349>
- [3] D. Lehrke. (2014, May 07). The cold thaw. *Jane's Def. Weekly.* [Online]. 51(24). Available: <http://search.proquest.com/docview/1521871560?accountid=12702>
- [4] Lomonosov ridge geographic feature, Arctic Ocean. (n.d.). Encyclopedia Britannica [Online]. Available: <http://www.britannica.com/EBchecked/topic/346795/Lomonosov-Ridge>. Accessed Jan. 12, 2015.
- [5] B. Leira et al. (2009, Nov.) Ice-load estimation for a ship hull based on continuous response monitoring. *Proc. of the Inst. of Mech. Eng.* [Online]. 223, pp. 529–540. Available: <http://search.proquest.com/docview/194684695?accountid=12702>
- [6] P. Toensmeier. (2006, Feb.) Advanced composites put to sea in navy's new ship. *Plast. Eng.* [Online]. 62(2), pp. 26–28. Available: <http://search.proquest.com/docview/213909263?accountid=12702>
- [7] M80 Stiletto next-generation littoral vessel, United States of America. (n.d.). Naval-Technology [Online]. Available: <http://www.naval-technology.com/projects/m80-stiletto/m80-stiletto6.html>. Accessed Jan. 12, 2015.
- [8] K. Baron. (2013, Nov.21) Inside the secret interior of the navy's first stealth destroyer. [Online]. Available: <http://www.defenseone.com/ideas/2013/11/inside-secret-interior-navys-first-stealth-destroyer/74321/>
- [9] Arleigh Burke Class (Aegis) Destroyer, United States of America. (n.d.). Naval-Technology. [Online]. Available: <http://www.naval-technology.com/projects/burke>. Accessed Apr. 09, 2015.
- [10] Ulstein delivers third medium sized PSV to Blue Ship Invest. (2006, Mar. 6). Ulstein [Online]. Available: <http://worldmaritimenews.com/archives/78178/norway-ulstein-delivers-third-medium-sized-psv-to-blue-ship-invest>

- [11] B. T. Ellis, "An investigation into the damaged stability of a tumblehome hull warship design," M.S. thesis, Dept. Mech. Aerosp. Eng., Naval Postgraduate School, Monterey, CA, 1997.
- [12] M. F. Pinnell and P. O. Sjoblom, "Low-velocity impact testing of thermoplastic and thermoset matrix composite materials," Wright Res. and Dev. Cent. AF Sys. Comm., Wright-Patterson AFB, OH, Rep. 91-00898, Nov. 1990.
- [13] W. Elber, "Failure mechanics in low-velocity impacts on thin composite plates," Langley Res. Cent., Hampton, VA, Rep. 19951226 108, May 1983.
- [14] J. E. Russell, "Dynamic response of composite structures underwater," M.S. thesis, Dept. Mech. Aerosp. Eng., Naval Postgraduate School, Monterey, CA, 2013.
- [15] A. C. Owens, "An experimental study of fluid structure interaction of carbon composites under low velocity impact," M.S. thesis, Dept. Mech. Aerosp. Eng., Naval Postgraduate School, Monterey, CA, 2012.
- [16] Sea ice types. (2010, Nov. 03) Australian Antarctic Division [Online]. Available: <http://www.antarctica.gov.au/about-antarctica/environment/icebergs-and-ice/sea-ice>
- [17] Navigating through brash ice and growlers. (n.d.). Word Press. [Online]. Available: <https://sarahfenwick.wordpress.com/2010/01/19/antarctica/navigating-through-brash-ice-and-growlers/>. Accessed Apr. 09, 2015.
- [18] P. Wadhams. (2003, Jan. 01) How does Arctic Sea ice form and decay. [Online]. Available: http://www.arctic.noaa.gov/essay_wadhams.html
- [19] G. W. Timco and R. M. W. Frederking, "A review of sea ice density," Nat. Res. Council of Can., Ottawa Canada, Rep. 0165-232 Mar. 1995.
- [20] Equation of state. (n.d.). National Institute of Ocean Technology [Online]. Available: https://www.niot.res.in/COAT/coat_pdf/CHAP%20III%20-%20Equation%20of%20State.pdf. Accessed Jan. 24, 2015.
- [21] National Oceanic and Atmospheric Administration Database. [Online]. Available: <https://www.nodc.noaa.gov/cgi-bin/OC5/NPclimatology/arcticfig.pl?parameter=t>. Accessed Jan. 24, 2015.
- [22] More about plastics. (n.d.). McMaster Carr. [Online]. Available: <http://www.mcmaster.com/#8574kac/=wqjgsf>. Accessed Jan. 12, 2015.
- [23] P. Colla (2010, Apr. 26) Photos of Drygalski Fjord. [Online]. Available: <http://www.oceanlight.com/log/2010/04>

- [24] Port Lockroy. (n.d.). Chinese-Poems. [Online]. Available: <http://chinese-poems.com/blog/?p=837>. Accessed Apr. 09, 2015.
- [25] S. C. Millhouse, "Hydrodynamic forces on composite structures," M.S. thesis, Dept. Mech. Aerosp. Eng., Naval Postgraduate School, Monterey, CA, 2014.
- [26] S. C. Knutton, "Computational analysis of effect of transient fluid forces on composite structures," M.S. thesis, Dept. Mech. Aerosp. Eng., Naval Postgraduate School, Monterey, CA, 2013.
- [27] Ansys 12.1 Help. (2009) Chapter 9. Free surface flow over a bump. Ansys Inc. Program Tutorials Archive.

THIS PAGE INTENTIONALLY LEFT BLANK

INITIAL DISTRIBUTION LIST

1. Defense Technical Information Center
Ft. Belvoir, Virginia
2. Dudley Knox Library
Naval Postgraduate School
Monterey, California